Continuous-Wave Magnetic Field Sensing with Nitrogen-Vacancy Centers in Diamond

Ahmadi, Sepehr

Publication date:
2018

Document Version
Publisher's PDF, also known as Version of record

PhD Thesis

Continuous-Wave Magnetic Field Sensing with Nitrogen-Vacancy Centers in Diamond

Department of Physics

Technical University of Denmark

Sepehr Ahmadi

Supervisor: Professor Ulrik Lund Andersen
Co-supervisor: Associate Professor Alexander Huck
Co-supervisor: Associate Professor Jørn Otto Bindslev Hansen

September 2018

Acknowledgments

I am deeply grateful to my supervisors, Professor Ulrik Lund Andersen, Associate Professor Alexander Huck, and Associate Professor Jørn Otto Bindslev Hansen, for giving me the opportunity to perform research on the frontiers of the field and for all their support during my studies.
Special thanks to Haitham for all his help and encouragement and Adam, Alexander S., Louise, James, and Mürsel for all the valuable discussions we had regarding magnetometry.
I am thankful to Jonas for sharing his insights on cavities, Kristian for help with diamond preparation, Tobias, Ruben, and Aleksander for their support regarding electronics, Erik, Søren, Bjarne, and Poul for preparing workshop tasks, and Tine, Nana, Helle, and Marianne for assisting me in all the administrative work.
I am grateful to Alexander H., Casper, Christian, Haitham, Ilya, James, Jan, Joost, Jørn, Joshua, Louise, Mikkel, Rasmus, and Ulrik who gave me valuable and constructive feedback on this thesis.
I would like to acknowledge all the people in the Quantum Physics and Information Technology (QPIT) section who created a great work environment: Adam, Adriano, Aleksander, Alexander H., Alexander S., Andreas, Arne, Casper, Christian, Christian B., Clemens, David, Dennis, Dino, Haitham, Hossein, Hou-Man, Hugo, Ilya, Iman, Iyad, Jacob, James, Jan, Jens, Jonas, Joost, Jørn, Joshua, Juanita, Kirstine, Kristian, Louise, Mads, Mikkel, Niels, Nitin, Olivier, Rasmus, Rayssa, Ruben, Shuro, Timur, Tine, Tobias, Ulrich, Ulrik, Xueshi, and Yuriy.
Finally, I would like to thank Timur, Alexander S., Olivier, Mikkel, Dennis, and Jacob for sharing room 217 with me.

It was a pleasure to be a QPITer.

Lyngby, September 2018

Sepehr

Abstract

The nitrogen-vacancy center, a point defect in diamond, is a promising quantum sensor for magnetic field sensing with high sensitivity and high spatial resolution under ambient conditions. Such a magnetometer has potential applications in various fields, including neuroscience, microelectronics, and nanoscale magnetic resonance microscopy.

This thesis presents cavity-enhanced magnetic field sensing using ensembles of nitrogen-vacancy centers in diamond. We apply a phase-sensitive detection method in our experiments and discuss our efforts regarding exploring the ideal modulation conditions. We demonstrate a $\sim$ 400 pT/$\sqrt{\text{Hz}}$ magnetic noise density spanning a bandwidth up to 125 Hz, by measuring the changes in the fluorescence level. Using a five-level model for nitrogen-vacancy centers, a physical model is developed that shows excellent agreement with the measured optically detected magnetic resonance spectra.

Furthermore, we introduce an alternative technique for measuring the electron spin-states of nitrogen-vacancy centers based on recording the absorption of the pump light. This method is employed for magnetic field sensing, and a magnetic noise floor of $\sim$ 100 nT/$\sqrt{\text{Hz}}$ is measured spanning a bandwidth up to 125 Hz. We modified the five-level model to describe the absorption detected magnetic resonance of a diamond placed inside an optical cavity. The model agrees very well with experiments.

Resumé

Nitrogenvakancecentret, som er en punktdefekt i diamant, er en lovende kvantemekanisk magnetfeltsensor som kan detektere magnetfelter med høj rumlig opløsning. Et sådant magnetometer har anvendelsespotentiale indenfor flere forskellige områder, heriblandt neurovidenskab, mikroelektronik og magnetisk resonansmikroskopi på nanoskala.

Denne afhandling præsenterer kavitetforstærket magnetfeltsdetektion med ensembler af nitrogenvakancecentre i diamant. Eksperimentelt anvendes en faseføls om målemetode, og vi diskuterer vores arbejde med at karakterisere de ideelle modulationsparametre. En magnetisk støjtæthed på ~ 400 pT/$\sqrt{\text{Hz}}$ i en båndbredde af 125 Hz er demonstreret ved at måle ændringerne i fluorescensintensiteten. En fysisk model med fem energiniveauer er udviklet for nitrogenvakancecentret, og den stemmer fremragende overens med de optisk detekterede magnetiske resonanser.

Endvidere introducerer vi en alternativ teknik til bestemmelse af elektronspintilstande i nitrogenvakancecentre, som er baseret på målinger af absorptionen af pumpelyset. Denne metode anvendes til magnetfeltsdetektion, og der er målt en magnetisk grundstøj på ~ 100 nT/$\sqrt{\text{Hz}}$ i en båndbredde af 125 Hz. Vi har modificeret fem-niveau-modellen for at simulere absorptionsdetekteret magnetisk resonans i en diamant placeret i en optisk kavitet. Modellen stemmer glimrende overens med eksperimentelle resultater.

Contents

1 Introduction **1**
- 1.1 The importance of magnetic field sensing . . . 1
- 1.2 Magnetic sources and sensor competitors . . . 2
- 1.3 Thesis structure . . . 4

2 Sensing With Nitrogen-Vacancy Centers **5**
- 2.1 Defects in diamond . . . 5
  - 2.1.1 Diamond synthesis . . . 6
  - 2.1.2 Diamond type classification . . . 6
- 2.2 Nitrogen-vacancy center . . . 7
  - 2.2.1 Crystallographic structure . . . 7
  - 2.2.2 Charge-state and isotope variations . . . 7
  - 2.2.3 Electronic configuration and optical transition . . . 8
- 2.3 Spin-state initialization and readout . . . 10
- 2.4 Rabi oscillation and spin coherence times . . . 12
- 2.5 Hamiltonian formalism . . . 14
- 2.6 Rate equation model . . . 15
- 2.7 Continuous-wave magnetometry . . . 17

3 Experimental Framework **19**
- 3.1 Diamond sample . . . 19
- 3.2 Spin-state control and readout . . . 20
  - 3.2.1 Microwave delivery . . . 20
  - 3.2.2 Optical drive . . . 21
  - 3.2.3 Optical cavity . . . 22
  - 3.2.4 Stabilization techniques . . . 24
- 3.3 Phase-sensitive detection . . . 26
- 3.4 Electron spin resonance measurement . . . 30
  - 3.4.1 Three-frequency excitation . . . 32
  - 3.4.2 Static and AC magnetic field inclusions . . . 34
  - 3.4.3 Analyzing data . . . 34

3.4.4 Pulsed measurements 37

4 Optimized Frequency Modulation 39
4.1 Introduction 39
4.2 Publication 39

5 Pump-Enhanced Continuous-Wave Magnetometry 53
5.1 Introduction 53
5.2 Publication 54

6 Magnetometry Based on Pump Absorption 69
6.1 Introduction 69
6.2 Publication 70
6.3 Reflection-based magnetometry 79

7 Cavity-Enhanced Magnetometry 81
7.1 Introduction 81
7.2 Publication 81

8 Outlook 85

Chapter 1

Introduction

This chapter includes a short motivation highlighting the importance of magnetic field sensing. Next, certain state-of-the-art high-sensitive magnetometers are introduced. Finally, the structure of this thesis is presented.

1.1 The importance of magnetic field sensing

Magnetic fields are present everywhere around us. These fields are created from magnetic dipoles or moving charges and are generated by various sources. The Earth's magnetic field may have been the first of this type of field that humans paid attention to. We made simple compasses to sense this magnetic field and used them for positioning.

Later, we modeled this phenomenon by classical physics, and today, we explain it using quantum theory. We realized that certain animals can detect magnetic fields and use them for navigation, and some even use quantum mechanics to perform this navigation [1].

We also learned to use magnetism by developing new technological devices to generate, manipulate, and sense magnetic fields. Nowadays, we detect our orientation with the magnetometers in our smartphones, we apply magnetic resonance imaging for medical diagnoses, and we magnetically store information on hard disk drives and magnetic stripes on credit cards.

Additionally, electric impulses in animals, including humans, create weak magnetic fields. Highly sensitive devices are needed to measure the magnetic signals produced by the heart during cardiocycles with a technique called magnetocardiography or those produced by brain activity with a technique called magnetoencephalography. The sensing and imaging of such signals pave the way for advanced, earlier medical diagnoses and touch the lives of many.

The aforementioned examples highlight the importance of sensing very weak magnetic fields, especially for biomedical applications.

1.2 Magnetic sources and sensor competitors

There are various magnetic field sources around us. The amplitudes of certain environmental and biomagnetic fields are shown in Fig. 1.1. The unit of a magnetic field is the Tesla. One Tesla of magnetic field is a very strong field. Therefore, magnetic fields are usually reported in sub-Tesla units. For instance, we are surrounded by Earth's magnetic field, which is in the range of a few tens of micro-Tesla. The electric impulses in our body are another source of much weaker magnetic fields. Biomedical fields are in the range of nano-Tesla to femto-Tesla, and a magnetometer should be able to sense such weak fields to be practical for biomedical applications.

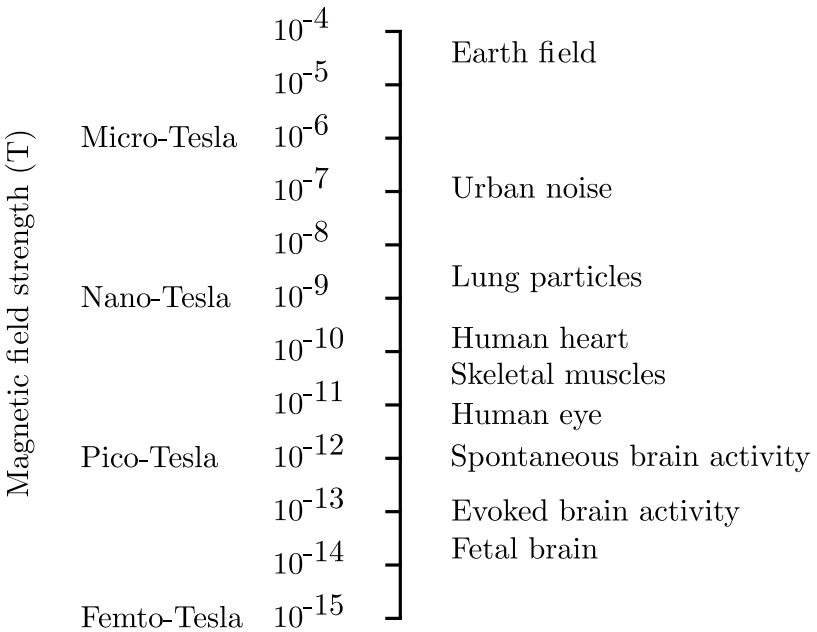

Figure 1.1: Amplitudes of various environmental and biomagnetic signals. Data taken from Ref. [2].

Next, we introduce three different sensitive magnetometers, certain of which are already being used for sensing biomagnetic fields.

Superconducting quantum interference devices

One extremely sensitive magnetometer is the superconducting quantum interference device (SQUID) based on Josephson tunneling [3, 4].

The direct current (DC) SQUID consists of two Josephson junctions in a superconducting loop. Biasing the current in a DC SQUID divides the current between two branches, each with a Josephson junction. An external magnetic flux generates a circulating current in the loop, which leads to different currents in each branch. Due to flux quantization in the loop, an oscillating voltage appears across the loop. Therefore, the SQUID acts as a flux-to-voltage transducer. Another type of SQUID is the radio frequency (RF) SQUID, which consists of only one Josephson junction in a superconducting loop.

Due to the superconducting loops in SQUIDs, they are typically operated at 4.2 K, the temperature of liquid helium. The use of high-temperature superconductors can increase the operating temperature to the temperature of liquid nitrogen. Sub-femto-Tesla sensitivities have been demonstrated by SQUIDs [5]. SQUIDs also have bandwidths from low frequencies to over 1 GHz [3]. Their high sensitivities and large bandwidth ranges make SQUIDs one of the best devices for sensing magnetic fields.

Spin exchange relaxation-free magnetometers

Spin exchange relaxation-free (SERF) magnetometers are another group of very sensitive magnetometers. As the name implies, spin exchange relaxation is avoided in this type of magnetometer. SERFs consist of an atomic medium containing a high density of alkali atoms that have intrinsic magnetic moments. A high density of atoms in a near-zero magnetic field at a high temperature causes spin-exchange collisions to occur faster than the precession frequency, and thus, decoherence due to spin-exchange interaction is eliminated [4].

The sensing of magnetic fields with SERFs is based on the interaction between the atoms and the magnetic field, which is governed by the Zeeman effect. SERFs sense magnetic fields through the following steps: The spin state of an atomic medium is polarized by an optical pump. The spin angular momentum precesses due to the torque produced by an external magnetic field. This precession of the magnetic moments affects the light passing through the medium, and thus, a probe beam can measure the precession frequency and extract information regarding the external magnetic field [4].

Sub-femto-Tesla sensitivities have been demonstrated by SERFs [6, 7]. Recently, a cesium vapor magnetometer was able to detect the magnetic

field generated by the action potential of a frog sciatic nerve [8]. In addition, a human brain has been imaged by a movable and wearable magnetometer using rubidium atoms [9].

Atomic magnetometers are superior to SQUIDs due to their high sensitivities with no requirements for cryogenic temperatures. However, atomic magnetometers can operate at near-zero magnetic field, and usually the sensor requires heating.

Nitrogen-vacancy centers in diamond

Magnetometry performed with these quantum defects in diamond is the topic of this thesis and is discussed in detail in the next chapter. In short, this is an attractive technology as diamond magnetometers are capable of operating in an unshielded environment at room temperature. Moreover, the biocompatibility of diamond makes it a suitable material for biosensing applications.

1.3 Thesis structure

This thesis consists of eight chapters. Chapter 2 introduces the background of the nitrogen-vacancy center and its properties for magnetic field sensing. Chapter 3 presents an experimental framework for magnetometry. Chapter 4, Chapter 5, Chapter 6, and Chapter 7 include the published results from this PhD study. Finally, an outlook is presented in Chapter 8.

Chapter 2

Sensing With Nitrogen-Vacancy Centers

The nitrogen-vacancy (NV) center is a promising system for various quantum sensing applications. There have been several studies regarding the use of NV centers to sense magnetic fields [10, 11], electric fields [12, 13], pressure [14], and temperature [15, 16] at high sensitivities and spatial resolutions under ambient conditions. Furthermore, applications of NV centers have been demonstrated in the fields of neuroscience [17, 18], cellular biology [19–21], nanoscale magnetic resonance microscopy [22–25], paleomagnetism [26], microelectronics [27–29], masers [30], random number generation [31], and fundamental science [32–34].

In the first part of this chapter, we start by introducing certain defects in diamond and presenting the main processes to synthesize single-crystal diamond. Next, we discuss the crystallographic and electronic configuration of the NV center in more detail.

In the second part of this chapter, we focus on sensing magnetic fields with NV centers, introduce spin-state initialization, manipulation, readout, and optically detected magnetic resonance technique. We continue by presenting Hamiltonian and a rate equation model. In the last section, continuous-wave magnetometry is presented as an approach for optical magnetometry with NV centers.

2.1 Defects in diamond

Diamond is a solid phase of carbon with many exceptional properties. Diamond has an extreme rigidity and a high thermal conductivity [35]. Its mechanical properties make it a practical material for industrial applica-

tions, for instance, for processing other materials. Furthermore, diamond is an attractive candidate for bioapplications due to its biocompatibility and optical properties [36].

Additionally, diamond is intriguing for quantum physics because of properties that surprisingly arise from impurities in its crystal structure. Point defects are common defects in a diamond crystal. Such defects are called color centers, as they give the diamond a particular color.

Progress has been made in studying different types of color centers in diamond such as the nitrogen-vacancy [37], silicon-vacancy [38–42], germanium-vacancy [43–47], and tin-vacancy [48]. Color centers have been employed in quantum sensing [49], quantum information processing [50–52], and single photon sources [31, 40]. We continue this chapter on synthesizing diamond with a focus on only one type of color center, the NV center.

2.1.1 Diamond synthesis

Natural diamonds are mostly formed in the Earth's mantle under high pressure and temperature conditions. Although natural diamonds are valuable, synthesized diamonds can be preferable for quantum applications due to the presence of undesired defects and inhomogeneities in natural crystals. Furthermore, certain properties of synthesized diamond are controllable during diamond growth.

There are two main approaches to synthesizing diamond: High pressure high temperature (HPHT) and chemical vapor deposition (CVD).

Initially, man-made diamond was synthesized using the HPHT method [53]. This technique resembles the growth conditions of natural diamond. Diamonds grown by HPHT usually have a yellow color because of their high concentrations of nitrogen impurities, a few ten to a few hundred parts per million (ppm), which come from the atmosphere or the growth materials [54].

The most common process for growing diamond is the CVD technique [55]. This technique is based on chemical reactions in the presence of different gaseous sources and the nucleation and growth of diamond on a crystal substrate. Typically, the flow is a mixture of hydrogen and methane [55]. Using the CVD process, diamond can be synthesized with more control during growth and on a larger substrate.

2.1.2 Diamond type classification

Diamond generally is classified according to its nitrogen and boron impurities and the arrangement of the atoms in the lattice [56]. If the concentration of nitrogen atoms is higher than 5 ppm (typically 100 ppm to 3000 ppm), the

diamond is categorized as a type I diamond. A nitrogen concentration of less than 5 ppm categorizes the diamond as type II [57].

Type I and type II diamonds are further subdivided. Type Ia diamonds contain aggregated nitrogen, while type Ib diamonds contain single substitutional nitrogen atoms. For a type II diamond, depending on whether nitrogen or boron is the main impurity, the diamond is type IIa or type IIb, respectively [57]. More than 98% of natural diamonds are type I, and most CVD diamonds are type IIa [57].

2.2 Nitrogen-vacancy center

Nitrogen is the most common impurity in diamond [56] and is the building block of the NV center. In this section, we introduce certain physics of the NV center including its crystallographic structure in the diamond lattice, charge states, energy levels, isotope variations, and absorption and fluorescence behavior.

2.2.1 Crystallographic structure

The NV center is a point defect in the diamond lattice consisting of single substitutional nitrogen atom next to a vacancy. A diamond lattice with an NV center is shown in Fig. 2.1. The line that connects the nitrogen atom to the vacancy determines the NV axis. There are four possible orientations for an NV center based on the position of the NV axis in a single-crystal diamond.

2.2.2 Charge-state and isotope variations

The potential charge states of an NV center are neutral NV^0, negative NV^-, and positive NV^+. There have been studies regarding the ionization dynamics of single NV centers [58–60] as well as the conversion of charge states and its application for storing information [61]. However, the NV^- state has important optical and spin properties from the magnetometry perspective that is the focus of this thesis. Therefore, for the rest of this thesis, NV^- is denoted NV for simplicity.

There are six electrons associated with an ionized NV; two electrons are contributed from the dangling bond of the nitrogen atom, the three unpaired electrons of the vacancy come from the neighboring carbon atoms, and one electron is from a donor in the diamond lattice.

Nitrogen has two stable isotopes, ^{14}N with a natural abundance of 99.64% [62] and nuclear spin $I = 1$ and ^{15}N with a natural abundance of 0.36% [62] and nuclear spin $I = 1/2$. The variation in the nuclear spins of nitrogen atoms results in two types of NV centers with different hyperfine structures.

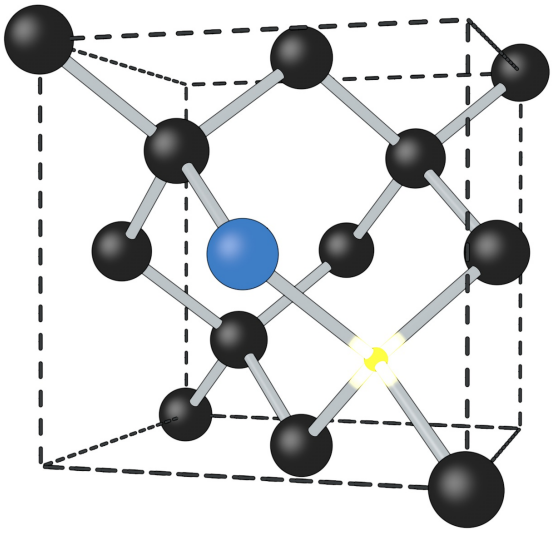

Figure 2.1: Crystal structure of the NV center in diamond. The carbon atoms and the nitrogen atom are shown in black and blue, respectively. The vacancy is represented by a yellow halo.

2.2.3 Electronic configuration and optical transition

The electronic energy levels of the NV center are depicted in Fig. 2.2. These energy levels consist of the spin-triplet ground state $|g\rangle$, spin-triplet excited state $|e\rangle$, and shelving state $|s\rangle$. The shelving state includes at least two intermediate singlet states [37]. In this thesis, we do not apply the transition between singlet states for magnetometry, and thus, we only consider one singlet state for the sake of simplicity.

The $m_s = 0$ and $m_s = \pm 1$ sublevels in the ground state and the excited state experience zero-field splittings of $D_g \sim 2.87$ GHz and $D_e \sim 1.42$ GHz, respectively, due to spin-spin interaction between unpaired electrons [63, 64]. The zero-field splitting is temperature dependent at a rate of -74.2 kHz/K [65].

The transition between $|g\rangle$ and $|e\rangle$ has an optical zero-phonon line at

637 nm [37]. This optical transition is mainly spin-conserving [49]. However, the shelving state is a nonradiative decay path that is spin-selective. We discuss its role in spin initialization in the next section. Although a 532 nm laser is generally used for excitation, NV centers can be excited in the wavelength range of $\sim$ 450 nm to 637 nm. The fluorescence emitted from an excited NV center has a wavelength in the range of $\sim$ 637 nm to 800 nm [4]. The broadband phonon-sideband at room temperature is the reason behind such a broad wavelength range.

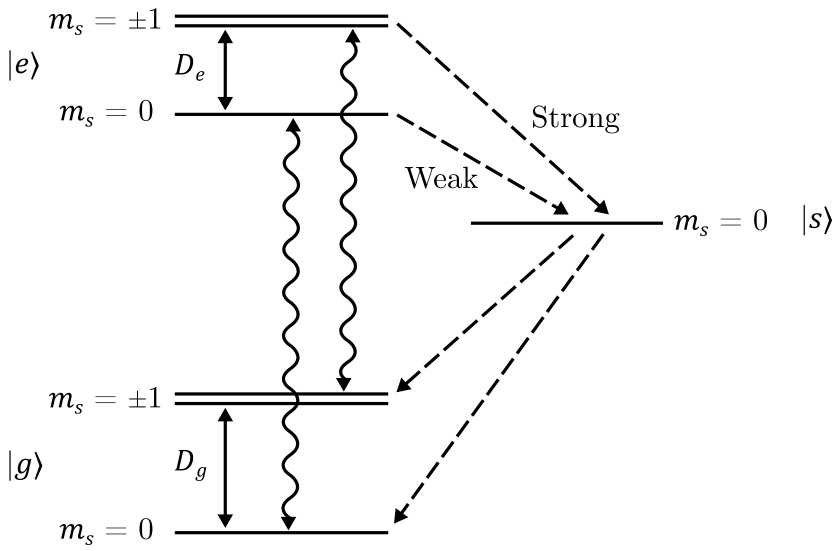

Figure 2.2: Energy level diagram of the NV center consisting of ground states $|g\rangle$, excited states $|e\rangle$, and a shelving state $|s\rangle$. Solid arrows indicate the zero-field splittings in the ground state D_g and the excited state D_e. The optical transitions are denoted by wiggly arrows. The nonradiative transitions are denoted by dashed arrows.

Diamond has a refractive index of $\sim$ 2.42 in the visible spectrum at room temperature [66]. The mismatch between the high refractive index of diamond and the refractive index of air as the collection medium causes total internal reflection inside the diamond. Therefore, most photons do not exit diamond, which results in low photon collection efficiencies.

Various approaches have been studied to increase the photon collection rate of NV centers. Some examples include fabricating solid immersion lenses [67, 68], applying a dielectric optical antenna [69], employing a silver mirror

[70], emitting through nanopillar waveguides [71], using a parabolic collector [72], coupling to a microcavity [73, 74], collecting light from the edges of the diamond [75], and placing prisms on the edges of the diamond [76, 77].

In the next section, we illustrate how to sense an unknown magnetic field by using the optical and spin properties of NV centers.

2.3 Spin-state initialization and readout

An important property of the NV center is that its spin state can be initialized and detected optically. The spin-selective property of the shelving state results in polarization of the electron spin of the NV center into $m_s = 0$ in the ground state under continuous optical pumping. Initialization is generally the first step in the sensing procedure. NV centers are excited by pumping with a 532 nm laser, which excites the NV center above the zero-phonon line. This excited NV center decays to $|e\rangle$ on a time scale of picoseconds [78] by nonradiative transitions. An NV center, which is initially at $m_s = 0$ in the ground state, absorbs a photon and is transferred to $m_s = 0$ in the excited state. As we discussed in the previous section, this transition is spin-conserving. Later, the NV center has a high probability of emitting a fluorescence photon and decaying to $m_s = 0$ in the ground state. Similarly, if an NV center is initially at $m_s = \pm 1$ in the ground state, it is transferred to $m_s = \pm 1$ in the excited state by absorbing a pump photon. However, in this case, it is more probable for the NV center to decay through the nonradiative decay path than in the case of $m_s = 0$. After several cycles of excitation and relaxation, NV centers accumulate at $m_s = 0$ in the ground state with high probability. As it is more probable for the NV center at $m_s = 0$ in the ground state to emit a fluorescence photon under optical pumping, it is often called the bright state, whereas $m_s = \pm 1$ is called the dark state for similar reason.

Continuously pumping a polarized NV center repeats the excitation and relaxation cycles. Therefore, the NV center continuously emits fluorescence photons with red wavelengths. Red photons can be detected by filtering the pump light using a long-pass optical filter. On the other hand, the $m_s = 0 \leftrightarrow m_s = \pm 1$ transition in the ground state is accessible with microwave (MW) wavelengths. If we generate an MW field with an MW antenna in the vicinity of an NV center and sweep the MW frequency while optically pumping the NV center, we hit the $m_s = 0 \leftrightarrow m_s = \pm 1$ transition at a certain MW frequency. Emitting an MW field resonant with the $m_s = 0 \leftrightarrow m_s = \pm 1$ transition transfers the population to the dark state, $m_s = \pm 1$, and thus reduces the emitted fluorescence counts. Monitoring the fluorescence count rate results in an optically detected magnetic resonance

(ODMR) spectrum. The population transfer from the bright state to the dark state is visible as a peak at ~ 2.87 GHz in the ODMR spectrum.

An external magnetic field lifts the degeneracy of $m_s = \pm 1$ in the ground state as shown in Fig. 2.3. The splitting is proportional to the applied magnetic field B, increasing at $2\gamma_e B$ where γ_e is the electron gyromagnetic ratio, and $\gamma_e/2\pi \sim 28025$ MHz/T [79]. In the presence of a static magnetic field, the ODMR spectrum contains two separate peaks generated from electron spin resonances of the $m_s = 0 \leftrightarrow m_s = -1$ and $m_s = 0 \leftrightarrow m_s = +1$ transitions.

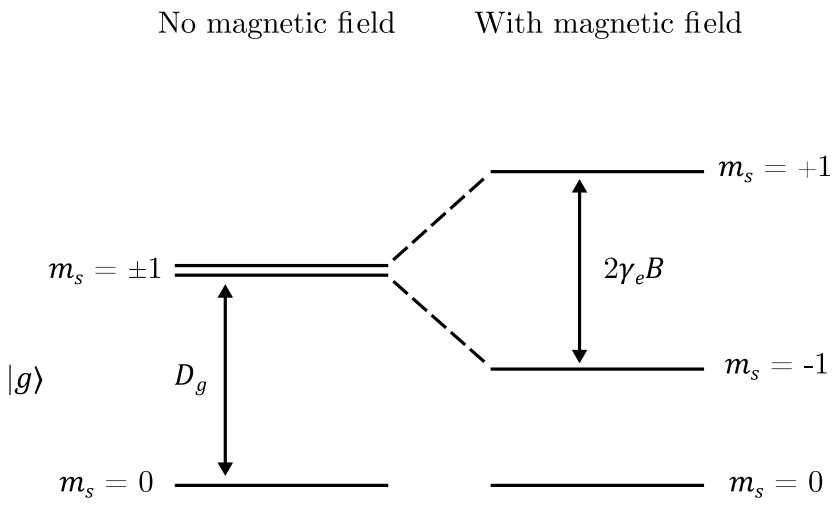

Figure 2.3: Schematic of the NV ground state electronic structure in the absence and in the presence of a magnetic field. The degeneracy of the ground state is lifted by a magnetic field, resulting in an energy difference of $2\gamma_e B$.

The ODMR spectrum in the absence of a magnetic field is plotted in Fig. 2.4 (a). The frequency of this peak corresponds to zero-field splitting. The ODMR spectrum in Fig. 2.4 (b) indicates the presence of a static magnetic field in the environment.

There are four possible spin orientations for NV centers in single-crystal diamond. The angle between each different pair of the possible orientations is 109.4°. For ensembles of NV centers, four spin orientations result in eight possible peaks in the ODMR spectrum in the presence of an external static magnetic field. Moreover, the resonance frequency associated with each spin

transition depends on the magnitude and direction of the magnetic field [80].

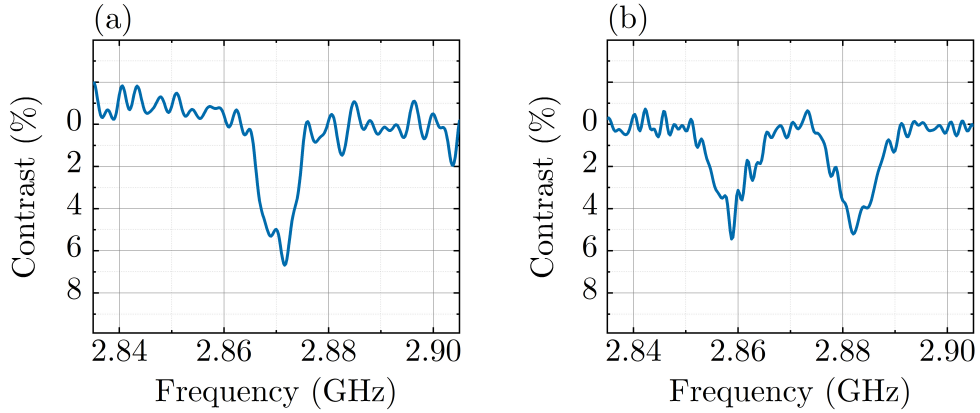

Figure 2.4: ODMR spectra (a) in the absence of a magnetic field and (b) in the presence of an external magnetic field. The magnetic field lifts the degeneracy of the $m_s = \pm 1$ states and results in two separate peaks in the ODMR spectrum.

2.4 Rabi oscillation and spin coherence times

Applying an MW field resonant with the $m_s = 0 \leftrightarrow m_s = +1$ or resonant with $m_s = 0 \leftrightarrow m_s = -1$ transitions coherently drives the population between the two spin states. The pulse sequence for measuring these Rabi oscillations is shown in Fig. 2.5. For the $m_s = 0 \leftrightarrow m_s = +1$ transition, a laser pulse initializes the spin states to $|0\rangle$. Then, an MW pulse transfers the spin population between $|0\rangle$ and $|+1\rangle$ spin states. The spin state is detected by exciting the NV center with a laser pulse and recording the emitted fluorescence. The population transfer can be measured as a function of the length of the MW pulse. For an ensemble of spins, the Rabi signal decays due to inhomogeneous broadening and also detuning of hyperfine transitions [81]. The Rabi frequency, $\Omega/2\pi$, depends on the amplitude of the MW field applied by:

$$\Omega = \gamma_e B. \tag{2.1}$$

In practice, the coherence of the electron spin ensembles is dominated by dephasing time T_2^*. Inhomogeneity in the environment causes dephasing of the NV spins in diamond. Diamond is composed of carbon atoms. The most abundant carbon isotope is ^{12}C at a natural abundance of 98.89% [62]. ^{12}C is nuclear spin free and therefore not magnetically active. In contrast, the

^{13}C isotope, at a natural abundance of 1.11% [62] and nuclear spin $I = 1/2$, is the main source of paramagnetic impurities in the spin bath. Magnetic field fluctuations from the local spin bath contribute to NV spin dephasing.

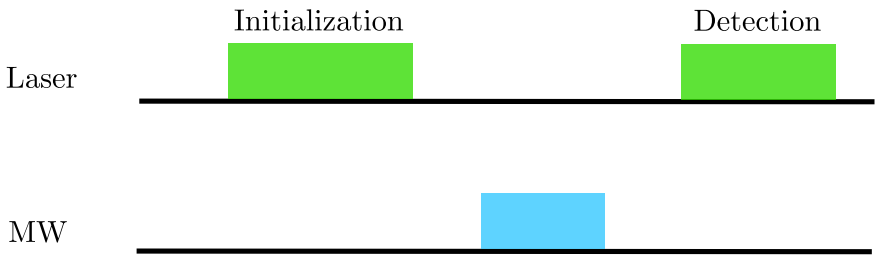

Figure 2.5: Pulse sequence for measuring Rabi oscillation.

Ramsey measurement is a technique for obtaining T_2^*. The pulse sequence is shown in Fig. 2.6. First, the spin state is initialized in the $|0\rangle$ state with a laser pulse. If the $m_s = 0 \leftrightarrow m_s = +1$ transition is considered, an initial $\pi/2$ MW pulse transfers the spin population to the superposition of the $|0\rangle$ and $|+1\rangle$ states. The spin precesses for time τ due to coupling with magnetic fields. A second MW pulse projects the population to the $|+1\rangle$ state. The spin state is detected optically by measuring the fluorescence after the last laser pulse. The free induction decay curve is the outcome of the Ramsey measurement, and its decay envelope corresponds to T_2^*.

In this thesis, we performed Rabi and Ramsey measurements with an ensemble of NV centers inside an optical cavity. The results are presented in the next chapter.

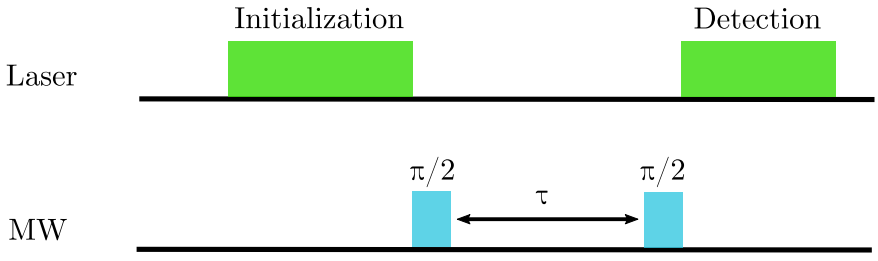

Figure 2.6: Ramsey pulse sequence for measuring spin dephasing time.

Moreover, the spins experience decoherence and relaxation characterized by T_2 and T_1, respectively. The dominant source of the spin decoherence is the interaction with nearby spins. The coherence time can be measured with a Hahn echo pulse sequence. A long spin coherence time of $T_2 = 1.8$ ms at room temperature has been obtained for ultrapure, isotopically engineered diamond with 99.9% ^{12}C concentration [82].

The relaxation process causes the spins to flip and thus returns the polarized spin population to a thermally mixed state. This process is attributed to spin interaction with phonons in the diamond lattice. Long relaxation times T_1 of up to 8 hours have been demonstrated with NV centers at cryogenic temperatures [83].

2.5 Hamiltonian formalism

The spin Hamiltonian of NV centers in the presence of an external magnetic field can be formulated in terms of different contributions as [37, 84]:

$$\mathcal{H} = \mathcal{H}_{ZFS} + \mathcal{H}_{HF} + \mathcal{H}_I + \mathcal{H}_{HF,ext} + \mathcal{H}_B, \tag{2.2}$$

where $\mathcal{H}_{ZFS}$ denotes the zero-field splitting contribution, the hyperfine interaction of the NV electron spin with nitrogen nuclear spin is represented by $\mathcal{H}_{HF}$, $\mathcal{H}_I$ is the higher order quadrupole interaction, $\mathcal{H}_{HF,ext}$ indicates the hyperfine interaction of the NV electron spin with external nuclear spins, and the interaction with the magnetic field is included in $\mathcal{H}_B$.

Substituting each term and denoting the electron spin and nuclear spin matrices with S and I, respectively, the Hamiltonian becomes:

$$\frac{\mathcal{H}}{\hbar} = S^T \mathcal{D} S + S^T \mathcal{A}_{HF} I + I^T \mathcal{Q}_I I + \sum_{i=1}^{N} S^T \mathcal{A}_{HF} I_i + \frac{\mu_B g_e}{\hbar} S^T B, \tag{2.3}$$

where $\mathcal{D}$ is the zero-field splitting tensor, $\mathcal{A}_{HF}$ indicates the hyperfine interaction tensor, $\mathcal{Q}$ represents the quadrupole interaction tensor, μ_B is the Bohr magneton, and g_e is the g-factor.

Equation 2.3 is simplified by diagonalizing each tensor with respect to the NV axis, neglecting the strain in the diamond lattice, and discarding the interaction with external nuclear spins:

$$\frac{\mathcal{H}}{\hbar} = \mathcal{D}(S_z^2 - \frac{2}{3}) + A_\perp(S_x I_x + S_y I y) + A_\parallel S_z I_z + \mathcal{Q}(I_z^2 - \frac{2}{3}) + \gamma_e S_z B_z, \tag{2.4}$$

where $A_\perp$ and $A_\parallel$ are non-axial and axial magnetic hyperfine parameters, respectively, and $\gamma_e = \mu_B g_e / \hbar$ denotes the electron gyromagnetic ratio.

2.6 Rate equation model

The ODMR spectrum can be modeled by considering a Hamiltonian that incorporates the resonant drive between two spin states in the ground state. We consider five electronic levels for NV centers as illustrated in Fig. 2.7.

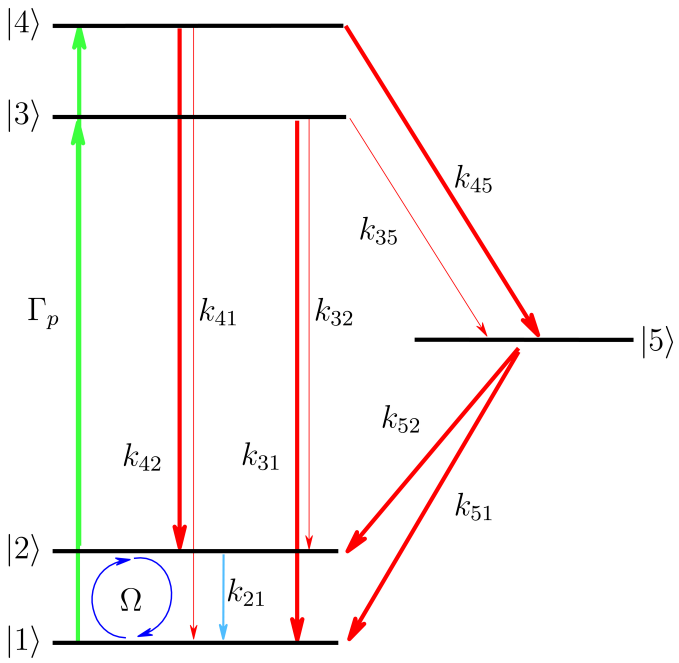

Figure 2.7: Schematic of NV center electronic levels to model transitions and the ODMR spectrum. The NV centers are excited with a rate of Γ_p. The decay between two states is shown by k_{ab}, and Ω corresponds to the Rabi frequency of the MW drive. The longitudinal relaxation rate is denoted by blue arrow. Figure taken from Ref. [85].

Using a rotating reference frame with the MW drive and the rotating wave approximation, the system of equations becomes:

$$\dot{\rho}_{11} = -\Gamma_p\rho_{11} + k_{31}\rho_{33} + k_{41}\rho_{44} + k_{51}\rho_{55} - \frac{k_{21}}{2}(\rho_{11} - \rho_{22}) - \frac{i}{2}\Omega(\rho_{12} - \rho_{21}), \tag{2.5}$$

$$\dot{\rho}_{22} = -\Gamma_p\rho_{22} + k_{32}\rho_{33} + k_{42}\rho_{44} + k_{52}\rho_{55} - \frac{k_{21}}{2}(\rho_{22} - \rho_{11}) + \frac{i}{2}\Omega(\rho_{12} - \rho_{21}), \tag{2.6}$$

$$\dot{\rho}_{33} = \Gamma_p\rho_{11} - (k_{35} + k_{32} + k_{31})\rho_{33}, \tag{2.7}$$

$$\dot{\rho}_{44} = \Gamma_p\rho_{22} - (k_{45} + k_{42} + k_{41})\rho_{44}, \tag{2.8}$$

$$\dot{\rho}_{55} = k_{45}\rho_{44} + k_{35}\rho_{33} - (k_{52} + k_{51})\rho_{55}, \tag{2.9}$$

$$\dot{\rho}_{12} = -(\gamma_2' - i\Delta)\rho_{12} + \frac{i}{2}\Omega(\rho_{22} - \rho_{11}), \tag{2.10}$$

$$\dot{\rho}_{21} = -(\gamma_2' + i\Delta)\rho_{21} - \frac{i}{2}\Omega(\rho_{22} - \rho_{11}), \tag{2.11}$$

where Γ_p is the pump rate, k_{ab} is the decay between states a and b, and $\Delta = (\omega_c - \omega_0)$ is the detuning between the MW angular frequency and the angular frequency of the electron spin resonance. We define the spin and optical dephasing rates as $\gamma_2 = k_{21}/2 + \gamma_2^*$ and $\gamma_2' = \gamma_2 + \Gamma_p/2$, respectively.

The steady-state solutions for the ground-state populations become:

$$\rho_{11}^{ss} = \left[1 + \Xi + \frac{\Gamma_p}{K_3} + \frac{\Gamma_p\Xi}{K_4} + \frac{k_{35}\Gamma_p}{K_3K_5} + \frac{k_{45}\Gamma_p\Xi}{K_5K_4}\right]^{-1}, \tag{2.12}$$

$$\rho_{22}^{ss} = \left[1 + \frac{1}{\Xi} + \frac{\Gamma_p}{K_4} + \frac{\Gamma_p}{K_3\Xi} + \frac{k_{45}\Gamma_p}{K_4K_5} + \frac{k_{35}\Gamma_p}{K_5K_3\Xi}\right]^{-1}, \tag{2.13}$$

$$\Xi = \frac{\left[\left(\frac{k_{21}}{2}\right) + \left(\frac{\Gamma_p(k_{32}K_5 + k_{52}k_{35})}{K_3K_5}\right) + \left(\frac{\Omega^2\gamma_2'}{2(\gamma_2'^2 + \Delta^2)}\right)\right]}{\left[\Gamma_p + \left(\frac{k_{21}}{2}\right) - \left(\frac{\Gamma_p(k_{42}K_5 + k_{52}k_{45})}{K_4K_5}\right) + \left(\frac{\Omega^2\gamma_2'}{2(\gamma_2'^2 + \Delta^2)}\right)\right]}, \tag{2.14}$$

where:

$$K_3 = k_{31} + k_{32} + k_{35}, \tag{2.15}$$

$$K_4 = k_{41} + k_{42} + k_{45}, \tag{2.16}$$

$$K_5 = k_{51} + k_{52}. \tag{2.17}$$

The steady-state population of the excited state defines the ODMR spectrum as:

$$\mathcal{I}_{cw} = \big(\frac{k_{31}+k_{32}}{K_3}\big)\rho_{33}^{ss} + \big(\frac{k_{41}+k_{42}}{K_4}\big)\rho_{44}^{ss}, \tag{2.18}$$

which is proportional to the steady-state population of the ground state:

$$\mathcal{I}_{cw} = \big(\frac{k_{31}+k_{32}}{K_3}\big)\frac{\Gamma_p}{K_3}\rho_{11}^{ss} + \big(\frac{k_{41}+k_{42}}{K_4}\big)\frac{\Gamma_p}{K_4}\rho_{22}^{ss}. \tag{2.19}$$

The ODMR spectrum can be represented by a Voigt profile, which is the convolution of the Gaussian and Lorentzian densities. For the case of homogeneous broadening, the ODMR spectrum is equivalent to the Lorentzian profile:

$$\mathcal{S}_{cw}(\omega_c) = \mathcal{I}_{cw}^{\Omega=0}\left(1 - \frac{\mathcal{C}\gamma^2}{\Delta^2+\gamma^2}\right) \equiv \mathcal{I}_{cw}, \tag{2.20}$$

where:

$$\mathcal{C} = 1 - \frac{\mathcal{I}_{cw}^{\Delta=0}}{\mathcal{I}_{cw}^{\Omega=0}}, \qquad 2\gamma \approx \gamma_2^* + \frac{1}{2\pi}\sqrt{\gamma_2^2 + \frac{\gamma_2\Omega^2}{k_{21}+\Gamma_p}}, \tag{2.21}$$

where $\mathcal{I}_{cw}^{\Omega=0}$ is the ODMR spectrum when $\Omega = 0$, $\mathcal{C}$ is the contrast, and γ is the half width at half maximum.

We apply this model in Chapter 4 and Chapter 5 to simulate ODMR spectra. Decay rate values were extracted from Ref. [86].

2.7 Continuous-wave magnetometry

There are various protocols to measure an external magnetic field with NV centers. Here, we describe the straightforward method that we applied in our experiments. Information regarding unknown magnetic fields in the environment can be extracted from the shift in the resonance frequency of the NV electron spins [87, 88]. Initially, a known static magnetic field splits the ODMR peaks of the four possible NV orientations in a bulk diamond. Then, the MW field is set to the frequency where the highest slope of the ODMR of one of the NV orientations is obtained. The highest slope is the most sensitive to changes in the magnetic field. Any unknown magnetic field shifts the electron spin resonance frequency due to the Zeeman effect, changing the fluorescence signal by an amount proportional to the slope. The changes in the resonance frequency are detected by monitoring the fluorescence signal.

Moreover, the vector components of the external field can be reconstructed by monitoring the shifts in the resonance frequencies of the three NV orientations.

Alternative magnetic field sensing techniques have been demonstrated that use NV centers, for instance, magnetometry by recording the fluorescence change at the ground-state level anticrossings of NV centers [89, 90] and by measuring the variations in the infrared absorption of the shelving states [91–93]. In Chapter 6, we introduce a different magnetometry method that uses NV centers based on measuring the absorption of the pump light [94].

Continuous-wave magnetometry is the basis of the magnetic field sensing in all the experiments in this thesis. Additionally, magnetic field sensing can be performed using pulsed-field magnetometry and dynamical decoupling schemes [95, 96].

In the next chapter, we discuss the experimental realization of magnetic field sensing with an ensemble of NV centers using the same method we introduced in this section.

Chapter 3

Experimental Framework

We present the framework for the experimental realization of magnetic field sensing with an ensemble of NV centers. We begin by introducing the diamond crystal and the required components for controlling the spin-state such as delivering an MW field and optical excitation. Next, we discuss the optical cavity and stabilization method, and the phase-sensitive detection technique. Finally, the experimental setup for the electron spin resonance measurements is presented.

3.1 Diamond sample

We obtained our diamond crystals from Element Six. The samples that were used for all experiments in this thesis are untreated single-crystal CVD diamonds with dimensions of 6.0 mm x 6.0 mm x 1.2 mm. These CVD-grade diamonds have type IIa optical properties; the absorption in the optical range is mainly attributable to nitrogen, and the concentration of nitrogen is reported to be less than 5 ppm by the provider.

If we assume that the concentration ratio between the sum of the neutral and positively charged substitutional nitrogen centers, $[N^0] + [N^+]$, and the negatively charged NV centers, $[NV^-]$, is approximately 300:1 [97], then $[NV^-]$ is in the range of ~ 17 ppb. We estimated $[NV^-]$ independently through measurements of the fluorescence count rate using a confocal setup and obtained a concentration of ~ 0.16 ppb.

The diamond was cleaned each time before mounting the sample and performing an experiment. We cleaned the diamond in a boiling triacid solution of sulfuric acid 95%, nitric acid 65%, and perchloric acid 70% at a ratio of 1:1:1 for approximately three hours.

In addition, we irradiated certain samples with electrons and annealed,

cut, and polished certain others. However, we did not use any of them for the published studies, and therefore, these samples are not discussed in this thesis.

3.2 Spin-state control and readout

In this section, we discuss two main components for controlling the spin state, optical and MW drive.

3.2.1 Microwave delivery

We developed various split-ring resonators [98, 99] to deliver a uniform MW field across a bulk diamond [100]. We simulated the resonance using COMSOL and constructed the resonators in-house by a photolithography method. Figure 3.1 shows an example of the patterning.

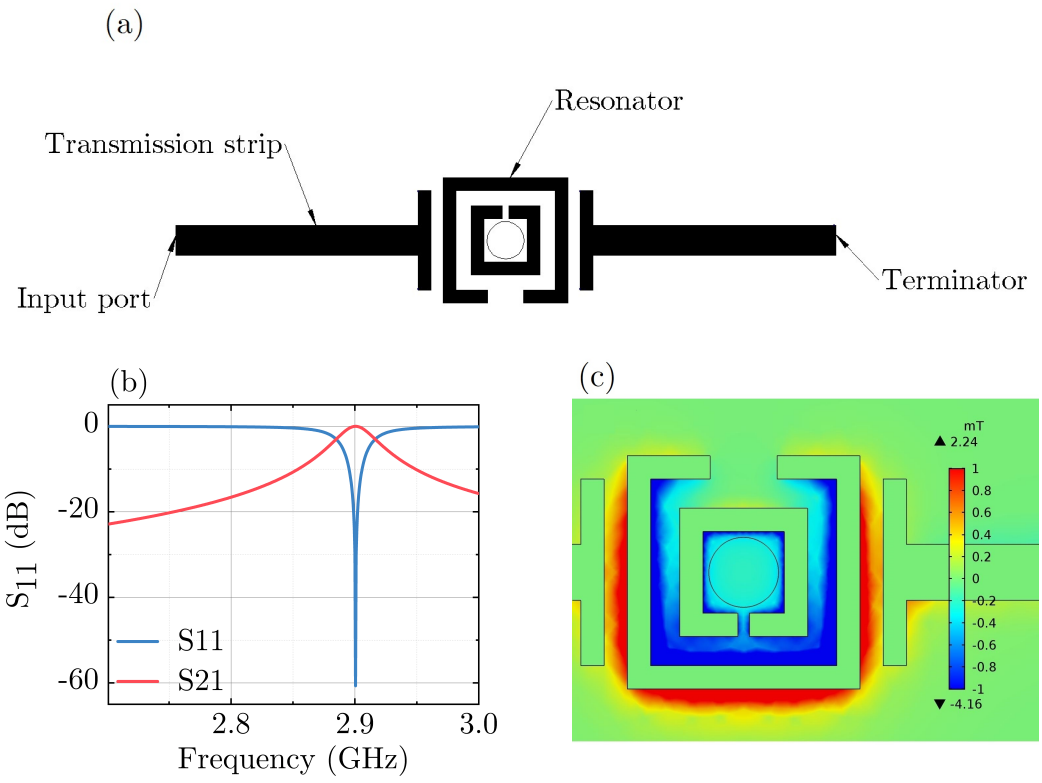

Figure 3.1: (a) Pattern of a split-ring resonator. (b) Simulated S_{11} and S_{21} components of the scattering parameters. (c) Simulated magnetic field of the same split-ring resonator as in (a) with a 16 W input power.

To fabricate a printed circuit board, we used an RO4003C laminate from the Rogers Corporation that is suitable for MW designs. This hydrocarbon ceramic laminate has a dielectric constant of 3.38 and a high thermal conductivity. Next, we added a layer of photoresist on the laminate. Then, we put a mask with a split-ring resonator pattern on the laminate and exposed it to ultraviolet light. We developed the board with sodium carbonate and later etched the copper with sodium persulfate. Finally, the residual resist was removed with sodium hydroxide.

Figure 3.2 (a) shows the S_{11} component of the scattering parameters [101] for a fabricated split-ring resonator, which is measured with a network analyzer. The standing-wave ratio [101] of the same resonator is depicted in Fig. 3.2 (b) with a resonance centered at 2.89 GHz. In our experiments, the MW signal was generated with a SG394 RF signal generator from Stanford Research Systems.

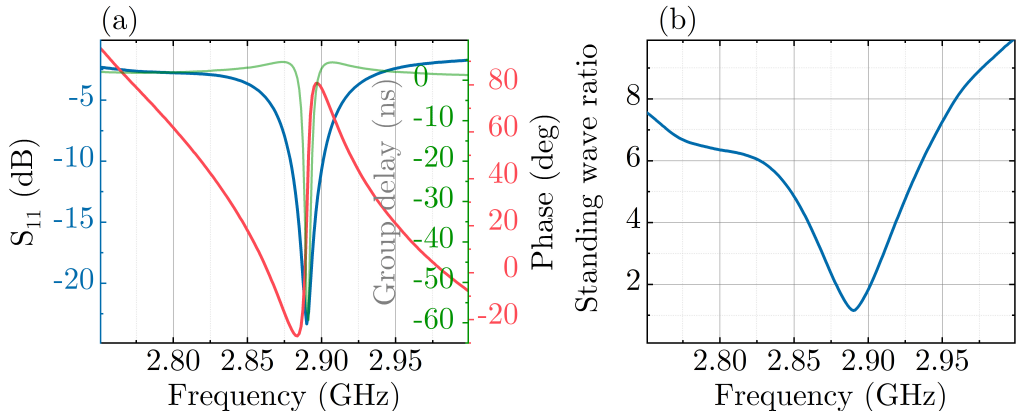

Figure 3.2: Example of the measured (a) S_{11} component of the scattering parameters and (b) standing-wave ratio of a fabricated split-ring resonator. The diamond was glued on the board.

3.2.2 Optical drive

We optically pumped the NV centers with a continuous-wave linearly polarized 532 nm laser. We used a Verdi G SLM Coherent laser, which possesses a single longitudinal mode with a noise of root mean square $< 0.02\%$ from 10 Hz to 100 MHz. We rotated the polarization of the laser beam to p-polarized to minimize the reflection from the diamond, which was mounted at its Brewster angle.

3.2.3 Optical cavity

We constructed a linear optical cavity with two concave mirrors. The substrates and coatings were provided by Laseroptik with measured reflectivities of $R_1 = 94.8\% \pm 0.1\%$ and $R_2 = 99.8\% \pm 0.1\%$ at a pump wavelength of 532 nm. Both mirrors had anti-reflection coatings for 532 nm wavelengths on the flat ends. The mirrors, with radii of curvature of 10 cm, were placed in a confocal configuration forming a cavity length of L =10 cm. As a consequence, the beam in the optical cavity had a minimum waist of 92 μm with a Rayleigh length of $\sim$ 50 mm.

The resonances of an optical cavity are spaced in frequency with the distance of the free spectral range $c/2L$ where c is the speed of light and $2L$ is the round-trip optical path length. The ratio of the free spectral range to the full width at half maximum is defined as the finesse, which is a parameter that is used to measure the quality of the cavity. The finesse can also be calculated as [102]:

$$F = \frac{\pi\sqrt{\rho}}{1-\rho}, \tag{3.1}$$

where ρ is the cumulative round-trip loss product and is defined as:

$$\rho = \sqrt{R_1 R_2 e^{-\alpha}}, \tag{3.2}$$

and α is the propagation loss coefficient. For a lossless optical cavity where $e^{-\alpha} = 1$, the finesse solely depends on the product of R_1R_2. For the case of our mirrors, the finesse was calculated as $F = 113.4 \pm 4.4$. This calculation was confirmed by a measured finesse of $F = 114 \pm 0.1$, which is shown in Fig. 3.3. However, incorporating the diamond in the center of the optical cavity at its Brewster angle $\theta_B = 67°$ introduced more losses inside the cavity and reduced the finesse. For a loaded cavity, the finesse was measured as $F = 45.1 \pm 0.1$. This corresponded to $\sim 8\%$ losses, $e^{-\alpha} = 0.92$, occurring by passing the laser beam through diamond.

The intensities of transmitted, reflected, or intracavity electromagnetic fields can be calculated classically using the equations of the multiple interferences of waves. The ratio of the transmitted power P_t, reflected power P_r, and intracavity power P_{cav}, to the input power P_{in} is [102]:

$$\frac{P_t}{P_{in}} = \frac{T_1 T_2 e^{-\alpha}}{|1-\rho|^2}, \tag{3.3}$$

$$\frac{P_r}{P_{in}} = \frac{(R_1 - (R_1 + T_1)\rho)^2}{R_1|1-\rho|^2}, \tag{3.4}$$

$$\frac{P_{cav}}{P_{in}} = \frac{T_1}{|1-\rho|^2}, \tag{3.5}$$

where T_1 and T_2 are the transmissions of the first and second mirrors, respectively. If the mirror loss is negligible, then $R_i + T_i = 1$.

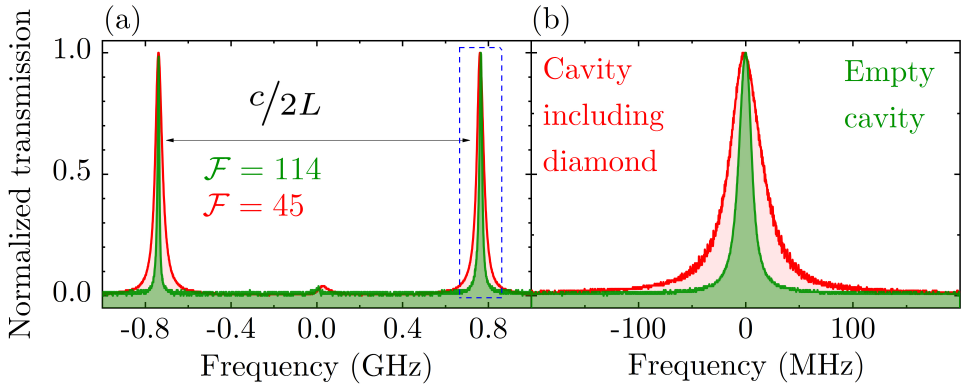

Figure 3.3: (a) Transmission spectrum of the optical cavity as a function of the frequency of the incident beam without (green) and with (red) the diamond. The finesse of the cavity including diamond reduces to 45 compared with the empty cavity with a finesse of 114. (b) Enlargement of a resonance peak from (a). Adding the diamond increases the linewidth from approximately 6.5 MHz to 17 MHz. Figure taken from Ref. [85].

The responses of the cavity can be divided into three cases [103]. If $R_1 > R_2 e^{-\alpha}$, the cavity is undercoupled. The reflected beam is dominant by the incoming field that is promptly reflected by the first mirror and never enters the cavity. If $R_1 = R_2 e^{-\alpha}$, the cavity is impedance-matched. In this case, the amplitudes of the promptly reflected field and the leakage field from the cavity are equal, but the fields are 180° out of phase. Therefore, the beams interfere destructively and cancel out each other completely. In an impedance-matched cavity, the incoming beam is transmitted through the cavity, and there is no reflected light. This phenomenon is equivalent to the impedance-matching in electrical resonators. The last case is when $R_1 < R_2 e^{-\alpha}$. This case represents an overcoupled cavity, which means the reflected beam is dominated by the leakage light from the cavity.

In the case of our cavity, the diamond introduces $\sim 8\%$ round-trip losses, and thus $R_1 > R_2 e^{-\alpha}$. The cavity was slightly undercoupled. Building up the highest intracavity power requires an impedance-matched cavity. If we assume that R_2 is fixed, using our diamond, the impedance-matched point can be reached by altering the reflectivity of the first mirror. We investigate

this alteration by plotting the ratio of P_{cav}/P_{in} as a function of R_1 using Eq. 3.5, which is illustrated in Fig. 3.4. The impedance-matching is achieved if approximately $R_1 = 91.8\%$ corresponding to $\max(P_{cav}/P_{in}) = 12.22$. For the case of our undercoupled cavity, $P_{cav}/P_{in} = 11.57$. Although this is not the optimal value, it is very close to the maximum.

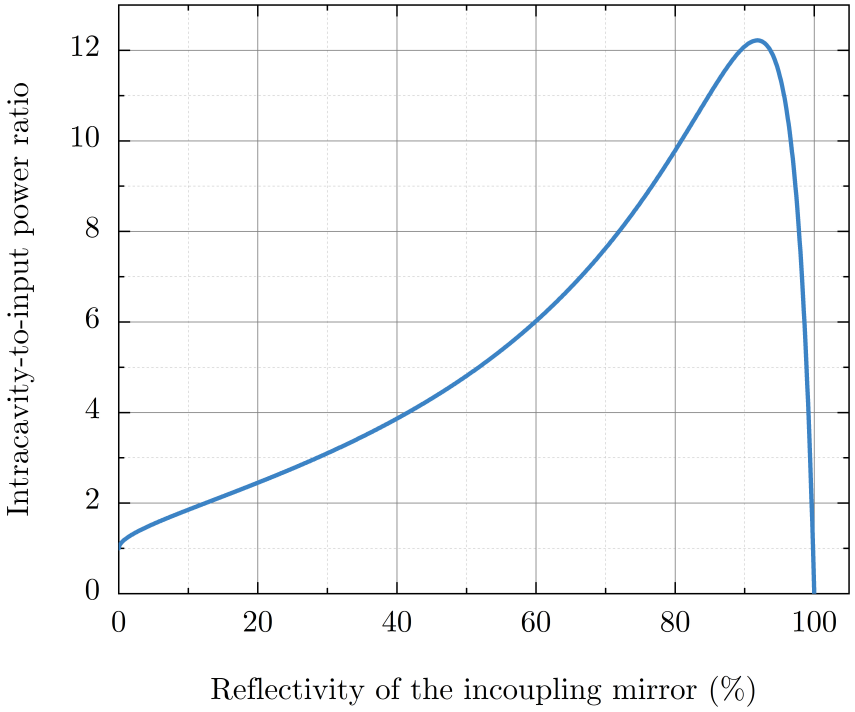

Figure 3.4: Ratio of the intracavity power to the input power as a function of the reflectivity of the incoupling mirror. The reflectivity of the second mirror remains unchanged at 99.8%. The diamond sample introduces 8% losses, $e^{-\alpha} = 0.92$. The highest P_{cav}/P_{in} is 12.22, while $P_{cav}/P_{in} = 11.57$ for the case of our cavity.

3.2.4 Stabilization techniques

We applied the Pound-Drever-Hall (PDH) technique for locking the optical cavity [104, 105]. Here, we briefly introduce the PDH model. To begin, we modulate the phase of the incident light with an electro-optic modulator. We describe the electric field of the cavity input light as $E_{in} = E_0 e^{i\omega_c t}$, where E_0 is the amplitude, ω_c denotes the angular frequency of the carrier, and t is time. If we modulate the phase with a sine-wave, the phase-modulated field

is represented by:

$$E_{in} = E_0 e^{i\omega_c t + i\beta \sin(\omega_m t)}, \tag{3.6}$$

where β is the modulation index, and ω_m is the modulation angular frequency. Using the Jacobi-Anger expansion [106], Eq. 3.6 can be expressed as:

$$E_{in} = E_0 e^{i\omega_c t} \sum_{n=-\infty}^{\infty} J_n(\beta) e^{in\omega_m t}, \tag{3.7}$$

where J_n is the n-th Bessel function of the first kind. Applying the relation $J_{-n}(\beta) = (-1)^n J_n(\beta)$, Eq. 3.7 becomes:

$$E_{in} = E_0[J_0(\beta)e^{i\omega_c t} + \sum_{n=1}^{\infty} J_n(\beta)e^{i(\omega_c + n\omega_m)t} + \sum_{n=1}^{\infty}(-1)^n J_n(\beta)e^{i(\omega_c - n\omega_m)t}], \tag{3.8}$$

where all infinite number sidebands are included. Assuming that most of the power of the phase-modulated incident beam is in the carrier and the first-order sidebands, the incident field becomes:

$$E_{in} = E_0[J_0(\beta)e^{i\omega_c t} + J_1(\beta)e^{i(\omega_c + \omega_m)t} - J_1(\beta)e^{i(\omega_c - \omega_m)t}]. \tag{3.9}$$

Equation 3.9 shows that three different beams enter the cavity, a carrier with angular frequency ω_c and two sidebands with angular frequencies $\omega_c \pm \omega_m$. Next, we calculate the transmitted power of the cavity, because at the end, we measure the power with a photodetector. The transmitted power is calculated as follows:

$$\begin{aligned} P_t = {} & P_c|T(\omega_c)|^2 + P_s[|T(\omega_c + \omega_m)|^2 + |T(\omega_c - \omega_m)|^2] \\ & + 2\sqrt{P_c P_s}\big\{\mathrm{Re}[T(\omega_c)T^*(\omega_c + \omega_m) - T^*(\omega_c)T(\omega_c - \omega_m)]\cos(\omega_m t) \\ & + \mathrm{Im}[T(\omega_c)T^*(\omega_c + \omega_m) - T^*(\omega_c)T(\omega_c - \omega_m)]\sin(\omega_m t)\big\} + (\text{terms with } 2\omega_m), \end{aligned} \tag{3.10}$$

where $T(\omega) = E_t/E_{in}$ is the transmission coefficient of the optical cavity, $P_c = J_0^2(\beta)|E_0|^2$ is the power in the carrier, and $P_s = J_1^2(\beta)|E_0|^2$ is the power in the first-order sidebands. There are two oscillating terms in Eq. 3.10. One can be eliminated by selecting the modulation frequency. The remaining oscillating term is isolated by mixing the output of the photodetector with the modulation signal of $\omega_m t$ and then low-pass filtering the combined signal. Last, we measure $T(\omega_c)T^*(\omega_c + \omega_m) - T^*(\omega_c)T(\omega_c - \omega_m)$ and extract an error signal, which is antisymmetric around the cavity resonance. The servo controller uses this error signal as feedback for active stabilization. The feedback is sent to a piezo actuator attached to the incoupling mirror, which keeps the cavity on resonance by changing the length of the cavity.

3.3 Phase-sensitive detection

We used a lock-in amplifier (LIA) to extract the ODMR signal from the noisy environment. The LIA performs phase-sensitive detection (PSD), where the signal is modulated at a modulation frequency in the kHz range. A reference signal with identical frequency to the modulation is generated and forwarded to the LIA. The LIA amplifies only the signal at the reference frequency and a narrow band-pass filter excludes all other noise components [107]. We assume that the signal takes the form of $V_s\sin(\omega_s t + \theta_s)$, where V_s is the amplitude of the signal, and θ_s is the phase. Similarly, the LIA reference takes the form of $V_r\sin(\omega_r t + \theta_r)$. The output of the phase-detection is the product of two signals:

$$V_{output} = V_s V_r \sin(\omega_s t + \theta_s)\sin(\omega_r t + \theta_r), \tag{3.11}$$

$$V_{output} = 0.5 V_s V_r \big\{\cos([\omega_s - \omega_r]t + \theta_s - \theta_r) - \cos([\omega_s + \omega_r]t + \theta_s + \theta_r)\big\}. \tag{3.12}$$

If the signal frequency is the same as the reference frequency, $\omega_s = \omega_r$, and the output signal is followed by a low-pass filter, the output becomes a DC signal [108]:

$$V_{output} = 0.5 V_s V_r \cos\theta. \tag{3.13}$$

The phase difference between the signal and the reference, $\theta = \theta_s - \theta_r$, can be removed by tuning the phase of the reference frequency. Therefore, the output is directly proportional to the signal amplitude:

$$V_{output} = 0.5 V_s V_r, \tag{3.14}$$

and the noise frequency components other than the reference frequency are eliminated.

For our measurements, we used SR510 and SR850 LIAs from Stanford Research Systems. The modulated frequency was generated with a SG394 RF signal generator, also from Stanford Research Systems. To emphasize the importance of the PSD, we measured ODMR signals both without and with the LIA. The results are shown in Fig. 3.5 (a) and Fig. 3.5 (b), respectively. In Fig. 3.5 (a), we show measurements with no frequency modulation of the MW signal, detected with an avalanche photodiode using a 1 ms time measurement and averaged over 100 repetitions. In Fig. 3.5 (b), we used the PSD technique with the signal detected by a biased silicon photodiode averaged over 10 measurements. The time constant, modulation frequency,

and modulation depth in this case were 1 s, 30 kHz, and 0.5 MHz, respectively. For both (a) and (b), the laser input power was 250 mW, and the MW power was 24 dBm. The ODMR signal in (a) is much noisier than that in (b), which makes it impractical for magnetometry.

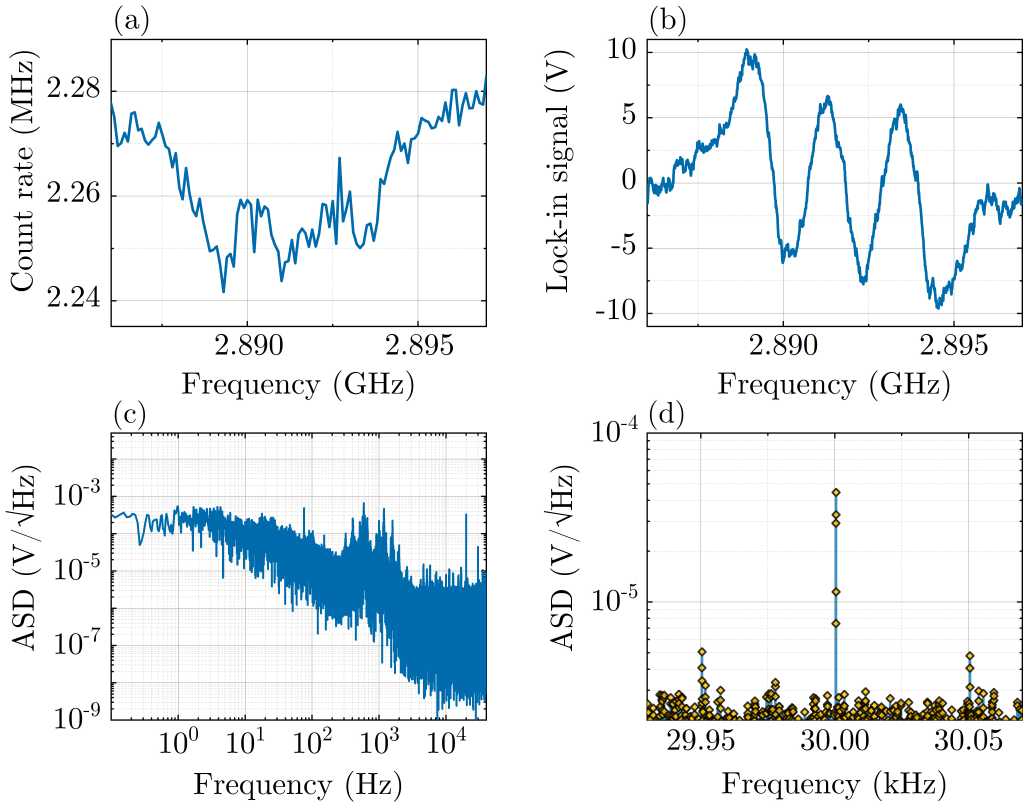

Figure 3.5: (a) Direct measurement of the ODMR signal using an avalanche photodiode. (b) Measured phase-modulated ODMR signal with a PSD technique using a silicon photodiode. (c) Noise density of the locked cavity before demodulation with LIA, highlighting the significant noise at frequencies lower than 3 kHz. (d) Zoomed in view of (c) around the modulation frequency of 30 kHz. Two sidebands at 30 ± 0.05 kHz originate from the beating of the modulation frequency with a 50 Hz magnetic noise from the environment.

Figure 3.5 (c) depicts the amplitude spectral density (ASD) of a time trace before demodulation with LIA. The time trace was measured on the maximum slope of the ODMR while the MW was frequency-modulated at 30 kHz. This time trace shows notable noise at frequencies lower than 3 kHz. However, the PSD sets the measurement frequency to a higher frequency (modulation frequency) and thus enables us to measure much weaker signals

that otherwise would have been lost in the noise at the lower frequencies. Figure 3.5 (d) is a zoomed in view of (c) around the modulation frequency. The signal at 30 kHz is above the noise floor showing a good signal-to-noise ratio. Two sidebands at 30 ± 0.05 kHz are also visible. The beating between the modulation frequency with the magnetic noise produces sidebands. These sidebands are signatures of a 50 Hz magnetic noise in the environment.

There are a few parameters that we can set for a PSD measurement. The gain settings, time constant, slope of the low-pass filter, and dynamic reserve are some of main parameters whose values and noise floors depend on the LIA device and can be different from one another. We characterized these parameters for our LIAs SR510 and SR850. Examples of such measurements are shown in Fig. 3.6 for SR850. All the noise densities were measured with a 50 Ω terminator attached to the input of the LIA. For each measurement in Fig. 3.6, we fixed other parameters such as a gain of 500 μV, a time constant of 1 ms, a 12 dB slope for the low-pass filter, and the lowest dynamic reserve.

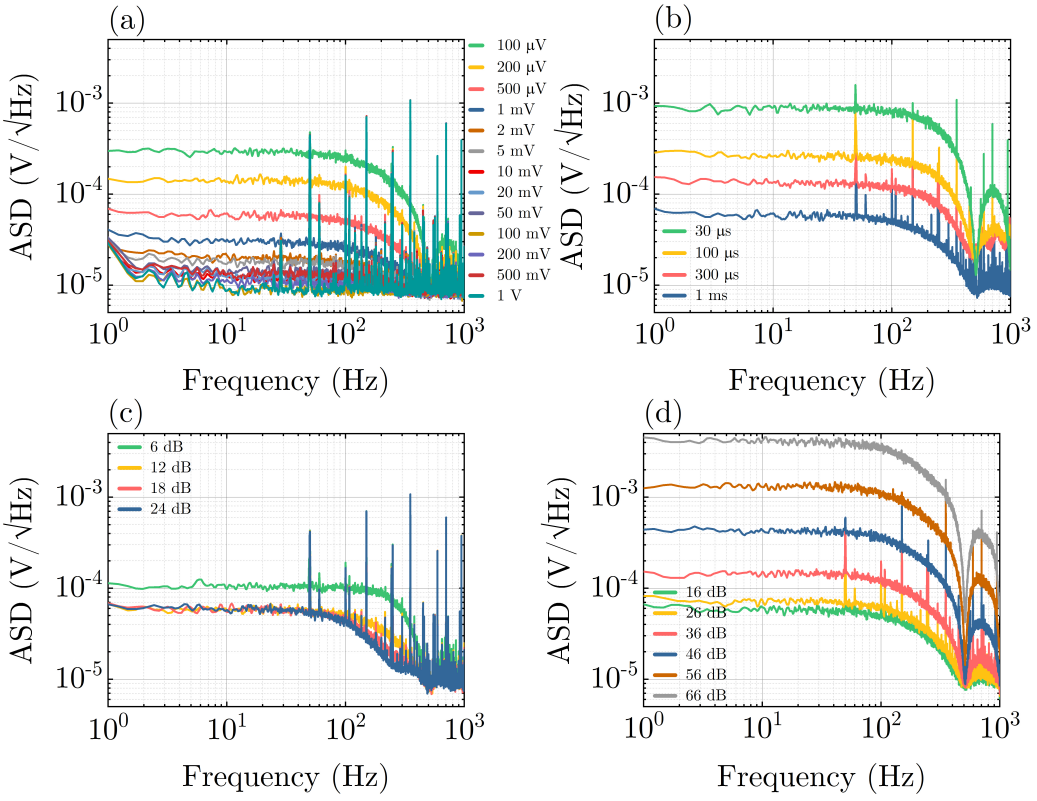

Figure 3.6: Characterizing the SR850 LIA. ASD for different LIA (a) gain settings, (b) time constants, (c) slopes of the low-pass filter, and (d) dynamic reserves.

Based on Fig. 3.6, we set the time constant at 1 ms, the slope of the low-pass filter at 12 dB, and the dynamic reserve at the minimum for all further measurements to achieve the lowest noise floor. The combination of the chosen time constant and the slope of the low-pass filter resulted in a 125 Hz bandwidth for our magnetometer using SR850. Furthermore, we attempted to enhance our ODMR signal to be able to use lower gain settings in our measurements and thus improve the sensitivity.

For a PSD technique, there are two other key parameters that are dependent on the physical system, the modulation frequency and the modulation depth. We discuss optimizing the modulation depth in Chapter 4 in detail [109]. Here, we investigate the modulation frequency by recording the ODMR signals and time traces for various modulation frequencies. The results are illustrated in Fig. 3.7 and show high noise densities for modulation frequencies lower than 20 kHz. Generally, higher modulation frequencies result in lower ASDs. In our experiments, the maximum modulation frequency was 50 kHz and was limited by the signal generator. However, high modulation frequencies require high detection bandwidth. As a result, we performed our experiments at a modulation frequency of 30 kHz, which we later increased to 35 kHz.

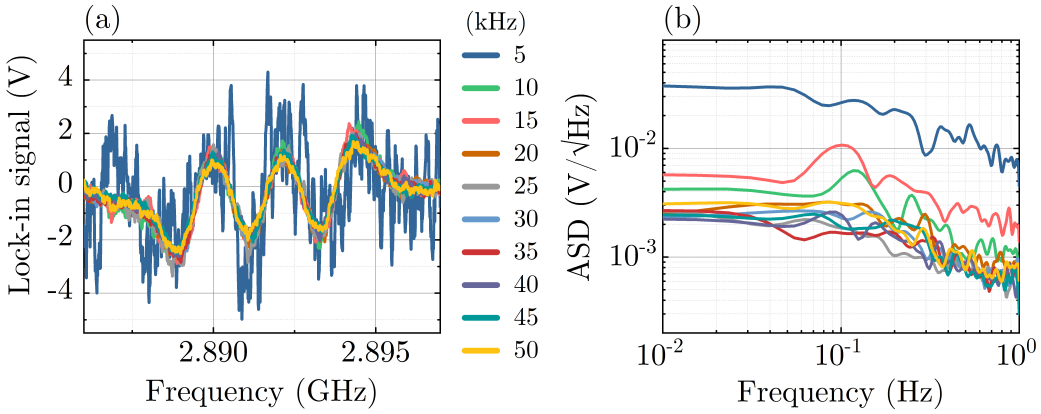

Figure 3.7: (a) ODMR measurements and (b) noise densities for different modulation frequencies. The noise density is higher for modulation frequencies below 20 kHz

Next, we isolated the signal around the modulation frequency before feeding it to the LIA. We constructed a Sallen Key second-order band-pass filter. The filter was centered at the same frequency as the modulation frequency of 35 kHz. The gain, phase response, and group delay of the filter are shown in Fig. 3.8 (a) as a function of frequency. The filter has a measured bandwidth of 15 kHz. Figure 3.8 (b) illustrates that using the band-pass filter enhances

the maximum slope the ODMR signal, which improves the sensitivity of the magnetometer.

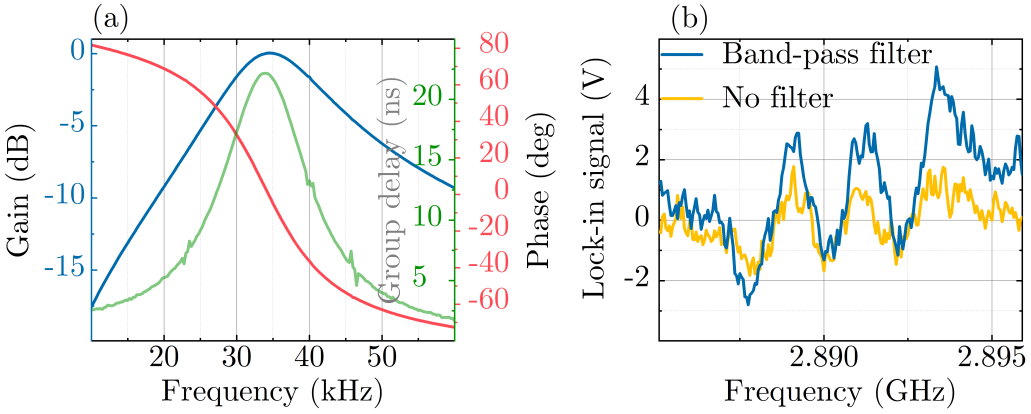

Figure 3.8: (a) Gain, phase response, and group delay of the band-pass filter centered at 35 kHz. (b) ODMR measurements with and without the band-pass filter, highlighting the enhancement of the LIA signal with band-pass filtering.

3.4 Electron spin resonance measurement

In this section, we combine the discussed methods for spin-state control and readout and the PSD technique to describe the general experimental setup. A schematic of the main part of the setup is shown in Fig. 3.9. We briefly review its components:
A CVD diamond with a low concentration of NV centers is placed at its Brewster angle $\theta \sim 67°$ in the center of the confocal optical cavity. The mirrors have reflectivies of R_1 and R_2. The incoupling mirror is attached to a piezo actuator to adjust the cavity length. The cavity is pumped with a p-polarized green laser. The phase of the pump field is modulated with an electro-optic modulator, which is not shown in the figure. The light transmitted through the cavity is detected and sent to the cavity lock. The cavity lock mixes this signal with the reference signal that modulates the phase of the pump light, low-pass filters the signal, and sends the signal to the piezo actuator as feedback for cavity stabilization.

The frequency-modulated carrier frequency f_c is mixed with f_m, corresponding to the coupling constant $A_\parallel = 2.16$ MHz of the hyperfine interaction between the electron spin of the NV centers and the ^{14}N intrinsic nuclear spin. The mixed signal is sent to the MW split-ring resonator. The fluorescence is collected from the large face of the diamond using either an objective

or a condenser lens and is filtered using a 600 nm cut-on long-pass filter (not shown in the figure). Some laser light is tapped off with a beam splitter before entering. The photocurrent of this signal is subtracted from the fluorescence signal to remove the technical noise of the laser. The subtracted signal is filtered with a band-pass filter centered at the modulation frequency and is fed to the LIA. The LIA demodulates the signal and its output, S_{LI}, is the three-frequency-modulated ODMR signal. Next, we discuss the idea of three-frequency excitation instead of single-frequency excitation and present certain results.

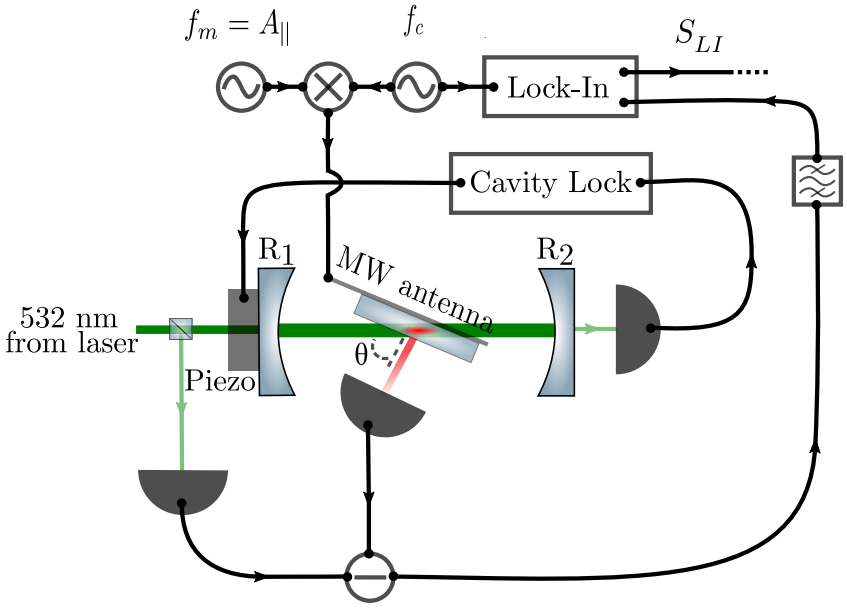

Figure 3.9: Schematic of the experimental setup for performing ODMR measurements. A phase-modulated 532 nm laser pumps the confocal optical cavity, which consists of two mirrors with reflectivities R_1 and R_2. The diamond containing NV centers is placed in the center of the cavity at its Brewster angle $\theta \sim 67°$. The transmission of light through the cavity is used to send feedback to the piezo and lock the cavity with the PDH technique. The signal driving the MW antenna is generated by mixing the frequency-modulated carrier signal f_c with $f_m = A_{\|}$, corresponding to the axial hyperfine constant of the NV centers. To remove the laser technical noise, the fluorescence emitted from the NV centers is detected and subtracted from the laser signal before entering the cavity. The subtracted signal is sent to the LIA and is demodulated using the reference signal that modulates the MW field.

3.4.1 Three-frequency excitation

Using the setup discussed in Fig. 3.9, various ODMR measurements were performed. Some examples of ODMR spectra are depicted in Fig. 3.10 to highlight the effects of modulation and excitation types. A permanent magnet was aligned along the [111] axis, which resulted in two stronger inner peaks generated from three orientations of the NV centers in the diamond and two outer peaks generated from a single orientation of the NV centers.

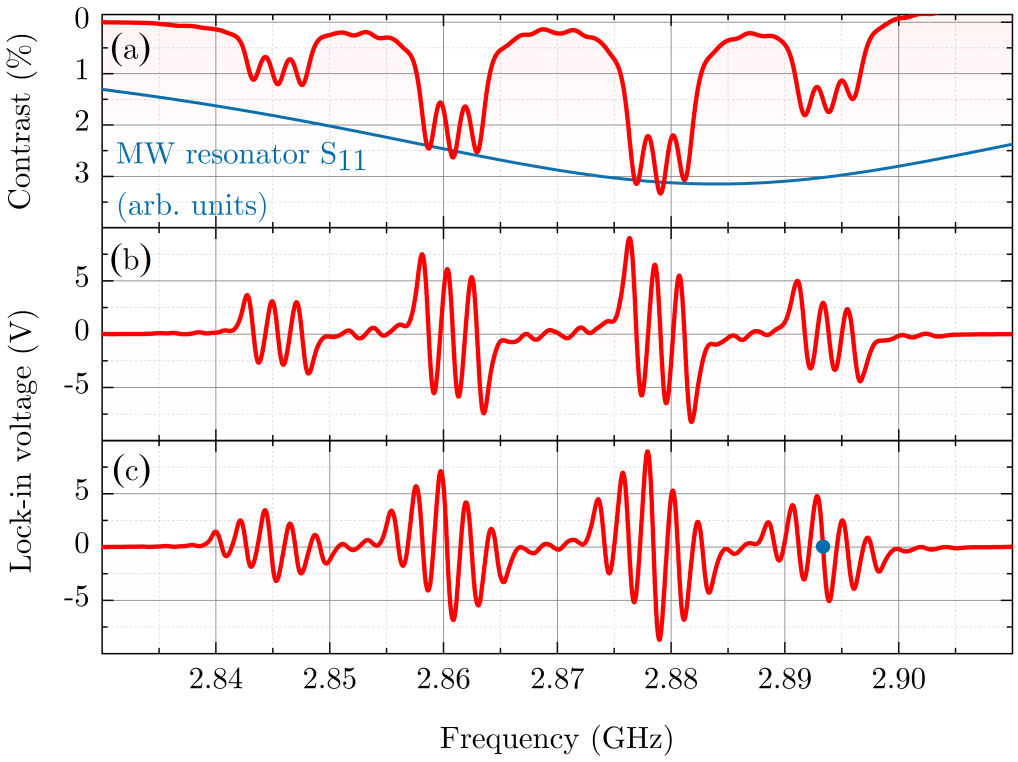

Figure 3.10: Plots of measured (a) amplitude-modulated single-frequency excitation, (b) frequency-modulated single-frequency excitation, and (c) three-frequency-modulated ODMR spectra. The blue trace in (a) displays the S_{11} parameter of the MW resonator (not sharing the y-axis with the red trace). The blue dot in (c) indicates the point that is most sensitive to changes in the magnetic field. Figure taken from Ref. [85].

The amplitude-modulated ODMR spectrum measured is presented in Fig. 3.10 (a), which is analogous to the unmodulated ODMR spectrum. The contrast of the two outer peaks (and the two inner peaks) is identical if they

experience the same MW field strength. We used a split-ring resonator that delivered a uniform MW field in a large area at the expense of being narrow-band. Therefore, the two outer peaks (and the two inner peaks) experienced different MW field strengths resulting in different contrasts. The blue trace in Fig. 3.10 (a) plots the frequency dependence of S_{11}.

A frequency-modulated ODMR spectrum is presented in Fig. 3.10 (b) that imitates the derivative of the amplitude-modulated ODMR spectrum. The sensitivity of the magnetometer is proportional to the slope of the electron spin resonance as $[\max(|\frac{d}{d_\omega}S|)]^{-1}$, where $\frac{d}{d_\omega}S$ is the derivative of the ODMR signal with respect to the MW frequency. The frequency-modulated spectrum has a higher $\max(|\frac{d}{d_\omega}S|)$ than the amplitude-modulated signal. Furthermore, simultaneously exciting all three hyperfine peaks by sweeping the MW drive with three frequencies of equal amplitude separated by $A_\parallel = 2.16$ MHz leads to a five-peak feature in the electron spin resonance possessing larger $\max(|\frac{d}{d_\omega}S|)$. The three-frequency-modulated ODMR spectrum is shown in Fig. 3.10 (c). The blue dot indicates the point of $\max(|\frac{d}{d_\omega}S|)$ for a single orientation of NV centers, which is thus the most sensitive point to changes in magnetic field. This point was used for the magnetometry measurements.

In addition, we measured a series of ODMR spectra as a function of MW power to determine the optimum MW power for obtaining highest $\max(|\frac{d}{d_\omega}S|)$. Figure 3.11 depicts similar measurements for single-frequency excitation and three-frequency excitation.

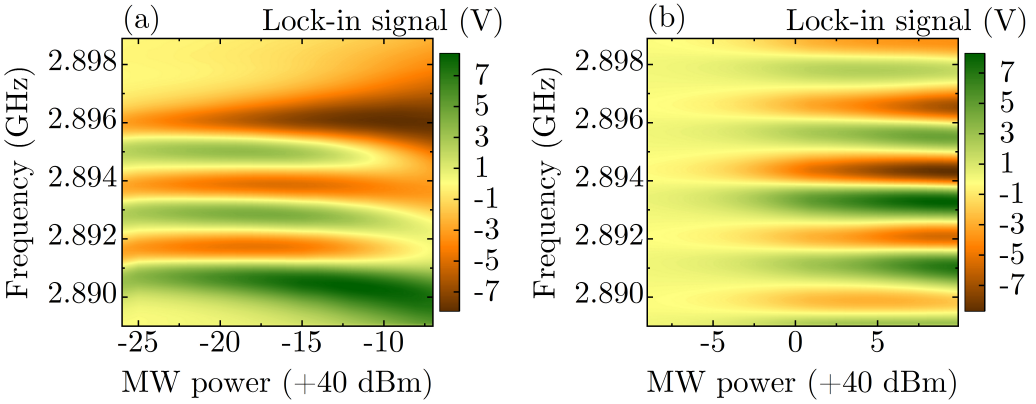

Figure 3.11: Measured frequency-modulated ODMR spectra as a function of MW power for (a) single-frequency excitation and (b) three-frequency excitation.

As shown in Fig. 3.9, for the case of three-frequency excitation, a mixer

was used to mix f_c with f_m. The mixer had losses, and as a consequence, the input MW power in Fig. 3.11 (b) is larger than the input MW power in (b).

3.4.2 Static and AC magnetic field inclusions

As supplementary measurements, we created an external magnetic field and measured it with our magnetometer. The static magnetic field was generated by applying a DC current to a coil. The coil was placed in the vicinity of the diamond. The magnetic field produced was detected with the magnetometer. The results were used to calibrate the magnetic field as shown in Fig. 3.12.

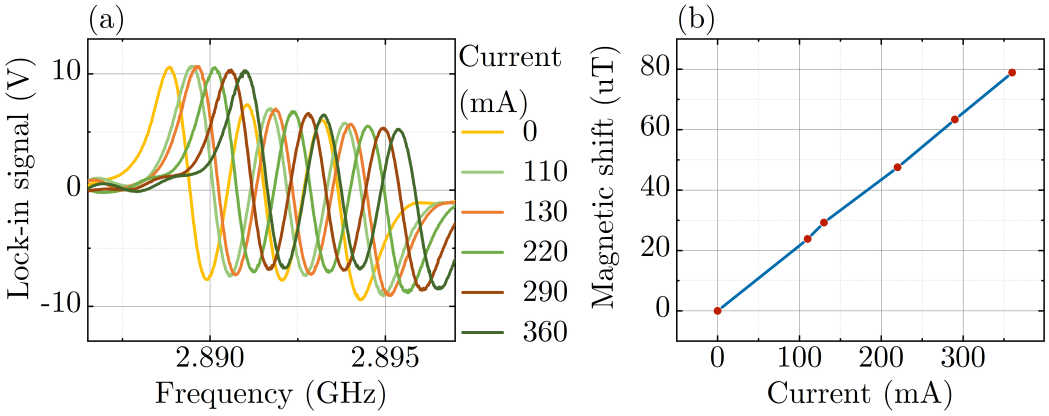

Figure 3.12: Calibrating the generated magnetic fields. (a) ODMR measurements for different currents in the coil that is placed in the vicinity of the diamond. (b) Measured magnetic shift as a function of current in the coil. The blue line connects the measured points.

Later, we applied an AC current through the coil and measured the response of the magnetometer. The calibration data was used to compare the estimated magnetic field with the measured magnetic field.

3.4.3 Analyzing data

The ASD was estimated using Welch's method [110] with 25 Blackman-Harris windows with 50% of the window length as the number of overlapped samples. The ASD was converted to sensitivity through:

$$\eta = \frac{\text{ASD}}{\max(|\frac{d}{d\omega}S|)\gamma_e}. \tag{3.15}$$

To plot the magnetic noise density, we measured three time traces for an optical cavity laser input of 400 mW: first, when the MW drive was adjusted to $\max(|\frac{d}{d_\omega}S|)$ of the frequency-modulated ODMR signal (magnetically sensitive), second, when the MW drive was far from any spin resonance (magnetically insensitive), and third, when the detector was blocked (electronic noise). Figure 3.13 depicts the Fourier transforms of the measured time traces, which are displayed in units of sensitivity using Eq. 3.15.

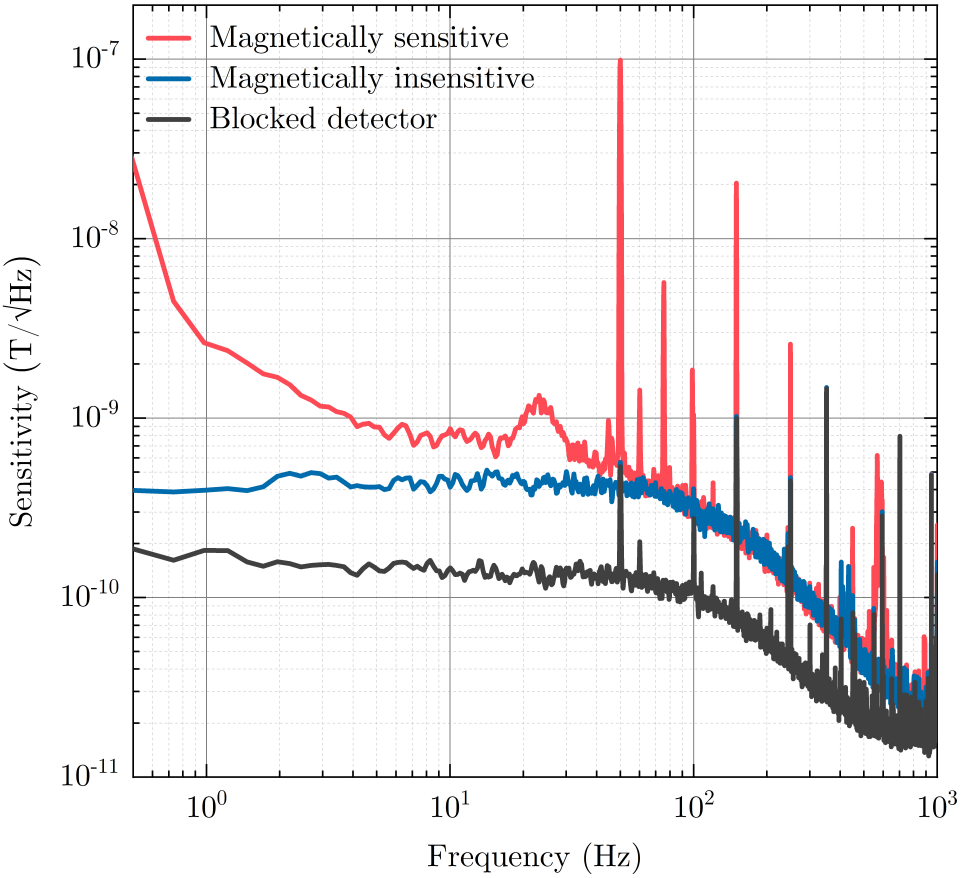

Figure 3.13: Measurements of magnetic noise spectral density: The magnetically sensitive configuration corresponds to the MW drive being set to $\max(|\frac{d}{d_\omega}S|)$ of the spin resonance (red trace), the magnetometer is magnetically insensitive when the MW drive is off-resonance (blue trace), and a blocked detector corresponds to the electronic noise of the system (black trace).

The red trace in Fig. 3.13 is magnetically sensitive and contains low frequency magnetic noise. In addition, the red trace shows a pronounced noise at 50 Hz and its harmonics. The magnetometer sensitivity of ~ 400 pT/$\sqrt{\text{Hz}}$ was deduced from the magnetically insensitive trace, which is shown by the blue trace. The black trace represents the electronic noise of the LIA and the photodetector. The results were obtained using a photodiode with a large sensitive area of 10 mm x 10 mm (Hamamatsu Photonics S3994-01) that collected ~ 110 μW fluorescence from the NV centers. Furthermore, the technical noise was suppressed by canceling out the correlated laser noise in the measured fluorescence. We obtain a bandwidth of 125 Hz followed by a 12 dB/octave roll-off that is generated by the low-pass filter of the LIA.

Next, we generated a 40 Hz sine-wave magnetic field and recorded the response of the magnetometer. The results are shown in Fig. 3.14.

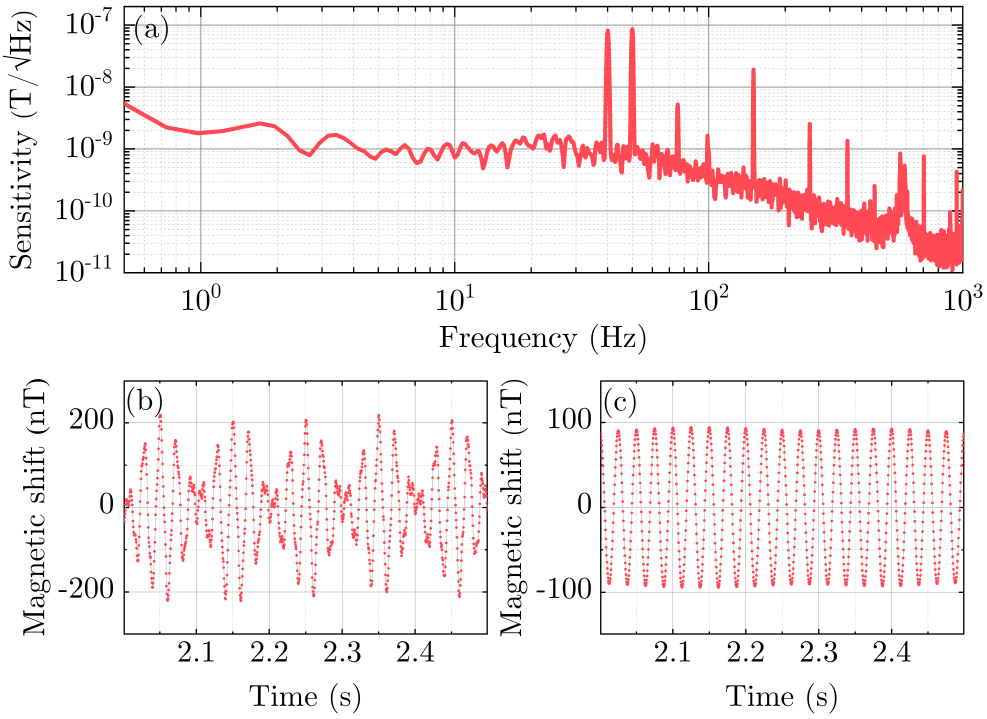

Figure 3.14: Plots of the magnetometer response to a 40 Hz applied sine-wave magnetic field. (a) Measurement of the magnetic noise density. The applied 40 Hz magnetic field and the 50 Hz magnetic noise from the environment are visible. (b) The response of the magnetometer to the applied magnetic field, highlighting the beating of 40 Hz and 50 Hz magnetic fields. (c) The same response as (b), band-pass filtered from 35 kHz to 45 kHz.

The Fourier transform of the time trace is presented in Fig 3.14 (a) in units of sensitivity. The pronounced 40 Hz and 50 Hz peaks are signatures of the applied magnetic field and the magnetic noise in the environment, respectively. The beating of these signals is visible in the measured time trace, as shown in Fig 3.14 (b). Digitally band-pass filtering the time trace from 35 kHz to 45 kHz removed both the low frequency and the 50 Hz magnetic noise, and the response to the 40 Hz applied magnetic field remained, as shown in Fig 3.14 (c).

3.4.4 Pulsed measurements

In addition to the sensitivity measurements, we performed pulsed measurements while keeping the optical cavity locked. Figure 3.15(a) shows an example of Rabi oscillations as a function of MW frequency for a single orientation of NV centers in the diamond. Three hyperfine states can be distinguished at longer MW pulse lengths. We measured the Rabi frequencies for several different MW powers. The result is presented in Fig. 3.15(b). The curve was fitted to estimate the Rabi frequencies for lower MW powers. Changing the MW antenna or the diamond thickness required the measurements to be repeated.

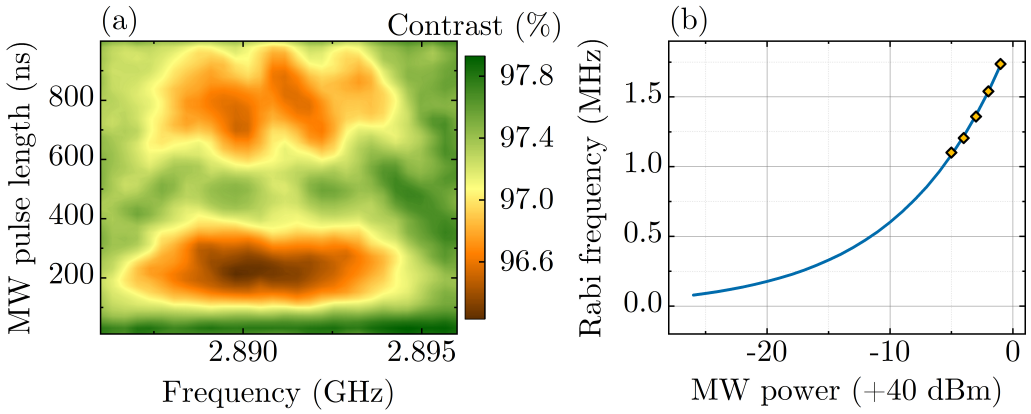

Figure 3.15: (a) Measured Rabi oscillations as a function of MW frequency. (b) Fitted curve of Rabi frequency as a function of MW power. The yellow dots are the experimental measurements.

Another pulsed measurement, the Ramsey sequence, was performed with the locked optical cavity. The free induction decay as a function of MW frequency, as shown in Fig. 3.16 for two different MW powers. Hyperfine states are visible, especially for lower MW power. We attempted to measure the relaxation time and perform a Hahn-echo sequence to measure the

decoherence time while the optical cavity was locked. However, there were difficulties in keeping the cavity locked and finalizing the sequence due to long pulses with the laser off.

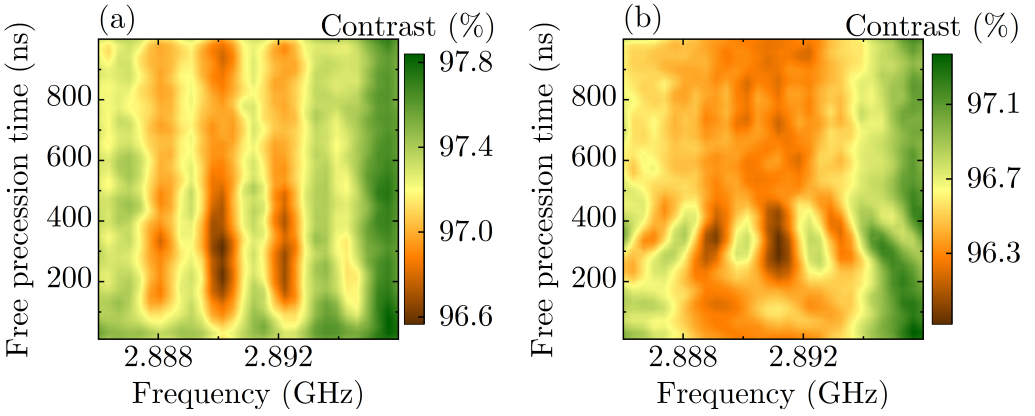

Figure 3.16: Measured free induction decay as a function of MW frequency when applying MW powers of (a) -6 dBm and (b) -1 dBm.

In the following chapters, we present our results using the experimental framework that was discussed in this chapter.

Chapter 4

Optimized Frequency Modulation

4.1 Introduction

PSD is a powerful tool in experimental physics that enables the extraction of signals buried in noise. This type of detection requires the measurements to be modulated with a certain function, frequency, and depth. In this chapter, we explore the ideal modulation conditions for sensing applications. We study the experimental results regarding the NV centers in diamond.

4.2 Publication

This section was published in Optics Express with the title of "Optimised frequency modulation for continuous-wave optical magnetic resonance sensing using nitrogen-vacancy ensembles" as follows:

Research Article | Vol. 25, No. 13 | 26 June 2017 | OPTICS EXPRESS 14809
Optics EXPRESS

Optimised frequency modulation for continuous-wave optical magnetic resonance sensing using nitrogen-vacancy ensembles

HAITHAM A. R. EL-ELLA,[1,*] SEPEHR AHMADI,[1] ADAM M. WOJCIECHOWSKI,[1,2] ALEXANDER HUCK,[1] AND ULRIK L. ANDERSEN[1]

[1]*Department of Physics, Technical University of Denmark, Kongens Lyngby, Denmark*
[2]*On leave from the Jagiellonian University, Kraków, Poland*
[*]*haitham.el@fysik.dtu.dk*

Abstract: Magnetometers based on ensembles of nitrogen-vacancy centres are a promising platform for continuously sensing static and low-frequency magnetic fields. Their combination with phase-sensitive (lock-in) detection creates a highly versatile sensor with a sensitivity that is proportional to the derivative of the optical magnetic resonance lock-in spectrum, which is in turn dependant on the lock-in modulation parameters. Here we study the dependence of the lock-in spectral slope on the modulation of the spin-driving microwave field. Given the presence of the intrinsic nitrogen hyperfine spin transitions, we experimentally show that when the ratio between the hyperfine linewidth and their separation is $\gtrsim 1/4$, square-wave based frequency modulation generates the steepest slope at modulation depths exceeding the separation of the hyperfine lines, compared to sine-wave based modulation. We formulate a model for calculating lock-in spectra which shows excellent agreement with our experiments, and which shows that an optimum slope is achieved when the linewidth/separation ratio is $\lesssim 1/4$ and the modulation depth is less then the resonance linewidth, irrespective of the modulation function used.

OCIS codes: (300.6380) Spectroscopy, modulation; (160.2220) Defect-center materials; (260.7490) Zeeman effect; (020.2930) Hyperfine structure

References and links

1. W. E. Bell and A. L. Bloom, "Optical detection of magnetic resonance in alkali metal vapour," Phys. Rev. **107**, 1559–1565 (1957).
2. S. Kotler, N. Akerman, Y. Glickman, A. Keselman, and R. Ozeri, "Single-ion quantum lock-in amplifier," Nature **473**, 61–65 (2011).
3. S. M. Salapaka and M. V. Salapaka, "Scanning probe microscopy," IEEE Control Syst. Mag. **28**, 65–83 (2008)
4. A. Al Mohtar, J. Vaillant, Z. Sedaghat, M. Kazan, L. Joly, C. Stoeffler, J. Cousin, A. Khoury, and A. Bruyant, "Generalised lock-in detection for interferometry: application to phase sensitive spectroscopy and near-field nanoscopy," Opt. Express **22**, 22232–22245 (2014)
5. R. H. Dicke, "The measurement of thermal radiation at microwave frequencies," Rev. Sci. Instrum. **17**, 268–275 (1946).
6. I. Mateos, B. Patton, E. Zhivun, D. Budker, D. Wurm, and J. Ramos-Castro, "Noise characterization of an atomic magnetometer at sub-millihertz frequencies," Sensor Actuat. A-Phys. **224**, 147–155 (2015).
7. H. Clevenson, M. E. Trusheim, T. Schroder, C. Teale, D. Braje, and D. Englund, "Broadband magnetometry and temperature sensing with a light trapping diamond waveguide," Nat. Phys. **11**, 393–397 (2015).
8. D. Robbes, "High sensitive magnetometers-a review," Sensor Actuat. A-Phys. **129**, 86–93 (2006).
9. D. Sheng, S. Li, N. Dural, and M. V. Romalis, "Subfemtotesla scalar atomic magnetometry using multipass cells," Phys. Rev. Lett. **110**, 160802 (2013).
10. I. K. Kominis, T. W. Kornak, J. C. Allred, and M. V. Romalis, "A subfemtotesla multichannel atomic magnetometer," Nature **442**, 596–599 (2003).
11. L. Rondin, J.-P. Tetienne, T. Hingant, J.-F. Roch, P. Maletinsky, and V. Jacques, "Magnetometry with nitrogen-vacancy defects in diamond," Rep. Prog. Phys. **77**, 056503 (2014).
12. R. Schirhagl, K. Chang, M. Loretz, and C. L. Degen, "Nitrogen-vacancy centres in diamond: nanoscale sensors for physics and biology," Annu. Rev. Phys. Chem. **65**, 83–105 (2014).
13. J. M. Taylor, P. Cappellaro, L. Childress, L. Jiang, D. Budker, P. R. Hemer, A Yacoby, R. Walsworth, and M. D. Lukin, "High-sensitivity diamond magnetometer with nanoscale resolution," Nat. Phys. **4**, 810–816 (2008).

#292431 http://dx.doi.org/10.1364/OE.25.014809
Journal © 2017 Received 7 Apr 2017; revised 26 May 2017; accepted 28 May 2017; published 19 Jun 2017
Corrected: 7 July 2017

Optics EXPRESS

14. T. Wolf, P. Neumann, K. Nakamura, H. Sumiya, T. Ohshima, J. Isoya, and J. Wrachtrup, "Subpicotesla diamond magnetometry," Phys. Rev. X **5**, 041001 (2015).
15. N.M. Nusran and M. V. Gurudev Dutt, "Dual-channel lock-in magnetometer with a single spin diamond," Phys. Rev. B **88**, 220410 (2013).
16. R. S. Schoenfeld and W. Harneit, "Real time magnetic field sensing and imaging using a single spin in diamond," Phys. Rev. Lett. **106**, 030802 (2011).
17. I. V. Fedotov, L. V. Doronina-Amitonoa, A. A. Voronin, A. O. Levchenko, S. A. Zibrov, D. A. Sidorov-Biryukov, A. B. Fedotov, V. L. Velichansky and A.M. Zheltikov, "Electron spin manipulation and readout through an optical fibre," Sci. Rep. **4**, 5362 (2014).
18. K. Jensen, N. Leefer, A. Jarmola, Y. Dumiege, V. M. Acosta, P. Kehayias, B. Patton, and D. Budker, "Cavity-enhanced room-temperature magnetometry using absorption by nitrogen-vacancy centres in diamond," Phys. Rev. Lett. **112**, 160802 (2014).
19. A. Wickenbrock, H. Zheng, L. Bougas, N. Leefer, S. Afach, A. Jarmola, V. M. Acosta, and D. Budker, "Microwave-free magnetometry with nitrogen-vacancy centres in diamond," Appl. Phys. Lett. **109**, 053505 (2016).
20. J. F. Barry, M. J. Turner, J. M. Schloss, D. R. Glenn, Y. Song, M. D. Lukin, H. Park, and R. L. Walsworth, "Optical magnetic detection of single-neuron action potentials using quantum defects in diamond," Proc. Natl. Acad. Sci. USA **113**, 14133–14138 (2016).
21. M. W. Doherty, N. B. Manson, P. Delaney, F. Jelezko, J. Wrachtrup and L. C. L. Hollenberg, "The nitrogen-vacancy color centre in diamond," Phys. Rep. **528**(1), 1–45 (2013).
22. V. M. Acosta, E. Bauch, M. P. Ledbetter, C. Santori, K.-M. C. Fu, P. E. Barclay, R. G. Beausoleil, H. Linget, J. F. Roch, F. Treussart, S. Chemerisov, W. Gawlik, and D. Budker, "Diamonds with a high density of nitrogen-vacancy centres for magnetometry applications," Phys. Rev. B **80**, 115202 (2009).
23. N. Alsam, G. Waldherr, P. Neumann, F. Jelezko, and J. Wrachtrup, "Photo-induced ionization dynamics of the nitrogen vacancy defect in diamond investigated by single-shot charge state detection," New Journal of Physics **15**, 013064 (2013).
24. L. Robledo, H. Bernien, T. V. D. Sar, and R. Hanson, "Spin dynamics in the optical cycle of single nitrogen-vacancy centres in diamond," New Journal of Physics **13**, 025013 (2011).
25. J. R. Carson, "Notes on the theory of modulation," Proceedings of the Institute of Radio Engineers **10**, 57–64 (1922).
26. A. Dréau, M. lesik, L. Rondin, P. Spinicelli, O. Arcizet, J.-F- Roch, and V. Jacques, "Avoiding power broadening in optically detected magnetic resonance of single NV defects for enhanced dc magnetic field sensitivity," Phys. Rev. B **84**, 195204 (2011).
27. K. Jensen, V. M. Acosta, A. Jarmola, and D. Budker, "Light narrowing of magnetic resonances in ensembles of nitrogen-vacancy centres in diamond," Phys. Rev. B **87**, 014115 (2013).

1. Introduction

One of the primary tools for precision measurements in modern experimental physics is phase-sensitive detection. As its principle is straightforward - retrieving a modulated signal component obscured in noise by mixing the total signal with a similarly modulated reference - this detection method results in a versatility that is applicable and implementable in a range of scenarios, from atomic magnetometers [1], to single-ion lock-in detection [2], scanning probe microscopy [3], and optical interferometry and spectroscopy [4]. Phase-sensitive detection is often carried out in conjunction with frequency filtration and AC-amplification, which is collectively termed as lock-in detection [5]. For sensing devices, this procedure is usually applied to overcome the problem of increased susceptibility to low-frequency or discrete frequency noise components when attempting to enhance the sensitivity. The main challenge usually lies in identifying suitable system parameters for modulation which lends itself to both maximising the systems response and discriminating it from noise lying outside a given bandwidth. This is pertinent in, for example, low-frequency magnetometry (DC to $\lesssim 1$ kHz) where $1/f$ noise and slow drifts stemming from the environment start to dominate [6, 7].

High sensitivity magnetometry has been mainly spurred on by advances in superconductivity and atomic magneto-optics [8], where $<\mathrm{fT}/\sqrt{\mathrm{Hz}}$ sensitivities have been achieved for a ~ 0.3 cm^3 sampling volume in both pulsed and continuous-wave operating regimes [9, 10]. However, there has been a recent surge of interest in exploring diamond-based magnetometery using ensembles of nitrogen-vacancy (NV) defects, due to the relatively simple technical operation under ambient conditions, their small potential sampling volume (approaching $\mu\mathrm{m}^3$ volumes), and their chemical inertness which allows for direct physical contact with delicate biological

Optics EXPRESS

systems [11, 12]. NV magnetic sensing schemes are usually based on either continuous-wave optically detected magnetic resonance (*cw*-ODMR) or pulsed ODMR, both which are used to determine small magnetic field changes $\delta\mathbf{B}$ around a fixed $\mathbf{B}$ field offset. *Cw*-ODMR schemes possess field sensitivities limited by the ratio of the spin resonance linewidth to fluorescence contrast and shot-noise level. On the other hand, pulsed techniques such as Ramsey/π-pulsed schemes result in sensitivities limited by $1/T_2*$, while spin-echo-based pulsed schemes possess enhanced field-sensitivities at the expense of limiting their optimised sensitivity to magnetic fields oscillating at frequencies in the order of $1/T_2$ [13].

When sensing low frequency fields (< 1 kHz) or spatial field variations over macroscopic areas, the use of *cw*-ODMR schemes is more technically convenient, which avoids the difficulty facing pulsed schemes in ensuring sufficient uniform intensity and spin control over a macroscopic volume, and involves simply monitoring the spin resonance frequency through shifts in the detected fluorescence level. The efficiency of this scheme is based on how large a change in fluorescence can be generated and how small a change can be detected, for incremental resonance shifts induced by an external magnetic field. The challenge is thus generating the narrowest spectral linewidth during *cw*-driving while ensuring that the fluorescence contrast is as high as possible. This is primarily limited by the number of spins used and the amount of light that is generated and collected, as well as the inherent collective-spin dephasing rates, the optical and microwave (MW) power-related dephasing, the environmental noise fluctuations, and the technical noise in both the detection apparatus and that introduced by power fluctuations occurring at various frequencies in the drive and measurement fields [14]. The use of lock-in detection is therefore well suited to overcome many of these issues in order to ensure the intrinsic-sensitivity of the NV system is maintained.

Previous NV-related work which addresses the use of lock-in detection has focused on single NV based sensing through multi-pulsed phase estimation schemes [15], or their incorporation within a scanning-probe based schemes [16]. Alternatively, it has also been presented as an integral component for NV ensemble magnetometery using optical fibre-based read-out [17], using the diamond as a light trapping-waveguide [7], through the absorption of the spin-singlet state [18], when avoiding the use of a MW drive field [19], or for sensing biologically generated magnetic fields [20]. However, to our knowledge, there has been no published investigation of the technicalities on optimising the modulation parameters to maximise the slopes in the measured lock-in spectrum. While this technique is conceptually undemanding, the optimum modulation function for NV ensemble magnetometry is not obvious as it is dependent on the systems spin resonance spectrum and its unique response to optical and microwave drive fields. This is especially true as NV systems possesses two/three (depending on the nitrogen isotope) peaks centred around the electron spin resonance frequency, due to the intrinsic hyperfine coupling between the nitrogen nuclear spin and the electron spin, which all respond identically to an external field.

The work presented in this article therefore investigates NV ensemble-specific ODMR spectra with particular emphasis on delineating an optimum modulation function of the microwave field drive for *cw*-ODMR sensing. This is carried out by first describing the characteristic NV *cw*-ODMR spectrum, followed by a description of frequency modulated lock-in detection. Finally, experimental and theoretical results are compared and discussed, which show that the optimum modulation function and depth are dependent on the linewidth-to-separation ratio of the measured peaks.

2. Optically detected magnetic resonance

2.1. Continuous-wave spectrum

All *cw*-ODMR measurements presented in this article are carried out using an ensemble of native $^{14}NV^-$ in an untreated single-crystal diamond (Element 6) grown using chemical vapour

Optics EXPRESS

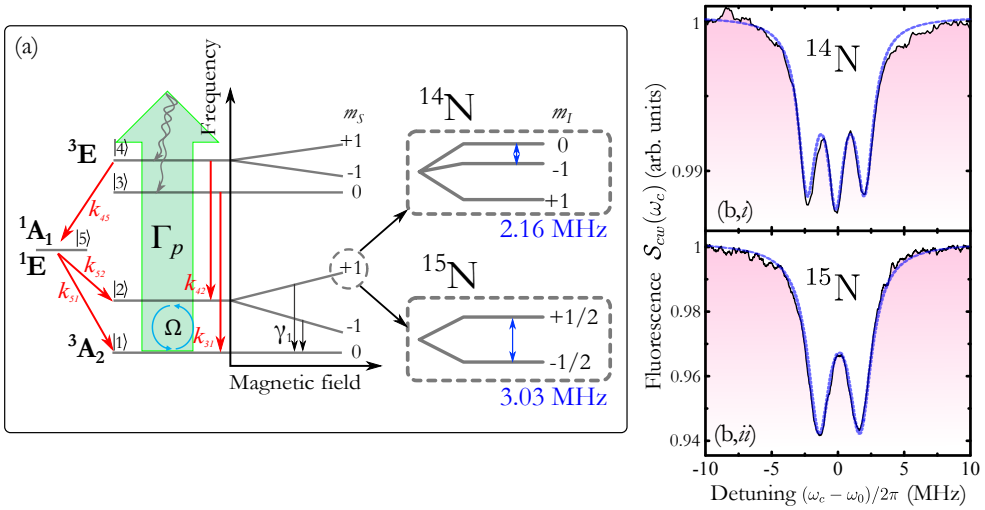

Fig. 1. (a) A general level schematic of the NV system, used to set up the optical Bloch equations. The electronic structure is comprised of a triplet state ($^3\mathbf{A}_2 \leftrightarrow {}^3\mathbf{E}$) and a singlet shelving state ($^1\mathbf{E} \leftrightarrow {}^1\mathbf{A}_1$). The $^3\mathbf{A}_2$ state levels can be coherently driven with the application of a MW drive with a Rabi frequency Ω, while above band excitation is carried out with a rate Γ_p, with the optical excitation processes being almost perfectly spin conserving. The spin levels are split with the introduction of a magnetic field, and couple with the nuclear spin of the N atom, generating an additional two or three hyperfine levels depending on the N isotope. These hyperfine levels are evident in *cw*-ODMR as shown in the measured spectra (b,i,ii) from an NV ensemble, where a weak magnetic field ($\sim$ 5 mT) has been applied to spectrally separate the distinct crystallographic sub-groups. The dotted blue lines are fits using equation (4) with the parameters $\Gamma_p/2\pi \simeq 20$ kHz, $\Omega/2\pi \simeq 30$ kHz, and $\gamma_2^*/2\pi \simeq 700$ kHz for ^{14}N, and $\Gamma_p/2\pi \simeq 50$ kHz, $\Omega/2\pi \simeq 100$ kHz, and $\gamma_2^*/2\pi \simeq 1$ MHz for ^{15}N.

deposition (with the exception of the spectrum shown in Fig. 1(b,ii), which was measured from a custom-grown diamond with an isotopically purified nitrogen source to produce an ensemble of ^{15}NV$^-$). The NV centre is a coupled pair of defects within a diamond carbon lattice, consisting of a substitutional nitrogen atom and a point vacancy. The defect pair exists in both a negatively charged and neutral configuration, as well as in two different isotopic forms of ^{14}N and ^{15}N. While both the neutral and charged state fluoresce, it is the negatively charged state which possesses a spin triplet configuration because of its extra electron, resulting in a magnetic-dipole transition with magnetically tunable spin levels [21]. The energy levels of the most relevant transitions are shown in Fig. 1(a). Coupled with a near-perfect spin-conserving optical dipole of the NV centre, an optical-contrast spectrum ($\mathcal{S}_{cw}(\omega_c)$, Fig. 1(b)) of the spin resonances can be generated by simultaneously shining light and sweeping the frequency of an applied microwave (MW) field across the spin Larmor frequency. This presents itself as magnetically sensitive probe, which changes its resonance frequency, and therefore its fluorescence rate, as a function of $\gamma_e B_z$, where $\gamma_e \sim 28$ MHz/mT is the electron gyromagnetic ratio, and B_z is a magnetic field vector component projected along the crystallographic axis of the NV defect.

The use of a single or ensemble of spins has direct implications on the apparatus used, and the overall sensitivity. For single NV spins, the amount of light generated is within the $\sim$ 0.05 pW range, which falls within the working limits of single photon counting avalanche photodiodes (APD). These usually give excellent signal-to-noise ratios due to their low intrinsic noise levels, and do not require additional lock-in detection provided that the noise in the driving fields or

Optics EXPRESS

environment do not exceed the shot-noise level. Single spins have a sensitivity ultimately limited to $\sim$ nT/$\sqrt{\text{Hz}}$, when using pulsed sensing protocols (for continuous wave protocols it is in the order of $\sim$ 100 nT/$\sqrt{\text{Hz}}$), and provide nano-scale sensor resolution. If such spatial resolution is not required using an ensemble of spins boosts the sensitivity by $1/\sqrt{N}$, where N is the number of spins used [13]. However, dense ensembles ($>$ 1 ppm NV) prepared through conventional irradiation and annealing techniques usually display a degraded collective ODMR linewidth due to inhomogeneous broadening and the increased susceptibility to static and driving field inhomogeneities [22]. Furthermore, the generated light from an ensemble is usually beyond the working limits of conventional APDs, and the use of *pin*-type photodiodes is necessary which are inherently noisier then APDs. For dense ensembles, fluorescence rates in the mW range can be obtained which usually allows for a shot-noise limited noise floor to be reached, however the degraded linewidth and the introduction of inhomogeneity-related degradation for higher density ensembles [22] implies that there may be an optimum balance between NV density and resulting sensitivity. In the low-density case ($\ll$ 1 ppm NV), an enhanced fluorescence rate can be achieved without too much degradation of the collective coherence/linewidth. However, the inherent *cw*-ODMR contrast for an ensemble of NVs of a single crystallographic orientation is usually around 1-3% [11], so the working signal-to-noise ratio needs to exceed this limit. Lock-in detection is therefore ideal for tackling these latter issues, usually allowing for a shot-noise limited spectrum to be achieved when optimally driving a low-density ensemble, while maintaining a linewidth that closely resemble those obtained from single NV defects.

By continuously applying a MW drive on the steepest part of $\mathcal{S}_{cw}(\omega_c)$, and monitoring the level of fluorescence, the presence, frequency and relative amplitude of a magnetic field can be deduced. The absolute sensitivity δB of such a detection process is proportional to $[d_\omega \mathcal{S}_{cw} \gamma_e]^{-1}$, where $d_\omega \mathcal{S}_{cw}$ is the derivative of $\mathcal{S}_{cw}(\omega_c)$ at a particular drive frequency $\omega_c/2\pi$ [7]. The relevant electronic levels that bring about the characteristic $\mathcal{S}_{cw}(\omega_c)$ spectrum are summarised in Fig. 1(a). The system ground state spins are driven by a coherent MW field with a drive frequency $\omega_c/2\pi$ and a Rabi frequency $\Omega/2\pi$, together with an above-band excitation rate $\Gamma_p/2\pi$, in this case considered for a 532 nm wavelength laser. This wavelength ensures that the $\text{NV}^- \rightleftharpoons \text{NV}^0$ charge state fluctuation rate is small in comparison to the NV^- fluorescence rate [23]. There is an intrinsic hyperfine interaction between the nitrogen nuclear spin and the electron spin of the NV centre which results in two or three hyperfine resonances depending on the nitrogen isotope, as summarised in Fig. 1. The resulting $\mathcal{S}(\omega_c)$ spectra are shown in Fig. 1(b), with the spectra of the sample used throughout the remaining article shown in Fig. 1(b,i).

A schematic of the experimental setup is shown in Fig. 2(a). A signal generator (Stanford Research Systems SG394) is used to deliver a modulated drive frequency $\omega_c/2\pi$ to an antenna placed close to the diamond sample. The diamond is excited with a 532 nm laser (Verdi SLM Coherent), and the fluorescence is collected using a condenser lens, filtered using a long-pass filter with a 600 nm cut-on, and detected using a biased Si detector (Thorlabs DET36A, with a 10 kΩ load, resulting in a bandwidth of 400 kHz). The excitation volume is in the order of 10^{-2} mm^3 with an estimated number of 10^9 NVs. The measured full-width at half-maximum of an individual hyperfine transition is $\gamma/2\pi \sim 1$ MHz, which was well fitted with a linear combination of a Lorentzian and a Gaussian profile (a pseudo-Voigt function) which is ~98% Lorentzian and ~2% Gaussian. This indicates that the in-homogeneous broadening is negligible, and the spectra can be confidently analysed using Lorentzian functions. The detector sends the signal to a two-channel digital lock-in amplifier (Stanford Research Systems SR850), while the MW drive frequency $\omega_c/2\pi$ is modulated at $\nu = 30$ kHz, for which this frequency was confirmed to be in a flat part of the optical power spectrum, and well within the detectors bandwidth. While the lock-in detector has a bandwidth up to 100 kHz, no further gain was achieved in the signal to noise ratio when modulating beyond 30 kHz, beyond which also a reduction in the lock-in signal amplitude is observed due to the limitations of the NV ensemble re-polarisation rate (set

Optics EXPRESS

by the excitation rates used). Simultaneous excitation of all three hyperfine transitions of $^{14}NV^-$ is carried out by mixing the modulated MW with a frequency equivalent to the axial hyperfine constant of $^{14}NV^-$, which is $A_{\|} = 2.16$ MHz.

The $\mathcal{S}_{cw}(\omega_c)$ spectrum of an NV ensemble can be simulated using a set of optical Bloch equations, by considering a single spin transition (e.g. $|m_s = 0\rangle \leftrightarrow |+1\rangle$) in a total of five levels as shown in Fig. 1(a), with the Hamiltonian:

$$\hat{\mathcal{H}}/\hbar = \sum_{i}^{5} \omega_i |i\rangle\langle i| - \Omega \cos(\omega_c t)(|1\rangle\langle 2| + |2\rangle\langle 1|). \tag{1}$$

Only the dominant decay paths considered are highlighted in red in Fig. 1(a), and only the ground-state level transition ($|1\rangle \leftrightarrow |2\rangle$) is described in terms of a coherent resonant drive. In a rotating reference frame with ω_c and using the rotating-wave approximation, the optical Bloch equations are:

$$\begin{aligned}
\dot{\rho}_{11} &= -\Gamma_p\rho_{11} + k_{31}\rho_{33} + k_{41}\rho_{44} + k_{51}\rho_{55} \\
&\quad -\frac{k_{21}}{2}(\rho_{11} - \rho_{22}) - \frac{i}{2}\Omega(\rho_{12} - \rho_{21}), \\
\dot{\rho}_{22} &= -\Gamma_p\rho_{22} + k_{32}\rho_{33} + k_{42}\rho_{44} + k_{52}\rho_{55} \\
&\quad -\frac{k_{21}}{2}(\rho_{22} - \rho_{11}) + \frac{i}{2}\Omega(\rho_{12} - \rho_{21}), \\
\dot{\rho}_{33} &= \Gamma_p\rho_{11} - (k_{35} + k_{32} + k_{31})\rho_{33}, \\
\dot{\rho}_{44} &= \Gamma_p\rho_{22} - (k_{45} + k_{42} + k_{41})\rho_{44}, \\
\dot{\rho}_{55} &= k_{45}\rho_{44} + k_{35}\rho_{33} - (k_{52} + k_{51})\rho_{55}, \\
\dot{\rho}_{12} &= -(\gamma_2' - i\delta)\rho_{12} + \frac{i}{2}\Omega(\rho_{22} - \rho_{11}), \\
\dot{\rho}_{21} &= -(\gamma_2' + i\delta)\rho_{21} - \frac{i}{2}\Omega(\rho_{22} - \rho_{11}),
\end{aligned} \tag{2}$$

where $\delta = (\omega_c - \omega_0)$ is the detuning between ω_c and the spin transition frequency ω_0 and ρ_{ii} is the normalised population of a level, while the total dephasing rate is defined as a sum of the longitudinal spin relaxation rate k_{21}, pure dephasing rate γ_2^*, and the optical pump rate through $\gamma_2' = k_{21}/2 + \gamma_2^* + \Gamma_p/2$. A unit-less, detuning-dependant *cw*-ODMR fluorescence ratio can then be described in terms of the steady-state populations of the excited states $|3\rangle$ and $|4\rangle$:

$$\mathcal{I}_{cw} = \frac{(k_{31}+k_{32})\rho_{33}^{ss}}{k_{31}+k_{32}+k_{35}} + \frac{(k_{41}+k_{42})\rho_{44}^{ss}}{k_{41}+k_{42}+k_{45}}. \tag{3}$$

The exact steady-state solution for equation (3) is given in Appendix A, while the rates used have been extracted from [24]. The *cw*-ODMR spectrum including the hyperfine lines is a sum of three individual peaks spaced by the axial hyperfine constant $A_{\|}$ which is 2.16 MHz for ^{14}N and 3.03 MHz for ^{15}N [21]:

$$\mathcal{S}_{cw}(\omega_c) = R_0 \sum_{m_I} \mathcal{I}_{cw}(\delta + m_I 2\pi A_{\|}), \tag{4}$$

where R_0 is the off-resonance detection rate, and m_I is the nuclear quantum number which spans either $\{-1, 0, 1\}$ for ^{14}N or $\{-\frac{1}{2}, \frac{1}{2}\}$ for ^{15}N. Equation (4) sufficiently reproduces experimentally observed *cw*-ODMR spectra, in particular as it accounts for power-related broadening and the dependence of the linewidth/contrast ratio to the spin excitation and polarisation rates. It is used as a basis for all simulations presented in this article, where the simulated fluorescence contrast and linewidth are an outcome of the given excitation rates, rather than postulated values. Through our measurements, we observe that using this model with rates measured from a single NV [24] can successfully represent a low density NV ensemble, and routinely obtains excellent agreement between the generated and measured spectra, as shown in Fig. 1(b,i,ii).

Optics EXPRESS

2.2. Lock-in spectrum

Generally, an ideally modulated signal can be decomposed as a sum of a static and time-varying component which is a product of a time-independent amplitude and an oscillatory function (i.e. $V(t) = V_0 + A\cos(2\pi\nu t + \phi(t))$). A modulated *cw*-ODMR signal recorded with a photo-detector can therefore be described to first order as the sum of the unmodulated steady-state spectrum (4) and a product of two complex phasors rotating in opposite directions, with a time-invariant amplitude also defined by (4):

$$\mathcal{S}_{cw}(\omega_c, t) \quad = \tfrac{1}{2}\mathcal{S}_{cw}(\omega_c) + \tfrac{1}{4}\mathcal{S}_{cw}(\omega_c)[e^{i(2\pi\nu t+\varphi_s)} + e^{-i(2\pi\nu t+\varphi_s)}], \tag{5}$$

where φ_s is the signal phase. Using (5), a lock-in signal $\mathcal{S}_{LI}$ can be described as a time integrated product of a mixed reference signal $\mathcal{S}_{ref}$ and a measured input signal $\mathcal{S}_{cw}$, both modulated at a frequency ν, with an amplification gain factor $\mathcal{A}$, as highlighted in Fig. 2(a):

$$\mathcal{S}_{LI}(\omega_c) = \frac{\mathcal{A}\mathcal{S}_{cw}(\omega_c)}{2\tau}\int_{-\tau/2}^{\tau/2}(e^{i\phi} + e^{-i(4\pi\nu t+\varphi_s+\varphi_r)})dt, \tag{6}$$

where the static component in (5) is removed by the lock-in bandpass filter at its input, and the remaining signal is then re-normalised and multiplied with a sinusoidal reference signal $\mathcal{S}_{ref} = e^{-i(2\pi\nu t+\varphi_r)}$ with a phase difference $\phi = \varphi_s - \varphi_r$, and integrated in time using a low-pass filter with a time constant τ. The integral results in a complex function of the amplified input signal which can be decomposed into an in-phase (X) and quadrature (Y) component:

$$X \quad = \tfrac{1}{2}\mathcal{A}\mathcal{S}_{cw}(\omega_c)\cos(\phi), \tag{7}$$

$$Y \quad = \tfrac{1}{2}\mathcal{A}\mathcal{S}_{cw}(\omega_c)\sin(\phi). \tag{8}$$

These can be measured individually using a two-channel lock-in detector, as schematically illustrated in Fig. 2(a). By measuring the quadratures simultaneously a phase-independent magnitude ($R = \sqrt{X^2 + Y^2}$) can also be obtained. The decomposition of (5) and the resulting expression in (7) or (8) takes on different forms depending on the modulation mechanism. In the case of ODMR, modulation can be applied to either the MW drive, the bias magnetic field, or the polarising laser drive. Modulation of the MW drive is a technically convenient approach with respect to versatility and fine control, as it can usually be controlled directly from the MW source without repercussions for the rest of the experimental setup. Frequency modulation (FM) is preferable to amplitude modulation (AM) as it results in a dispersion line-shape of the spin resonance, which possesses its highest sensitivity (point of maximum slope) on resonance where the signal is zero, while also displaying an approximately linear response for small field changes. In contrast, AM results in a Lorentzian/Gaussian line-shape which possesses its highest sensitivity on the line-shapes side where the signal is not zero and therefore more susceptible to fluctuations and noise in the driving field. An example of measured in-phase (X) lock-in ODMR spectra from an ensemble of $^{14}NV^-$ using an AM or FM MW field is shown in Fig. 2(b,i,ii)

For FM imposed either through the drive frequency or the external bias magnetic field B_z, the detuning δ becomes a function of time. Such a modulation can be either continuous or discrete, and may be represented by modulation functions that are either sine-wave (continuous, ~) or square-wave (discrete, #), respectively:

$$B_{\sim}(t) \quad = \cos(\omega_c t + \beta\sin(2\pi\nu t)) = \textstyle\sum_{n=-\infty}^{+\infty} J_n(\beta)\cos(\omega_c t + n2\pi\nu t), \tag{9}$$

$$B_{\#}(t) \quad = \cos(\omega_c t + \Delta\omega\ \mathrm{sgn}[\cos(2\pi\nu t)]t), \tag{10}$$

where J_n is a Bessel function of the first kind of order n, $\Delta\omega$ is the frequency modulation depth and $\beta = \Delta\omega/2\pi\nu$ is the modulation index. Analysis of the Fourier spectrum of these two

Optics EXPRESS

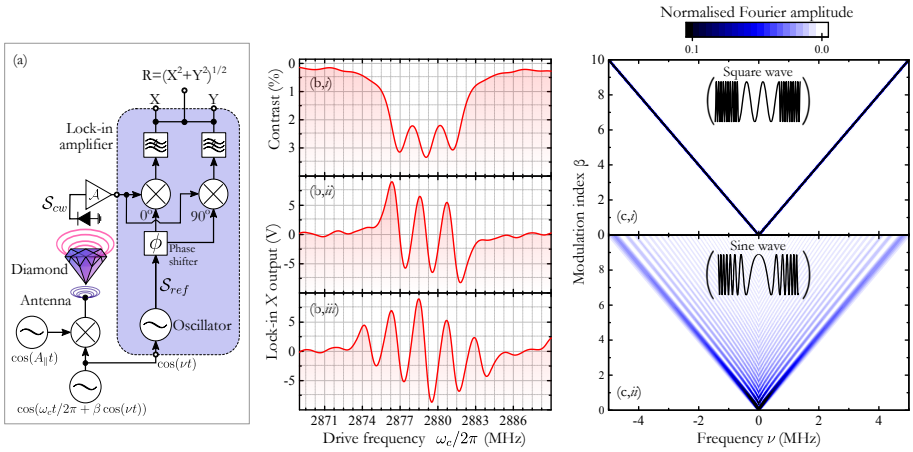

Fig. 2. (a) Schematic of the experimental setup and the two-channel lock-in detector. (b) Measured spectrum of an ensemble of ^{14}NV showing (i) in-phase X lock-in spectrum using an amplitude modulated MW field and plotted in terms of the measured fluorescence contrast, (ii) X lock-in spectrum spectrum using sine-wave single-frequency modulation, and (iii) three-frequency excitation of all hyperfine lines. (c) The Fourier spectrum for (i) $B_{\#}(t)$ (10) and (ii) $B_{\sim}(t)$ (9) as a function of modulation depth $\Delta\omega$, for a fixed modulation frequency ν. The amplitude scale has been reduced to highlight the presence and distribution of peaks in the case of $B_{\sim}(t)$.

functions, shown in Fig. 2(c), provides direct insight into their characteristics. The change in the frequency spectrum as function of β for a fixed ν is stark: $B_{\sim}(t)$ disperses its power over increasingly larger number of frequency components, while for $B_{\#}(t)$ the power remains largely within the two $\Delta\omega$ separated frequencies. Although the bandwidth needed to analytically describe $B_{\sim}(t)$ is infinite, ~99 % of the modulated signal power is present in approximately $n \simeq \lceil\beta\rceil$ frequency components separated by at most $n\nu$ from the central carrier frequency [25]. With these FM functions in mind, expression (6) can be reformulated in terms of $\mathcal{S}_{cw}(\omega_c(t))$ using a Taylor series expansion about ω_c. This results in an approximation of the in-phase/quadrature components X/Y as the difference between two or n out-of phase spectra separated by $\Delta\omega$ or ν, respectively. When $\phi = 0$, the in-phase X output for both modulation functions are:

$$X_{\#}^{FM}(\omega_c) \approx \frac{\mathcal{A}}{2}\left(\mathcal{S}_{cw}(\omega_c + \Delta\omega) - \mathcal{S}_{cw}(\omega_c - \Delta\omega)\right), \tag{11}$$

$$X_{\sim}^{FM}(\omega_c) \approx \frac{\mathcal{A}}{2}\sum_{n=0}^{\lceil\beta/2\rceil} J_n(\beta)\left(\mathcal{S}_{cw}(\omega_c + n2\pi\nu) - \mathcal{S}_{cw}(\omega_c - n2\pi\nu)\right). \tag{12}$$

With the presence of the hyperfine transitions and their considerable overlap, an increased contrast can be achieved by simultaneously exciting all of them. The enhancement of the slope is verified to be in the order of 2 - 3 times depending on the excitation and dephasing rates, and is obtained by mixing ω_c with a frequency equal to the hyperfine separation. For ^{14}NV, this generates the in-phase X lock-in spectrum shown in Fig. 2(b,*iii*). Analytically, this modifies the expressions (11) and (12) with an additional summation over the number of frequency components m_x (which is equal to m_I):

$$X^{A_\parallel}(\omega_c) = \textstyle\sum_{m_x} X^{FM}(\omega_c + m_x 2\pi A_\parallel). \tag{13}$$

Optics EXPRESS

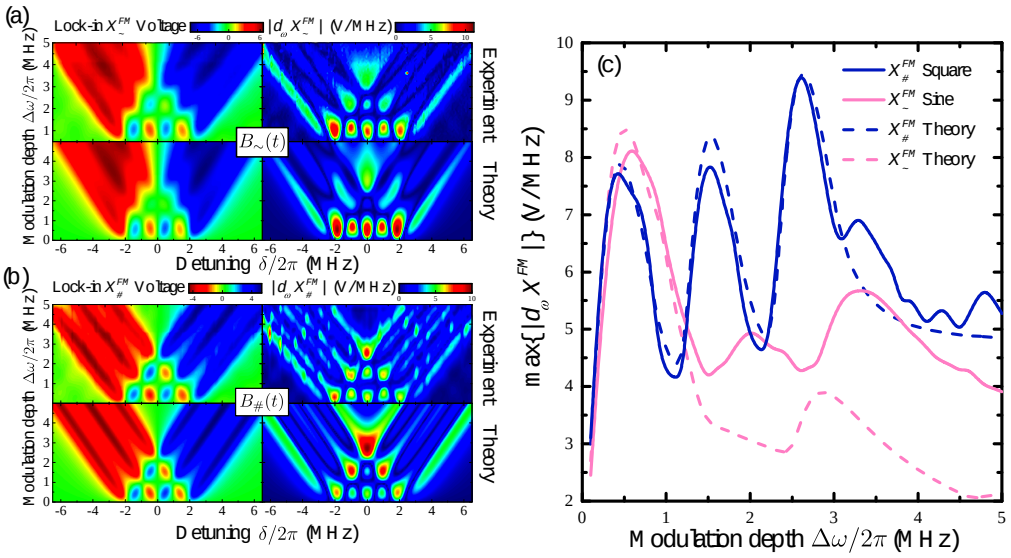

Fig. 3. Experimental and simulated two-dimensional plots of $X^{FM}(\omega_c, \Delta\omega)$ for (a) sine-wave modulated drive and (b) square-wave modulated drive, shown besides their first-order derivative. (c) Experimental and theoretical values of $\max\{|d_\omega X^{FM}(\omega_c)|\}$ as a function of $\Delta\omega$ for both modulation functions. The simulation parameters used for these Figs. are $\Gamma_p/2\pi \simeq 150$ kHz, $\Omega/2\pi \simeq 300$ kHz, and $\gamma_2^*/2\pi \simeq 500$ kHz.

3. Modulation function dependence

3.1. Single and multiple frequency modulation

Given the finite linewidth γ of the individual hyperfine transitions and the constant spectral separation between the hyperfine lines $A_\parallel$, the optimal modulation depth $\Delta\omega$ is expected to occur within the frequency span of all the hyperfine transitions $\sim 2A_\parallel$. Exactly what modulation depth and function is optimal will then depend on γ, which is dependent on both the intrinsic properties of the diamond, and extrinsically on the excitation rates Γ_p and Ω.

To investigate the dependence of the sine- and square-type modulation functions on the maximum achievable slope, we measure the in-phase X spectrum and its maximum absolute slope $\max\{|d_\omega X^{FM}|\}$ as a function of modulation depth $\Delta\omega$. These are shown in Fig. 3(a) for single-frequency sine, and in Fig. 3(b) for square-wave modulation, in comparison to simulated spectra using equations (11) and (12). There is very good agreement between the measured and theoretical spectra, particularly as the subtle difference between square-wave and sine-wave modulation is reproducible. Figure 3(c) plots $\max\{|d_\omega X^{FM}|\}$ for either modulation function for both experimental and theoretical trends. These trends show that, for the given ensemble and measurement parameters, sine-wave modulation gives an optimum $\max\{|d_\omega X^{FM}|\}$ when $\Delta\omega/2\pi$ is $\sim 0.5\gamma$ of a single hyperfine-transition peak ($\sim$ 1 MHz), while square-wave modulation exceeds this when $\Delta\omega/2\pi$ is larger than the full span of the three hyperfine lines at around $\Delta\omega/2\pi$ ~2.5 MHz. This difference is due to two factors, which include the ratio between γ and the frequency separation ($\xi = \gamma/2\pi A_\parallel$), as well as the spectral characteristics of the two modulation functions. Because for a sine-function the MW power is dispersed across a larger bandwidth as the modulation depth is increased, $\max\{|d_\omega X^{FM}|\}$ is reduced because of the decreasing amplitude. While this should be compensated for by increasing ν to maintain a constant β, this is impractical as ν is usually chosen beforehand on the basis of the inherent

Optics EXPRESS

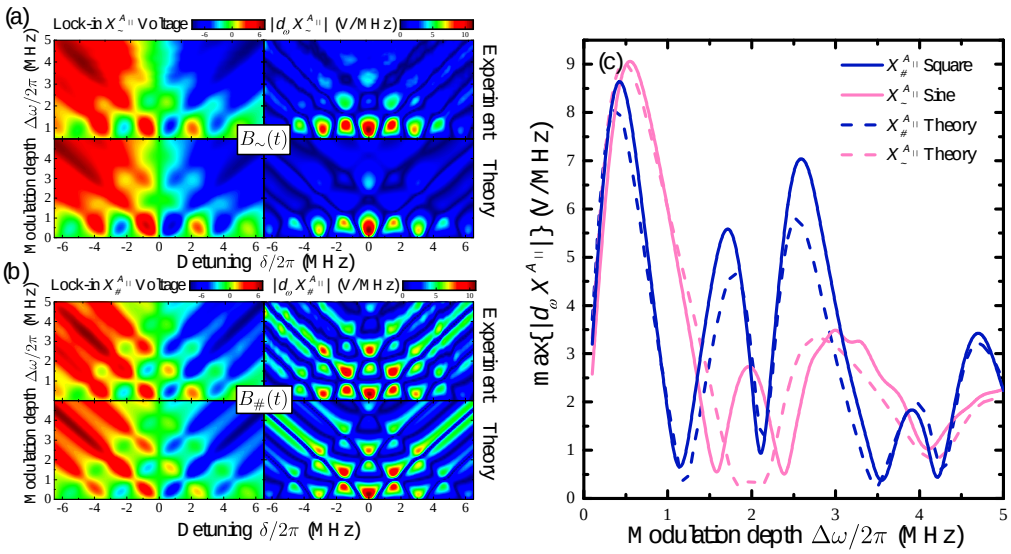

Fig. 4. Experimental and simulated two-dimensional plots of $X^{A\parallel}(\omega_c, \Delta\omega)$ for (a) sine-wave modulated drive and (b) square-wave modulated drive, shown besides their first-order derivative. (c) Experimental and theoretical values of $\max\{|d_\omega X^{A\parallel}(\omega_c)|\}$ as a function of $\Delta\omega$ for both modulation functions. The simulation parameters used for these Figs. are $\Gamma_p/2\pi \simeq 150$ kHz, $\Omega/2\pi \simeq 100$ kHz, and $\gamma_2^*/2\pi \simeq 500$ kHz.

noise spectral density and the bandwidth limitations of the apparatus and the system itself. In comparison, square-wave modulation is by definition discrete, and the distribution of power is, to first order, independent of the modulation parameters. A drawback with square-wave modulation is that when mixing with a sine-wave reference, multiple odd harmonics are generated. This degrades the demodulated amplitude by a factor which is dependent on the signal composition, as some of the power is distributed into these odd harmonics. However the power loss through this mechanism is negligible compared to the amplitude decrease when increasing $\Delta\omega$ of a sine-wave modulated spectrum.

The in-phase X spectrum generated when all hyperfine lines are simultaneously excited is shown for sine-wave modulation in Fig. 4(a), and for square-wave modulation in Fig. 4(b), in comparison to the simulated spectra using equation (13). In contrast to single-frequency excitation, $\max\{|d_\omega X^{A\parallel}|\}$ is obtained for a $\Delta\omega$ that is around half of γ for both modulation functions and the given ensemble and measurement parameters, as highlighted in Fig. 4(c). The discrepancy in this case is related to the effect of the enhanced contrast on $|d_\omega X|$ in relation to ξ, as discussed in the following section.

3.2. *Projected modulation function trends*

In order to study how the modulation function influences the lock-in signal slope, the dependence of the unmodulated signal slope on the optical and MW excitation rate needs to be assessed. Prior to lock-in detection, the linewidth γ and therefore the slope $|d_\omega \mathcal{S}_{cw}|$ is dependant on the excitation ratio Ω:Γ_p, and the effective dephasing rate γ_2'. In particular $\max\{|d_\omega \mathcal{S}_{cw}|\}$ is obtained when the depletion rate of the spin levels $^3\mathbf{A}_2$ by Γ_p is large enough to circumvent the effects of MW power broadening, yet below the pure dephasing rate γ_2* [26, 27]. This is simulated in Fig. 5(a) which plots $|d_\omega \mathcal{S}_{cw}|$ as a function of Ω and Γ_p, and shows an almost 1:1 correspondence for Ω:Γ_p is required to achieve an optimum slope for a given $\gamma_2^*/2\pi \simeq 500$

Optics EXPRESS

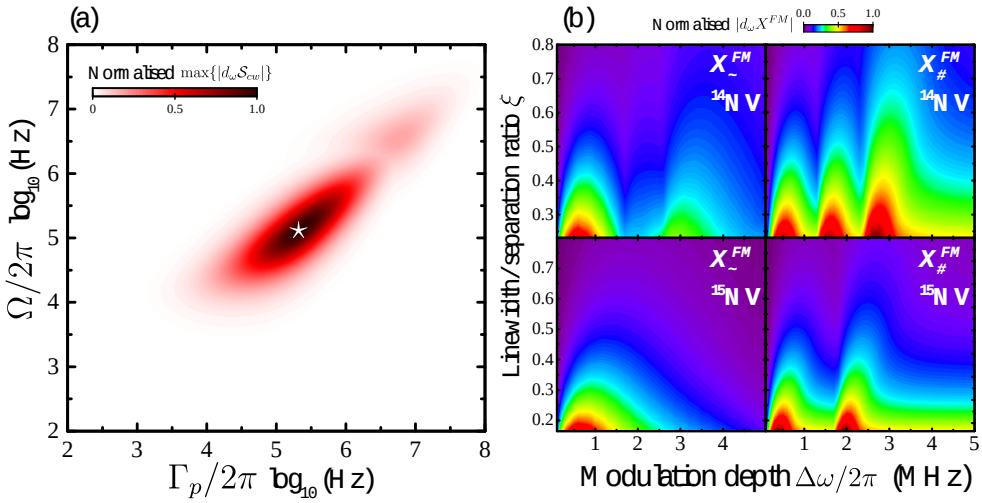

Fig. 5. (a) Simulation of the steepest slope of expression (4) as a function of Rabi frequency Ω and optical excitation rate Γ_p for $\gamma_2^*/2\pi \simeq 500$ kHz and $k_{21}/2\pi = 1$ kHz. The parameters for the maximum slope, designated by a star, are used for the simulations in (b), which show the normalised maximum slope for single frequency excitation as a function of ξ and modulation depth $\Delta\omega$ for sine ($X_\sim^{FM}$) and square ($X_\#^{FM}$) wave modulation for both NV isotopes.

kHz. The optimum point of $\max\{|d_\omega \mathcal{S}_{cw}|\}$ is highlighted by a star, and using these driving rates, $|d_\omega X^{FM}|$ is studied as a function of ξ and $\Delta\omega$ for both modulation functions and isotopic forms of the NV center. These are plotted as a function of ξ and $\Delta\omega$ for single-frequency excitation in Fig. 5(b).

Despite the stark difference between the modulation functions excitation spectrum (shown in Fig. 2(c)), it is the ratio ξ which is observed to be the limiting factor when generating the maximum obtainable slope $\max\{|d_\omega X^{FM}|\}$. As ξ approaches 1/4 for both ^{14}NV and ^{15}NV, the inherent overlap of the hyperfine lines degrades the $|d_\omega X^{FM}|$ values in the region between the peaks, while increasing the overall amplitude and therefore enhancing $|d_\omega X^{FM}|$ in the sides of the peak generated by the sum of all the hyperfine lines. As such, for $\xi > 1/4$, square-wave modulation outperforms sine-wave modulation, and the optimum $\Delta\omega$ will be the full span of all the hyperfine transitions. For $\xi < 1/4$, the difference between square- and sine-wave modulation is negligible, and the optimum $\Delta\omega$ remains within γ for both modulation functions, at values equivalent to $A_\parallel$ for square-wave modulation. Given the inherent $A_\parallel$ values of NVs, these ratios translate into $\gamma/2\pi$ of ~ 0.5 MHz for ^{14}NV, and ~ 0.8 MHz for ^{15}NV. Ultimately, this implies that square-wave modulation is the optimum choice when γ exceeds these values, to maximise $|d_\omega X(\omega_c)|$, and thereby the achievable sensitivity $\delta B \propto [d_\omega X(\omega_c)\gamma_e]^{-1}$.

From these simulations, it is evident that the optimum $\Delta\omega$ is dependent on the relative variation of $|d_\omega X^{FM}|$ within the spectrum: the more 'smeared' a spectrum is, the larger $\Delta\omega$ is needed to optimise $|d_\omega X^{FM}|$. As such, exciting all three transitions increases the contrast without significantly affecting the relative $|d_\omega X^{FM}|$ throughout the spectrum, thereby offsetting ξ to larger values. For simultaneous hyperfine level excitation, a larger ξ ratio is therefore required for square-wave modulation to be advantageous. The simulations highlight a threshold that is increased by a factor proportional to the number of excited hyperfine lines m_I. This behaviour is highlighted in Fig. 6 where $\max\{|d_\omega X_\#^{A_\parallel}|\}$ occurs at a modulation depth that is larger than the inherent linewidth only when $\xi > 3/4$. Ultimately, it should be emphasised that with an increase

Optics EXPRESS

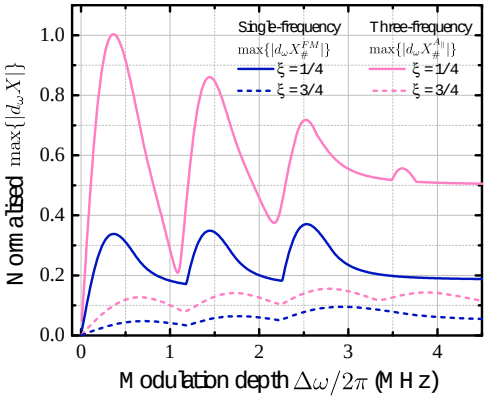

Fig. 6. Comparison of simulated $\max\{|d_\omega X_\#|\}$ for single- and three-frequency excitation of an ensemble of ^{14}NV, using two different ξ values. The normalisation is with respect to the maximum simulated slope, and the ξ values correspond to a linewidth of ~ 0.5 MHz and ~ 1.6 MHz.

in ξ, $\max\{|d_\omega X|\}$ is inherently degraded. The optimum scenario will therefore always occur with three-frequency excitation and ensembles possessing as low a ξ ratio as possible, for which there is no advantage in using either modulation function.

4. Conclusion

In this work we identify the optimum lock-in modulation parameters for obtaining the steepest spectral slope in the ODMR spectra measured from a low-density ensemble of ^{14}NV, for the purpose of *cw*-sensing of magnetic fields. Experimental measurements of the in-phase lock-in spectra from a ^{14}NV ensemble as a function of modulation depth and modulation function highlighted the advantage of square-wave modulation for the given sample. This also provided an assessment check for the spectral simulations based on a five-level set of optical Bloch equations and its reformulation in terms of a modulated drive frequency. Through accounting for the spectral difference of the modulation functions, this model was able to accurately reproduce the experimentally observed subtleties in the lock-in spectra. Their correspondence provides confidence to the simulated projections, which highlight the key relationship between $\Delta\omega$ and ξ. In particular, this showed that for single-frequency excitation when $\xi \gtrsim 1/4$, square-wave modulation is optimal with a $\Delta\omega$ which spans the sum of all the hyperfine linewidths. Below this threshold, there is no significant advantage in using either modulation functions. For NVs, this translated into linewidth limits of ~ 0.5 MHz for ^{14}NV, and ~ 0.8 MHz for ^{15}NV. Ultimately, the model indicates that an optimum slope will always be achieved with as low a ξ ratio as possible, with multi-frequency excitation and a modulation depth that is within the hyperfine linewidth, irrespective of the modulation function.

It is anticipated this analysis will benefit the development and optimisation of NV-based sensing schemes and devices, while the simplicity of the presented model should allow for its easy re-modification for alternative systems with different spectral properties. This is envisaged especially as many off-the-shelf NV ensembles display poor ξ ratios, and the production of optimised isotopically-pure diamonds is resource and time intensive. Aside from this, the relationship delineated here may be relevant to any spectral measurement or *cw*-sensing scheme which uses closely-spaced spectral features that respond identically to external perturbations.

Optics EXPRESS

A. Analytical solution to steady-state fluorescence ratio derived from the 5-level Bloch equations

The steady-state solutions for equation (3) detailed in section two of the manuscript (using notation with respect to Fig. 1(a)) is given as:

$$\begin{aligned}\mathcal{I}_{cw} &= \frac{\Gamma_p(k_{31}+k_{32})}{K_3^2}\left[1+\Xi+\frac{\Gamma_p}{K_3}+\frac{\Gamma_p\Xi}{K_4}+\frac{k_{35}\Gamma_p}{K_3K_5}+\frac{k_{45}\Gamma_p\Xi}{K_5K_4}\right]^{-1} \\ &+ \frac{\Gamma_p(k_{41}+k_{42})}{K_4^2}\left[1+\frac{1}{\Xi}+\frac{\Gamma_p}{K_4}+\frac{\Gamma_p}{K_3\Xi}+\frac{k_{45}\Gamma_p}{K_4K_5}+\frac{k_{35}\Gamma_p}{K_5K_3\Xi}\right]^{-1},\end{aligned} \tag{14}$$

where

$$\Xi = \frac{\left[\left(\frac{k_{21}}{2}\right)+\left(\frac{\Gamma_p(k_{32}K_5+k_{52}k_{35})}{K_3K_5}\right)+\left(\frac{\Omega^2\gamma_2'}{2(\gamma_2'^2+\Delta^2)}\right)\right]}{\left[\Gamma_p+\left(\frac{k_{21}}{2}\right)-\left(\frac{\Gamma_p(k_{42}K_5+k_{52}k_{45})}{K_4K_5}\right)+\left(\frac{\Omega^2\gamma_2'}{2(\gamma_2'^2+\Delta^2)}\right)\right]}, \tag{15}$$

$$K_3 = k_{31}+k_{32}+k_{35}, \quad K_4 = k_{41}+k_{42}+k_{45}, \quad K_5 = k_{51}+k_{52}, \tag{16}$$

Funding

Danish Innovation Foundation (EXMAD, the Qubiz centre); Danish Research Council (Sapere Aude DIMS).

Acknowledgments

We would like to thank Kristian Hagsted Rasmussen for help with diamond sample preparation.

Chapter 5

Pump-Enhanced Continuous-Wave Magnetometry

5.1 Introduction

The NV center is a promising platform for sensing weak magnetic fields with high spatial resolution at room temperature. In this chapter, we report on a magnetometer enhanced by an optical cavity. We use a CVD diamond with a low concentration of NV centers, ~ 2 pbb, and construct a split-ring resonator to deliver a uniform MW field to the diamond. The optical cavity enables us to reach a linewidth-narrowing regime which optimizes the ODMR slope and enhances the sensitivity.

We extracted a sensitivity of ~ 3 nT/$\sqrt{\text{Hz}}$ and incorrectly concluded a measured magnetic noise floor of ~ 200 pT/$\sqrt{\text{Hz}}$. Later, we realized there was a calibration error in Fig. 5(a) in Section 6.2. The error occurred in the calculation of the ASD. The noise density is off by a factor of $\sqrt{250}$. The corrected noise density is shown in Fig. 5.1 in this section. The magnetically insensitive trace plots a magnetic noise floor of ~ 3 nT/$\sqrt{\text{Hz}}$, which explains the discrepancy between the measured noise floor and the extracted sensitivity.

We obtain a bandwidth of 159 Hz followed by a 6 dB/octave roll-off that is generated by the low-pass filter of the LIA. The magnetically sensitive trace contains a low-frequency magnetic noise that is mainly caused by temperature fluctuations. Furthermore, a pronounced environmental magnetic noise at 50 Hz and its harmonics are visible in the spectrum.

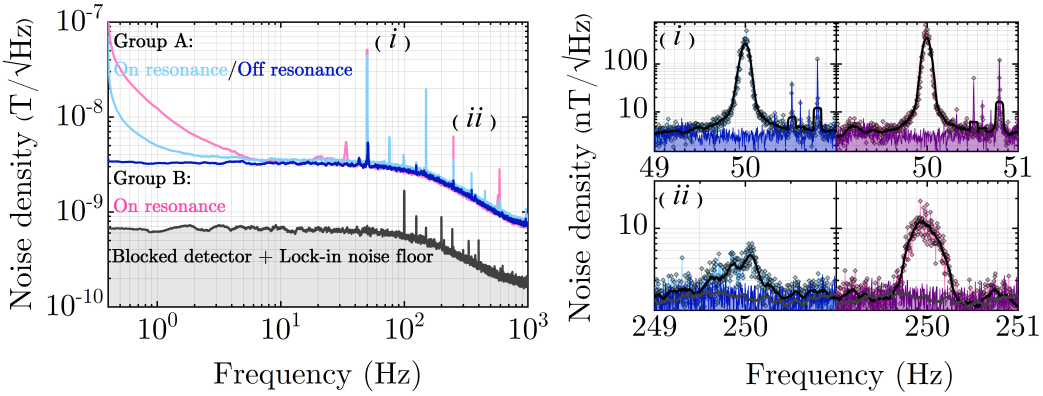

Figure 5.1: Plots of the magnetic noise spectral density when on resonance ($\omega_c = \omega_0$) and off resonance ($\omega_c >> \omega_0$) for both groups A and B with $\Omega \sim 0.55$ MHz and $\Gamma_p \sim 0.3$ MHz ($P_{in} \sim 0.4$ W). The combined noise floor of the LIA and photodetector for the lowest LIA gain settings, assuming a similar $\max\{d_\omega S_{\mathrm{LI}}\}$ to that of A, is also plotted. The plots are averaged from five subsequently measured frequency traces and are smoothed using a Savitzky-Golay filter. Magnified plots of the peaks designated (i) and (ii) show unsmoothed data points with the smoothed traces, highlighting the detection and lack of detection of the 50-Hz magnetic hum and its second odd harmonic when on or off resonance. The differences in amplitude are attributed to varying laboratory conditions.

5.2 Publication

This section was published in Physical Review Applied with the title of "Pump-Enhanced Continuous-Wave Magnetometry Using Nitrogen-Vacancy Ensembles" as follows:

Pump-Enhanced Continuous-Wave Magnetometry Using Nitrogen-Vacancy Ensembles

Sepehr Ahmadi, Haitham A. R. El-Ella,* Jørn O. B. Hansen, Alexander Huck, and Ulrik L. Andersen

Department of Physics, Technical University of Denmark, 2800 Kongens Lyngby, Denmark

(Received 27 March 2017; revised manuscript received 24 May 2017; published 5 September 2017)

Ensembles of nitrogen-vacancy centers in diamond are a highly promising platform for high-sensitivity magnetometry, whose efficacy is often based on efficiently generating and monitoring magnetic-field-dependent infrared fluorescence. Here, we report on an increased sensing efficiency with the use of a 532-nm resonant confocal cavity and a microwave resonator antenna for measuring the local magnetic noise density using the intrinsic nitrogen-vacancy concentration of a chemical-vapor deposited single-crystal diamond. We measure a near-shot-noise-limited magnetic noise floor of 200 $\mathrm{pT}/\sqrt{\mathrm{Hz}}$ spanning a bandwidth up to 159 Hz, and an extracted sensitivity of approximately 3 $\mathrm{nT}/\sqrt{\mathrm{Hz}}$, with further enhancement limited by the noise floor of the lock-in amplifier and the laser damage threshold of the optical components. Exploration of the microwave and optical pump-rate parameter space demonstrates a linewidth-narrowing regime reached by virtue of using the optical cavity, allowing an enhanced sensitivity to be achieved, despite an unoptimized collection efficiency of $< 2\%$, and a low nitrogen-vacancy concentration of about 0.2 ppb.

DOI: 10.1103/PhysRevApplied.8.034001

I. INTRODUCTION

The nitrogen-vacancy (N-V) center, an atomlike defect within a diamond crystal lattice, is an auspicious quantum sensor because of its readily polarized and detected spin state [1]. The characteristics of the N-V center combine high sensitivity and spatial resolution allowing for the detection of spatial temperature gradients [2,3], electric fields [4], and magnetic fields [5–7]—all at room temperature—by measuring the fluorescence contrast via optically detected magnetic resonance (ODMR). By using an N-size ensemble of N-V centers, the collective sensitivity is improved by a factor of $N^{-1/2}$ [8]. Developing diamond ensemble-based magnetic sensors presents advantages over their atomic-vapor and superconducting equivalents, particularly in terms of their relative simplicity, integrability in a variety of devices, and biological compatibility [9]. The methods developed for the collective control and readout of a N-V ensemble for sensing applications should also be useful for scalable quantum-information schemes using ordered ensembles [10], or for potentially coupling N-V ensembles to atomic vapors to create hybrid quantum systems for fundamental and applied experiments [11].

In this article, we present a proof-of-principle system for continuous-wave N-V-ensemble-based magnetometry which combines an optical and a microwave resonator. In combination with lock-in amplification and the simultaneous excitation of all three hyperfine lines, a near-shot-noise-limited noise floor of approximately 200 $\mathrm{pT}/\sqrt{\mathrm{Hz}}$ is achieved from the inherent ^{14}N-V^- concentration of an off-the-shelf single-crystal diamond (approximately 0.2 ppb) while collecting an estimated $< 2\%$ of the generated fluorescence. To put these parameters in context, assuming that sensitivity unquestionably scales with $N^{-1/2}$ and the detection efficiency, the work presented here should be compared to, for example, Refs. [12,13], which report measured sensitivities in the roughly 15- and 290-$\mathrm{pT}/\sqrt{\mathrm{Hz}}$ ranges, respectively, using highly engineered diamonds with enhanced N-V concentrations > 100 ppb and a detection efficiency that is $> 15\%$. The system presented in this article shows comparable sensitivity despite the lower concentration and collection efficiency, and it is anticipated to provide a solid foundation for developing further optimized and miniaturized cavity-based devices. These devices are to be implemented and combined in a variety of sensing applications, most notably in scenarios involving live biological tissue. Other works which report pT-fT sensitivities using N-V ensembles include that of Refs. [14,15]; however, these reported sensitivities are limited to ac fields, as they are achieved using spin-echo pulse sequences—unlike the continuous-wave approach presented in this work, which is applicable to both dc and ac fields.

The first section of this article briefly overviews the motivation of this work, followed by an overview of the N-V-center electronic structure, along with the experimental methods used. This overview is followed by a discussion of the optical-cavity parameters and a brief assessment of the system's total optical loss, leading to an estimate of the number of N-V centers collectively excited and the proportionality between the intracavity power and the ensemble excitation rate. Next, the ODMR spectrum and its equivalent lock-in spectrum are presented, and the characteristics of the optimal parameters reachable with our

*haitham.el@fysik.dtu.dk

current configuration are discussed. The measured spectra are compared with a theoretical model which highlights the occurrence of linewidth narrowing and allows for the derivation of an optimum shot-noise-limited sensitivity. Finally, measurements of the magnetic noise spectral density and an external magnetic field using the optimized system are presented.

II. EXPERIMENTAL METHOD AND SETUP

Obtaining high densities and efficiently employing them in a sensing scheme poses complications in terms of collective control and signal readout. Specifically, the inherent difficulties with increased densities spanning larger volumes involve insufficient collective polarization, inhomogeneous broadening, and nonoptimal signal collection.

Large densities are usually obtained through high-temperature high-pressure growth or extended nitrogen ion implantation and annealing, both of which suffer from poor N-to-N-V conversion efficiencies ($< 20\%$ [16]) and lead to a large concentration of N nuclear spins (in the form of single and aggregate substitutional defects) alongside ^{13}C nuclear spins. These nuclear spins inhomogeneously broaden the collective N-V spin resonance, and while such broadening can be mitigated by using ^{12}C purified diamond [17], the problem of low N-V creation efficiencies accompanying degradation of the collective coherence and crystal integrity still remains. At the same time, efficient collection of the generated fluorescence involves circumventing the limitations of the high refractive index of diamond, which results in a small critical angle of escape and significant light loss through total internal reflection. Different approaches have been studied to overcome this problem, involving, e.g., applying a solid immersion lens [18,19], coupling N-V centers to photonic crystals [20], using a dielectric antenna [21] or side-collection detection [14]. Alternative strategies intended to circumvent these issues have also been explored through sensing based on cavity-assisted absorption of the shelving state [22,23], and amplifying the ODMR fluorescence by trapping pump light within the diamond through total internal reflection [13].

In general, single and ensemble N-V-based continuous-wave sensing is limited by the ratio of the spectral ODMR linewidth to the fluorescence contrast. For a given ensemble, maximizing this ratio requires spatially uniform spin polarization and readout pump rates across the ensemble volume, which allows a saturated fluorescence regime to be reached. Reaching a saturated regime becomes more difficult with increasing ensemble volume and density, given (a) the negligible absorption cross section of single N-V centers, (b) the spatial inhomogeneity of the nuclear spin bath, (c) the generated spin noise resulting from spatially inhomogeneous fields which can only identically polarize a fraction of the ensemble, and (d) the inherent power broadening that accompanies increased polarization rates to maximize ODMR fluorescence contrast. One method of collectively tackling these issues is through addressing the spatial uniformity and efficiency of the spin polarization and readout pump fields with respect to a given ensemble volume, while ensuring that the readout pump rate is large enough to counteract power broadening [24]. In this work, these issues are addressed by using an optical cavity resonant with the readout pump light, in conjunction with a microwave split-ring resonator antenna. The antenna allows for a spin-polarizing field to be applied uniformly across the ensemble volume that is excited by the readout pump, while the cavity amplifies the power of the input beam to collectively excite the ensemble at a fast-enough rate to reach a linewidth-narrowing regime.

The electronic configuration of the N-V center [a simplified schematic is shown in Fig. 1(a)] exhibits spin-dependent fluorescence by virtue of the difference between the $|m_s = \pm 1\rangle$ and the $|m_s = 0\rangle$ spin-level intersystem crossing rates (k_I) from the ^3E excited triplet state to the shelving singlet states ($^1A_1 \leftrightarrow {}^1E$). In a simplified continuous-wave (CW) picture for an ensemble of identical systems, the radiative relaxation rate (k_r) of all of the excited-state levels competes with k_I to bring about a fluorescence contrast ($\mathcal{C}$) based on the initial distribution of the spin-state population in the triplet ground states ($^3A_2$). This ground-state spin population is set by the ratio between the optical readout pump rate (Γ_p) from above-band excitation (in this case, a 532-nm laser), and the resonant microwave (MW) drive rate of the spin levels (Rabi frequency, Ω), of which the optical above-band excitation mechanism is near-perfectly spin conserving. The presence of a local magnetic field breaks the degeneracy of the $|m_s = \pm 1\rangle$ spin levels in the ground and excited states, splitting them with a scaling proportional to the product of the gyromagnetic ratio of $\gamma_e \sim 28$ MHz/mT and the projection angle of the field along the N-V symmetry axis. The four possible crystallographic orientations of a single N-V within the diamond unit cell (along all four $\langle 111\rangle$ directions) result in four distinct N-V group alignments for a given magnetic field. In the experimental setup, the splitting of these groups is tuned via the placement of a permanent rare-earth magnet on a three-axis translation stage in the vicinity. A coil magnet is also placed next to the diamond (offset from the optical-cavity path) to generate weaker fields for assessing the system's response to low-frequency ac magnetic fields. The presence and magnitude of a local magnetic field is directly detected by monitoring the change in fluorescence of one of these aligned groups as a function of the applied MW frequency $\omega_c/2\pi$. As a result, the detection sensitivity using the ODMR spectrum $\mathcal{S}_{\mathrm{CW}}$ is limited by the inverse of the maximum MW-dependent rate of fluorescence change, $[\max\{d_\omega \mathcal{S}_{\mathrm{CW}}\}]^{-1}$, where d_ω denotes the derivative with respect to the MW frequency.

Confocal cavity-assisted ODMR is carried out using the native ^{14}N-V^- concentration of a polished and untreated single-crystal diamond ($6 \times 6 \times 1.2$ mm, Element Six)

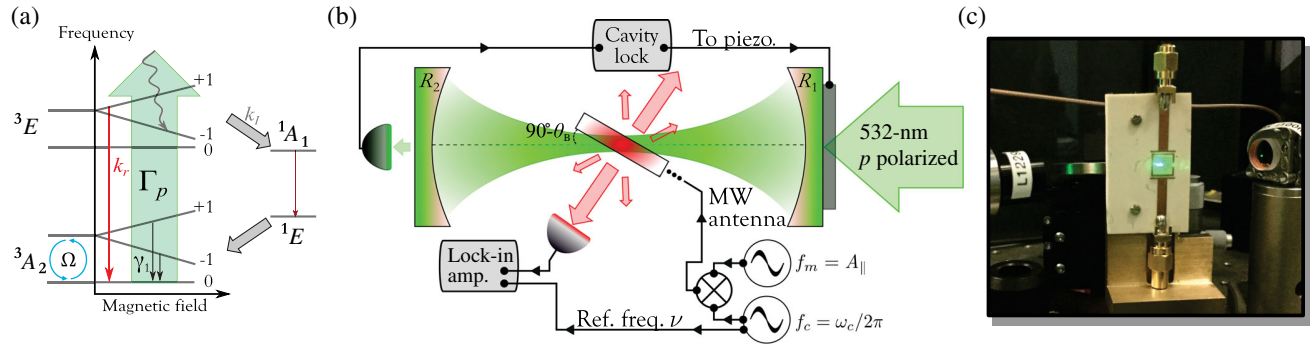

FIG. 1. (a) A simplified diagram of the N-V energy levels, highlighting the most significant decay and excitation pathways described in the text, as well as the splitting of the ground- and excited-state spin levels as a function of external magnetic field strength. (b) Simplified schematic of the experimental setup highlighting the most essential components used to measure ODMR from the diamond. The diamond is placed at a Brewster angle θ_B relative to the cavity axis, which is defined by two mirrors with reflectivities R_1 and R_2, where the input mirror reflectivity $R_1 < R_2$. The cavity is pumped through the input mirror with phase-modulated p-polarized light and is locked using the PDH technique with a servomechanism that monitors the transmitted light through R_2 and actuates a piezoelectric stack attached to R_1. The N-V resonance is driven by a modulated frequency $f_c = \omega_c/2\pi$ that is mixed with $f_m = A_\parallel = 2.16$ MHz generated from a second signal generator. An antenna attached to the apertured diamond holder is used to deliver the mixed drive frequency. A modulation reference signal at frequency ν is sent to a lock-in amplifier which is connected to the detector measuring the ODMR fluorescence generated from the diamond. (c) A picture of the diamond mounted on the apertured MW antenna, placed between the cavity mirrors.

grown using chemical vapor deposition (CVD), with a quoted substitutional nitrogen concentration [N_s] of < 1 ppm. The diamond is mounted on a homebuilt apertured circuit board, patterned with a MW split-ring resonator and, as shown in the schematic in Fig. 1(b), placed vertically between two confocal-cavity mirrors at a Brewster angle of $\theta_B = 67° \pm 0.4°$ relative to the cavity's longitudinal axis. Both cavity mirrors, R_1 and R_2, have a curvature radius of 10 cm and are antireflection coated for 532 nm on the flat ends. The measured reflectivities are $R_1 = 94.8\% \pm 0.1\%$ and $R_2 = 99.8\% \pm 0.1\%$, giving a projected finesse of 113 ± 4. The measured finesse of the empty cavity is $\mathcal{F} = 114$, shown in Fig. 2(a), agrees well within the error of the projected value. An unequal mirror reflectivity is chosen in order to approach impedance matching conditions when incorporating the diamond. The cavity is pumped with a phase-modulated and p-polarized 532-nm laser possessing a single longitudinal mode (Verdi SLM Coherent, rms $< 0.03\%$ from 10 Hz–100 MHz), and Pound-Drever-Hall (PDH) locked using the transmitted light through R_2, and a piezoelectric actuator attached to the R_1 mirror mount. The confocal configuration of these mirrors results in a Laguerre-Gaussian LG_{00} mode with a $1/e$ beam waist of 92 μm and a Rayleigh length of approximately 50 mm. With the diamond incorporated at its θ_B angle, and accounting for the standing-wave spatial intensity profile, an effective $1/e$ excitation volume of about 3.5×10^{-2} mm^3 is obtained, considering the LG_{00} transverse beam profile. The overall influence of the spatial standing-wave intensity variations are observed to be negligible when performing comparative measurements with and without the use of the cavity mirrors for similar optical excitation powers. Owing to the expected uniform spatial distribution of the N-V centers, the same total fluorescence rate is expected when comparing a flat and $\sin^2$ spatial profile with the same average intensity.

For sensing-based measurements, fluorescence is collected directly from the large face of the diamond using either a NA = 0.7 objective (Mitutoyo, with an approximate transmission efficiency of 77% at 700 nm), or a NA = 0.79 condenser lens (Thorlabs ACL25416U-B, with an approximate transmission efficiency of 99.7% at 700 nm) and filtered using a long-pass filter with a 600-nm cut-on wavelength. Considering the refractive index of diamond, the numerical aperture of the objective, and the loss from the remaining optical components, the total collection efficiency is estimated to be $< 2\%$. The collected fluorescence is focused onto a Si-biased detector (Thorlabs DET36A with an approximate quantum efficiency of 70% at 700 nm) attached with a 10 kΩ load resulting in a 400-kHz detection bandwidth. The detected signal is noise filtered and amplified using a lock-in amplifier (Stanford Research Systems SR510) through either amplitude or sine-wave frequency modulation of the MW drive (30-kHz modulation rate and 0.5-MHz modulation depth), for which the in-phase quadrature is output. The lock-in amplifier input is set with a bandpass filter centered at the modulation frequency (6-kHz bandwidth), and the output is set with a 1-ms time constant, thereby imposing a first-order low-pass filter with a corner frequency at 159 Hz. For simultaneously driving all three ^{14}N hyperfine lines, the modulated MW is mixed with a 2.16-MHz drive (corresponding to the axial hyperfine splitting frequency $A_\parallel$). The MW drive frequency $\omega_c/2\pi$ is delivered using a split-ring resonator which has a measured resonance at 2.884 GHz and a bandwidth of about 91 MHz. The spatial uniformity of the delivered MW power

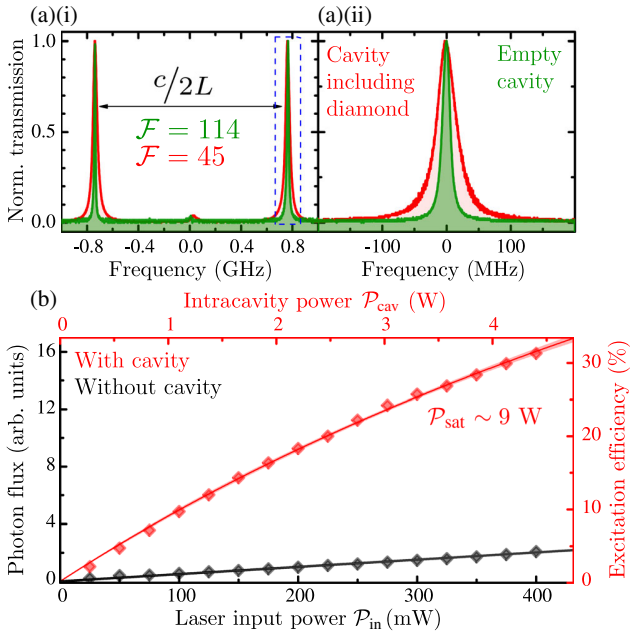

FIG. 2. (a)(i) Transmission spectrum of the cavity as a function of the laser frequency detuning for the cavity without (green) and with (red) the diamond, showing the dominance of the LG_{00} mode and a small negligible peak of the LG_{01} mode (evident from the displacement by half of the free spectral range) for both instances. (a)(ii) Enlargement of one of the transmission peaks highlighting the linewidth increase from approximately 6.5 to 17 MHz. (b) Relative power-dependent photon flux in arbitrary units for the collected light from the diamond without (black points) and with (red points) the cavity, plotted as a function of the cavity input $\mathcal{P}_{in}$ and intracavity powers $\mathcal{P}_{cav}$. The excitation efficiency $\mathcal{R}/\mathcal{R}_{sat}$ is also shown on the right scale for the cavity-enhanced photon flux. The black trace is a linear fit, while the red trace is a power-law fit, as discussed in the text.

is deduced from spatially dependent measurements of the Rabi frequency Ω using confocal microscopy, which is observed to vary by $< 2.5\%$ over a region of about 1 mm^2, across the 1.2-mm thickness of the diamond. The equivalent Ω of the applied MW power is determined using pulsed excitation in the cavity configuration.

III. CAVITY-ENHANCED ODMR READOUT

A. Characteristics of the confocal cavity

The enhancement of the input laser power by the confocal cavity is estimated directly from the measured finesse, $\mathcal{F}$. With the inclusion of the diamond and its associated absorption losses, a 60.5% reduction of the finesse is observed down to $\mathcal{F} = 45$, as shown in Fig. 2(a), along with a full free spectral range scan highlighting the dominance of the LG_{00} mode. The on-resonance relationship between the intracavity power $\mathcal{P}_{cav}$ and the input power $\mathcal{P}_{in}$ is $\mathcal{P}_{cav} \simeq \mathcal{P}_{in} T_1/(1-\varrho)^2$, where T_1 is the transmission of the input mirror and $\varrho = \sqrt{R_1 R_2 e^{-\alpha}}$ is the cumulative round-trip loss product, with α being the propagation-loss coefficient. ϱ is calculated from the polynomial root of its relation with $\mathcal{F}$ through $\mathcal{F}\varrho + \pi\sqrt{\varrho} - \mathcal{F} = 0$ and, in the absence of the diamond, is assumed to be a function solely dependent on the product of $R_1 R_2$. Using this relationship, a measured power-dependent flux rate is plotted in Fig. 2(b) as a function of $\mathcal{P}_{cav}$ and $\mathcal{P}_{in}$. A clear transition from a linear to a nonlinear dependence is observed which is fitted with $\mathcal{R} = \mathcal{R}_{sat}\mathcal{P}/(\mathcal{P} + \mathcal{P}_{sat})$ to estimate the excitation efficiency $\mathcal{R}/\mathcal{R}_{sat}$ and the projected saturation power $\mathcal{P}_{sat}$. The excitation efficiency is estimated to reach about 31% for $\mathcal{P}_{in} \sim 0.4$ W and 50% for $\mathcal{P}_{in} \sim 0.87$ W, for which the latter corresponds to an intracavity power of $\mathcal{P}_{sat} \sim 9$ W.

By measuring the finesse of the empty cavity, the product of the two mirror reflectivities, $R_1 R_2$, is determined with adequate precision. This determination of $R_1 R_2$ from an empty cavity allows for the reasonable assumption that the product α from the measured finesse of the loaded cavity is attributable solely to the diamond. This loss is composed of diamond bulk- and surface-based absorption, $\alpha_{ab}\ell$ and α_{surf}, birefringence-related loss α_{br}, and scattering losses α_{sc} due to surface-roughness-based scattering for every round-trip: $\alpha = \alpha_{ab}\ell + 4\alpha_{surf} + 4\alpha_{sc} + \alpha_{br}\ell$. Given the magnitudes of power, the laser wavelength, and the 600-nm cut-on wavelength of the bandpass filter, loss associated with the discharging of ^{14}N-$V^- \rightarrow {}^{14}$N-V^0 is considered to be negligible [25]. To decompose α, the amount of green light reflected from the surface of the diamond while the cavity is locked is measured. The total fraction of this reflected power to intracavity power corresponds to about 0.006, of which approximately 80% is s-polarized light. Using this measured reflection-based loss, and assuming that surface absorption is negligible (as the surfaces are cleaned with acid and constitute a negligible fraction of the beam path), an absorption-loss coefficient of $\alpha_{ab} \sim 0.0301$ mm^{-1} is estimated for $\ell = 2 \times 1.3$ mm.

Apart from the absorption of N-V^-, absorption around 532 nm can also be attributed principally to the nitrogen-vacancy-hydrogen (N-V-H) defect inherent in CVD-grown diamond [26]. Using the reported absorption coefficients in Ref. [26] for similar CVD diamonds ($\alpha_{\text{N-}V^0\text{-H}} \sim 0.03$ mm^{-1}), along with the absorption cross section of N-V reported in Ref. [27] ($\sigma_{\text{N-}V} = 3.1 \times 10^{-15}$ mm^2), the [N-V^-] concentration can be approximated through $\alpha_{ab} \approx \sigma_{\text{N-}V}[\text{N-}V^-] + \alpha_{\text{N-}V^0\text{-H}}$. An estimated concentration of about 6×10^{10} mm^{-3} is achieved, which translates to approximately 0.2 ppb ^{14}N-V^- (about 0.02% of the quoted [N_s] upper-bound concentration). These estimated concentrations are corroborated with estimates obtained through fluorescence count-rate measurements which indicate a concentration of about 0.16 ppb. Altogether, an order of magnitude estimate of 10^9 N-V^- within the excitation volume is determined. Although the inability to exactly discern competing absorption species and their mechanisms results in a large uncertainty in using

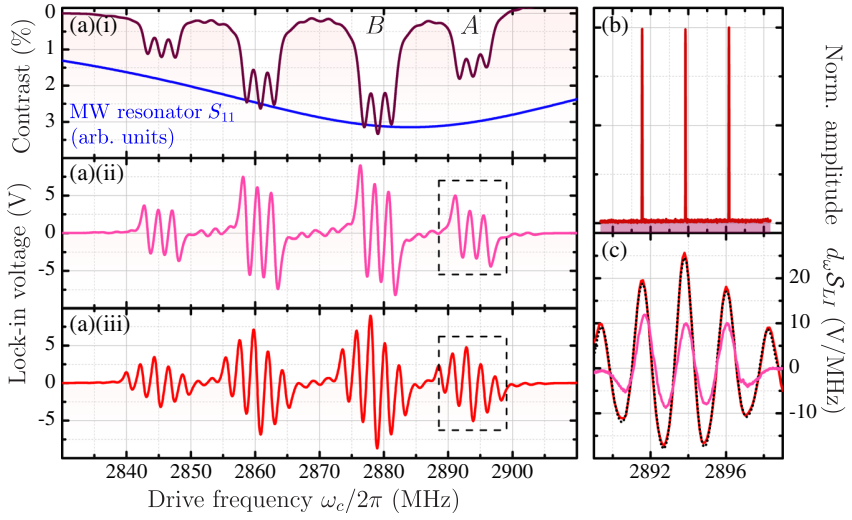

FIG. 3. (a)(i) Amplitude-modulated lock-in spectrum (purple trace) plotted in units of measured signal contrast as a function of MW drive frequency, with the frequency-dependent reflection parameter (S_{11}) of the split-ring resonator antenna (blue trace) incorporated for comparison (not sharing the y axis with the red trace). The frequency-modulated spectrum using single-frequency excitation (a)(ii) and three-frequency excitation (a)(iii) are shown for comparison. (b) Measured three-frequency excitation spectrum (a wide-span measurement is shown in the Supplemental Material [28]). (c) Plot of the derivative $d_\omega \mathcal{S}_{\mathrm{LI}}$ of peak A outlined in (a)(ii) and (a)(iii) using the same color. A simulation of the signal using Eq. (4) is overlaid with the measured trace in (a)(iii) (the black dotted line).

these assumptions, the estimate represents a realistic order of magnitude which reflects values reported in the literature for similar CVD diamonds, and from which the proportionality between the intracavity pump power and the excitation rate can be estimated to be on the order of $\varepsilon \sim 0.3$ kHz/mW.

B. Lock-in amplified magnetic resonance detection

The full ODMR spectrum of the $^3A_2$ spin states and the corresponding lock-in detected signals are shown in Fig. 3. The spectrum in Fig. 3(a)(i) is obtained through lock-in amplification using a pulsed MW signal, and highlights the deliberate alignment of the external magnetic field along one of the $\langle 111 \rangle$ crystallographic directions, as well as the influence of the split-ring resonator bandwidth. Given the four possible crystallographic orientations of the N-V defect, perfect alignment with only one axis orientation at a time is possible for a simple magnetic field, which brings about the spin-level degeneracy of the three other orientations. For an ensemble, splitting of the lines is generally desired in order to circumvent the degraded resonance line shape resulting from residual stray fields that break the degeneracy of the four subgroups. It is also necessary in the case of pulsed schemes where optimal coherence times are required [29], but these advantages are brought about at the expense of contrast, which is clearly visible in Fig. 3(a)(i) when comparing the leftmost peak to the two inner peaks. In the case of CW measurements and sensing schemes, such splitting is not strictly required and the advantage in detection of the enhanced contrast of three degenerate lines outweighs the reduced collective coherence. However, the three subgroups' sensitivity is degraded by the nonparallel projection angle of an external magnetic field. Irrespective of how the sensed field is aligned with respect to the three subgroups, the gyromagnetic ratio is—at best—reduced by a factor of $\cos(54.7°)$.

The amplitude ratios of the outer and inner peaks, designated here as group A and group B, respectively [labeled in Fig. 3(a)], do not possess a 1:3 ratio in this case due to the use of the split-ring resonator, which ensures more spatially uniform power delivery at the expense of power uniformity over the desired ODMR frequency window. The S_{11} trace of the loaded MW resonator is overlaid in Fig. 3(a)(i) (in normalized arbitrary-loss units) and shows a peak at around 2.884 GHz, which is centered between the $|m_s = +1\rangle$ spin levels of groups A and B.

As introduced previously, the sensitivity of the resonances to the presence of fluctuating fields is directly proportional to $[\max\{d_\omega \mathcal{S}_{\mathrm{CW}}\}]^{-1}$. This product can be enhanced by modulating the MW field and amplifying the resulting ac signal using a lock-in detector, resulting in a frequency-modulated ODMR signal $\mathcal{S}_{\mathrm{LI}}$, which is proportional to the derivative of the unmodulated signal and is shown in Fig. 3(a)(ii). The resulting spectra displays features with slopes that are approximately 2× steeper, and presents a higher field sensitivity at the expense of the lock-in-imposed bandwidth. However, due to the presence of three hyperfine levels from the ^{14}N nuclear spin and their considerable spectral overlap, single-frequency excitation results in an unoptimized contrast—and therefore a reduced $\max\{d_\omega \mathcal{S}_{\mathrm{LI}}\}$—relative to the optimal contrast expected from a single ideal spin resonance. The reduced contrast may be mitigated by either working at the excited-state level anti-crossing regime where all N nuclei are polarized upon green-light excitation [30], or by simultaneously exciting all three frequencies, which should result in the same enhanced contrast, using the measured MW excitation frequency spectrum shown in Fig. 3(b). The latter approach is more practical, as it avoids the restriction of working at a set magnetic field strength and alignment angle [30,31]. Simultaneous excitation of all three hyperfine transitions is carried out by mixing the modulated driving frequency with a sine wave oscillating at a frequency equal to the axial hyperfine constant $A_\parallel = 2.16$ MHz (the splitting of the three hyperfine lines), which results in the spectrum shown

in Fig. 3(a)(iii). The resulting slopes in Fig. 3(a)(iii) are approximately 2–2.5 times the slopes generated from the single-frequency modulated signal, as can be seen in Fig. 3(c), with further enhancement dependent on the optimization of the modulation depth, and the Γ_p/Ω ratio which judges the degree of linewidth narrowing brought about.

Both CW and lock-in spectra can be simulated using the steady-state solution of a five-level Bloch equation [32], set up with the rates reported in Ref. [33]. An analytical expression is defined in terms of the steady-state solutions of the excited-state populations $\mathcal{I}_{\mathrm{CW}}$ as a function of Γ_p, Ω, and the detuning of the drive frequency $\omega_c/2\pi$ relative to the peak resonance frequency $\omega_0/2\pi$ [28]. For the three hyperfine lines, the expression can be defined as a sum of three Lorentzian distributions:

$$\mathcal{S}_{\mathrm{CW}}(\omega_c) = \sum_{m_I=\{-1,0,1\}} V_0\left(\frac{(\mathcal{I}_{\mathrm{CW}}^{\Omega=0} - \mathcal{I}_{\mathrm{CW}}^{\Delta=0})\gamma^2}{\Delta^2+\gamma^2}\right), \quad (1)$$

where V_0 is the off-resonance detected voltage, m_I is the nuclear spin quantum number, γ is the half width at half maximum, and the detuning is expressed through $\Delta = (\omega_c - \omega_0) + 2\pi m_I A_{\parallel}$. This expression includes the influence of both power broadening and linewidth narrowing through $\mathcal{I}_{\mathrm{CW}}$, providing a basis to define the lock-in equivalent signal, which is a product of a cosine reference signal $\mathcal{S}_{\mathrm{ref}} = \cos(2\pi\nu t)$ and a detected signal, both modulated at a reference frequency ν. The modulation of $\omega_c/2\pi$ is carried out at the same frequency ν with a modulation depth m using a sine-wave function, resulting in a modulation index $\beta = m/\nu$. The ODMR spectrum $\mathcal{S}_{\mathrm{CW}}$ becomes a function of

$$\omega(t) = \sum_{n=-\infty}^{\infty} J_n(\beta)\sin(\omega_c t + n\nu 2\pi t), \quad (2)$$

where J_n is a Bessel function of the first kind of order n [28]. Assuming that the reference and modulated signals are perfectly in phase, the expression for the lock-in signal takes the form of

$$\mathcal{S}_{\mathrm{LI}}(\omega_c) = \mathcal{A}V_0\mathcal{S}_{\mathrm{CW}}(\omega(t))\mathcal{S}_{\mathrm{ref}}, \quad (3)$$

where a lock-in voltage prefactor $\mathcal{A} \propto 10g$ is proportional to the lock-in amplifier gain factor g. For $\beta > 1$, the power spectrum of Eq. (2) shows approximately $n \simeq \lceil\beta\rceil$ significant peaks which possess an amplitude that is at least 1% of the central unmodulated carrier frequency [34]. Using this picture, expression (3) becomes equivalent to the sum of two sets of $n/2$ out-of-phase spectra, each driven by an Ω scaled by a Bessel function $J_n{}^*(\beta)$ which has been normalized with respect to the maximum amplitude of the calculated frequency spectrum (obtained using Eq. (2)):

$$\mathcal{S}_{\mathrm{LI}} \simeq \frac{\mathcal{A}V_0}{2}\sum_{n=0}^{\lceil\beta/2\rceil}(\mathcal{S}_{\mathrm{CW}}[\omega_c + n\nu 2\pi, |J_n{}^*(\beta)\Omega|] - \mathcal{S}_{\mathrm{CW}}[\omega_c - n\nu 2\pi, |J_n{}^*(\beta)\Omega|]). \quad (4)$$

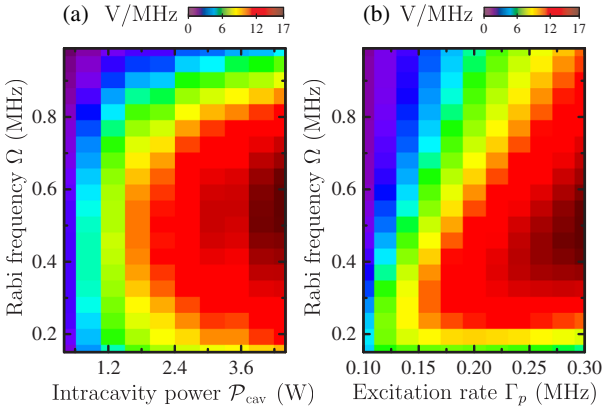

FIG. 4. (a) Measured $\max\{d_\omega\mathcal{S}_{\mathrm{LI}}\}$ for $\omega_c = \omega_0$ as a function of Ω and Γ_p. (b) Simulated comparison of the plot in (a) using Eq. (4) and identical experimental parameters of $\mathcal{A} = 5\times10^4$, $T_1 \sim 5.5$ ms, $T_2^* \sim 0.4$ μs, and $m = 0.5$ MHz.

A generated spectrum using Eq. (4) is fitted to a measured spectrum in Fig. 3(c), showing excellent agreement.

With an optimized m, ν, and drive frequency composition, exploration of the trend of $\max\{d_\omega\mathcal{S}_{\mathrm{LI}}\}$ with varying Γ_p's and Ω's is carried out for a fixed lock-in gain and time constant. The measured points are plotted in Fig. 4(a). Using the equivalent experimental lock-in gain settings (giving a prefactor of $g = 5\times10^3$), coherence times obtained through pulsed measurements, and decay rates inferred from Ref. [33], a simulated comparison is shown in Fig. 4(b), using Eq. (4) and the five-level model summarized in the Supplemental Material [28]. Both measured and simulated trends indicate an Ω-dependent maximum, while there is a general increase with Γ_p. Specifically, the increase in Γ_p is seen to offset the degradation of $\max\{d_\omega\mathcal{S}_{\mathrm{LI}}\}$ associated with power broadening when Ω increases. Essentially, this is the linewidth-narrowing effect [24,35], where the onset of power broadening is counteracted by the increased depletion rate of $^3A_2$. This mechanism is accentuated by adjusting the Γ_p/Ω ratio, which leads to obtaining an optimum $\max\{d_\omega\mathcal{S}_{\mathrm{CW}}\}$. This regime is reached by virtue of the cavity enhancement, allowing for the necessary Γ_p for the large ensemble volume to be achieved. The Ω values used for the simulation match the experimentally verified parameters, while the excitation rate is found to obey the relationship $\Gamma_p \simeq (\varepsilon/4)\mathcal{P}_{\mathrm{cav}}$. Although the trend correspondence is not perfectly identical in this part of the parameter space, the similarity of the occurrence and position of a minimum and the slope values points towards the validity of expression (4).

A projection of the maximum-attainable sensitivity can be calculated assuming detection is limited solely by the lock-in input noise and the detected shot noise. The projected sensitivity can be estimated from the ratio of the electronic noise level and the point in the spectrum where the fastest rate of fluorescence change occurs when

a magnetic field is applied, i.e., the point of maximum slope $\max\{d_\omega \mathcal{S}_{\mathrm{LI}}\}$. Considering an ensemble of 10^9 emitters and a collection efficiency of 2%, the shot-noise level is calculated to be approximately 58 $\mathrm{nV}/\sqrt{\mathrm{Hz}}$. Using the estimated lock-in input noise and detector load-generated noise (approximately 7 $\mathrm{nV}/\sqrt{\mathrm{Hz}}$ and 13 $\mathrm{nV}/\sqrt{\mathrm{Hz}}$, respectively), along with the previously stated gain setting $\mathcal{A} = 5 \times 10^4$ and the coherence times for the measurements in Fig. 4(a), a maximum projected sensitivity is calculated as

$$\delta B = \frac{\mathcal{A}(80\mathrm{nV}/\sqrt{\mathrm{Hz}})}{\max\{d_\omega \mathcal{S}_{\mathrm{LI}}\}\gamma_e} \sim 160\ \mathrm{pT}/\sqrt{\mathrm{Hz}} \tag{5}$$

for $\Omega = 5.7$ MHz and $\Gamma_p = 6$ MHz, which corresponds to a cavity input power of $\mathcal{P}_{\mathrm{in}} = 1.1$ W. While δB should scale inversely with the square root of the number of N-V centers, the measured absorption fraction and simulations indicate that the expected excitation power needed to optimize $\max\{d_\omega \mathcal{S}_{\mathrm{LI}}\}$ is strongly nonlinear with respect to the number of emitters. While the actual increase in excitation power will depend on how exactly the N-V densities are increased and the resulting ratio between N-V centers and other absorbing impurities, this suggests that increasing ensemble densities to maximize sensitivities may not be an optimal strategy, as the power required to optimize $\max\{d_\omega \mathcal{S}_{\mathrm{LI}}\}$ may be difficult to experimentally maintain. Instead, further improvement of the collection efficiencies and detection electronics (in terms of photodetector responsiveness and low-noise preamplification) would be more practically realizable.

IV. ENHANCED MAGNETIC FIELD SENSING

Optimization of the lock-in modulation and excitation rates provides an optimally sensitive magnetic field probe, and by setting $\omega_c = \omega_0$ (the point of $\max\{d_\omega \mathcal{S}_{\mathrm{LI}}\}$), the presence of magnetic fields is observed through the change in the detected voltage, with a scaling inversely proportional to γ_e. Experimental assessment of the resulting sensitivity is carried out through both measuring the magnetic noise spectral density, as well as generating a weak oscillating field close to the diamond, the results of which are summarized in Fig. 5.

For the measurement of the spectral noise density, groups A and B are both assessed. With $\omega_c = \omega_0$, a time trace of 5×10^5 samples is recorded with a 2-kHz sampling rate, and the resulting sensitivity ($\mathrm{T}/\sqrt{\mathrm{Hz}}$) scaling of the trace's Fourier transform is obtained. This measurement is also carried out for a MW excitation that is off resonance ($\omega_c \gg \omega_0$) in an insensitive part of the spectrum. The resulting spectra in Fig. 5(a) show distinct spectral features resting on a approximately 200-$\mathrm{pT}/\sqrt{\mathrm{Hz}}$ noise floor for both groups A and B. Given the theoretically anticipated sensitivity calculated in the previous section, this value is deemed to be near-shot-noise limited for the current excitation parameters of $\Omega \sim 0.55$ MHz, and $\Gamma_p \sim 0.3$ MHz ($\mathcal{P}_{\mathrm{in}} \sim 0.4$ W). Low frequency (dc to 5-Hz) noise is attributed to the slow, temperature-dependent, fluctuating magnetization of the permanent magnet and to other residual magnetizations of surrounding metallic components. It is also affected by the temperature dependence of the N-V resonance frequency, which has a temperature-dependent zero-field splitting adding to the shifted spin resonances ω_0 by a factor of -74.2 kHz/K [36]. Group B is expected to be much more sensitive to such low-frequency magnetic noise due to the three subgroups possessing different relative projection angles, and it therefore displays a higher noise density below 5 Hz. Towards higher frequencies, there is a characteristic first-order filter roll-off (-20 dB/decade) which occurs after the cutoff frequency at 159 Hz. Most noteworthy is the detection of the 50-Hz magnetic mains "hum" and its subsequent odd harmonics, shown to be detectable only when the MW is on resonance. Detection of 50 Hz and its second odd harmonic for both groups are shown in Figs. 5(a)(i) and 5(a)(ii), subject to the characteristic dampening of the low-pass filter. For comparison, the noise spectra generated from the lock-in amplifier at its lowest gain setting with the connected blocked detector is also plotted, with a similar sensitivity scaling as for group A. This represents the cumulative noise floor limit of the current configuration, which may be overcome by further enhancing $\max\{d_\omega \mathcal{S}_{\mathrm{LI}}\}$ (i.e., via changing the linewidth-to-contrast ratio) and increasing the light collection efficiency.

Further investigation of the system's noise characteristics is carried out by calculating the Allan deviation of the time traces used to calculate the noise spectra in Fig. 5(a). Using the color designation in Fig. 5(a), the Allan deviations are plotted in Fig. 5(b) in units of T. The Allan deviation is a measure of the standard deviation as a function of sample binning size and is commonly used, in conjunction with the spectral noise density, to study and identify the presence of systematic and stochastic noise in oscillatory systems [37]. The slopes and features of the obtained trend highlight the type of noise present and their limits on the optimal averaging time. In the calculated Allan plots, the most striking feature is the clear difference in behavior between the on- and off-resonance traces. The off-resonance traces exhibits a constant $\tau^{-1/2}$ scaling, which signifies the dominance of stochastic white noise, as expected from thermally induced electronic noise generated in the detector and lock-in amplifier components. Both on-resonance traces also show the same trend dressed with the systematic noise originating from the 50-Hz hum, but they reach slightly different minimum τ's of approximately 4 nT at 0.4 s and about 6 nT at 0.2 s for A and B, respectively. Group B displays a higher Allan deviation on a slightly shorter time scale, believed to be due to the increased sensitivity of three groups maintaining degeneracy, and the larger intrinsic magnetic noise inherent to the denser

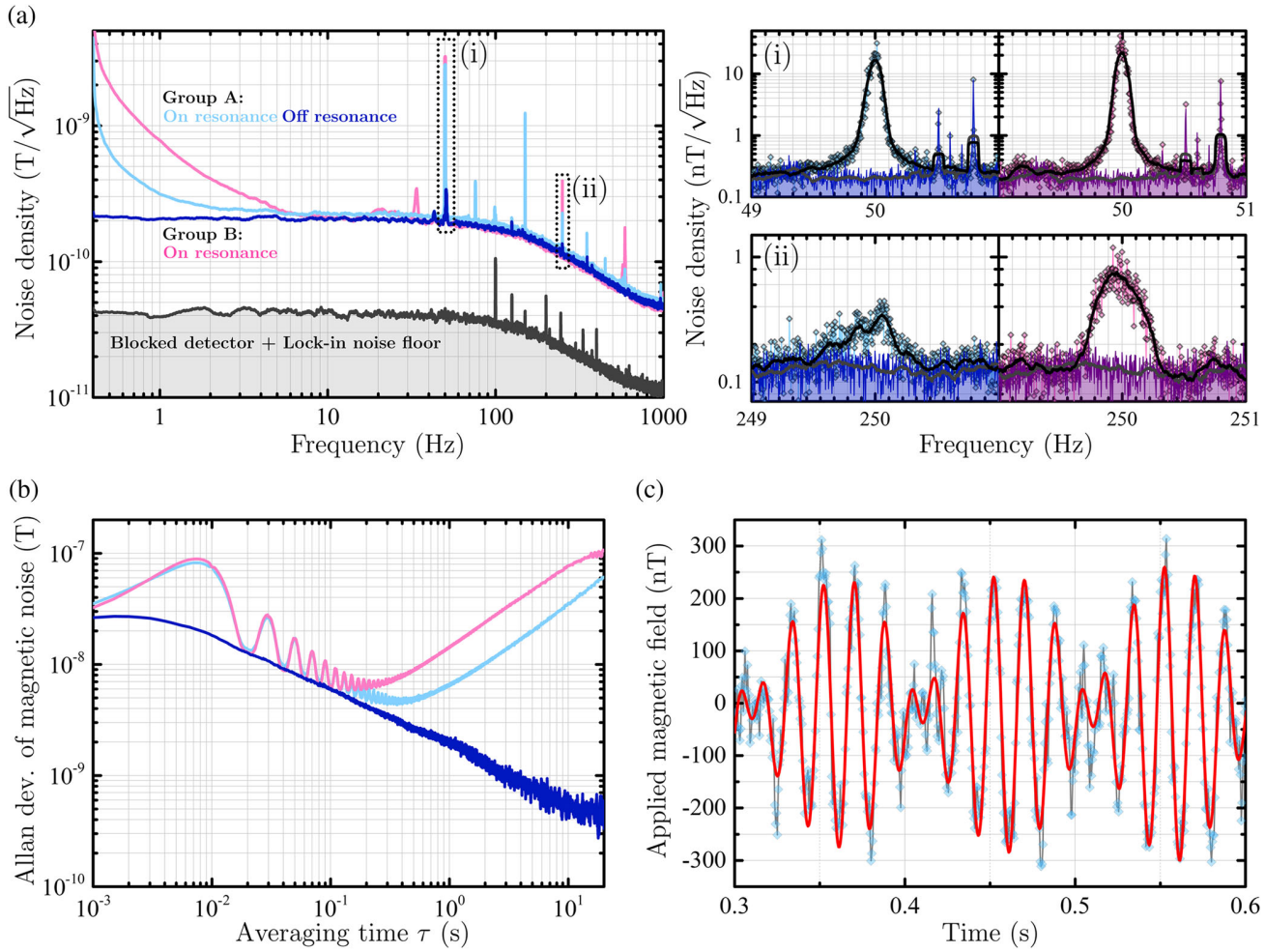

FIG. 5. (a) Plots of the magnetic noise spectral density when on resonance ($\omega_c = \omega_0$) and off resonance ($\omega_c \gg \omega_0$), for both groups A and B with $\Omega \sim 0.55$ MHz and $\Gamma_p \sim 0.3$ MHz ($\mathcal{P}_{\text{in}} \sim 0.4$ W). The combined noise floor of the lock-in and detector for the lowest lock-in gain settings, assuming a similar $\max\{d_\omega \mathcal{S}_{\text{LI}}\}$ to that of A, is also plotted. The plots are averaged from five subsequently measured frequency traces and are smoothed using a Savitzky-Golay filter. Magnified plots of the peaks designated (i) and (ii) show unsmoothed data points with the smoothed traces, highlighting the detection and lack of detection of the 50-Hz magnetic hum and its second odd harmonic when on or off resonance. The difference in amplitude are attributed to varying laboratory conditions. (b) Plots of the Allan deviation of the traces in (a) using an identical color designation. The trends show drops scaling with $\tau^{-1/2}$ highlighting the dominance of white noise in this regime, while the on-resonance plots are dressed with the systematic noise originating from the 50-Hz magnetic hum. A minimum floor for on-resonance detection is reached for $\tau = 0.2$–0.4 s, which signifies the limitation of electronic voltage noise ("flicker" noise), with further averaging (at large τ) giving no advantage. The subsequent increase highlights the dominance of long-term drift through thermal- and mechanical-based Brownian noise. The larger Allan deviation of group B is related to the fact the maintaining degeneracy is more noisy. (c) Time trace plot of the on-resonance response of group B to a generated 60-Hz magnetic ac field using the coil. The beating of the 60-Hz noise and the 50-Hz magnetic hum is made clear by the red trace, which is a guide for the eye.

ensemble of group B compared to group A. For longer averaging times, the minima are followed by an increase with a scaling that signifies the onset of long-term thermal drift, originating from, e.g., temperature-based magnetization fluctuations and the thermal expansion and displacement of surrounding metallic fixtures.

Finally, a weak ac magnetic field is applied to test the system response to more realistic measurement scenarios. A 60-Hz sine field is generated using the coil placed near the diamond holder, and a time trace is measured for group B, using all of the same measurement parameters applied for measuring the magnetic spectral noise density in Fig. 5(a). A portion of a recorded 250-s time trace is plotted in Fig. 5(c), which distinctly highlights beating between the generated 60-Hz field and the 50-Hz magnetic hum. Bearing in mind the Allan-deviation characteristics of the magnetometer shown in Fig. 5(b), estimating a single standard deviation of the measured trace would only be fair in the presence of a flat spectrum dominated by white noise. Instead, an Allan deviation of approximately 6 nT is

obtained for a sampling bin of 0.2 s from the total 250-s trace [a portion of which is shown Fig. 5(c)]. Accounting for the sampling-bin bandwidth, a directly extracted sensitivity of about 3 $\mathrm{nT}/\sqrt{\mathrm{Hz}}$ is calculated. This value is larger then the measured noise density floor due to the presence of the low-frequency magnetic noise fluctuations from the environment and the magnetic coil itself. Through shielding of the environment and stabilization of the magnetic coils current source, this measured value is expected to approach the noise floor of approximately 200 $\mathrm{pT}/\sqrt{\mathrm{Hz}}$.

V. CONCLUSION AND OUTLOOK

This work demonstrates how amplifying the pump field in combination with a microwave resonator antenna and lock-in detection can reach a near-shot-noise-limited noise floor using an off-the-shelf CVD diamond with no additional modification and unoptimized fluorescence collection. The use of the confocal cavity brings about excitation across a volume of approximately 3.5×10^{-2} mm^3, with an estimated magnitude of about 10^9 N-V centers, allowing for a nonlinear fluorescence excitation regime to be reached. Reaching this excitation regime was crucial for bringing about linewidth narrowing and thereby maximizing the measured lock-in slope, in combination with simultaneously exciting all three hyperfine frequencies. The enhanced sensitivity of the signal allows for the measurement of an approximately 200-$\mathrm{pT}\sqrt{\mathrm{Hz}}$ noise floor for frequencies ranging from 0.1 to 159 Hz (limited by the time constant set by the lock-in amplifier), and the measurement of an applied 60-Hz magnetic field with an extracted sensitivity of about 3 $\mathrm{nT}/\sqrt{\mathrm{Hz}}$ which is limited by the environmental magnetic noise. Compared to the projected calculated sensitivity of approximately 160 $\mathrm{pT}\sqrt{\mathrm{Hz}}$ that is achievable with the estimated number of N-V centers, the measured noise floor is assumed to be near-shot-noise limited.

This work shows the importance of enhancing the efficiency and uniformity of excitation and spin polarization, with measured near-dc sensitivities comparable to those reported in the literature that are based on using denser N-V ensembles. Furthermore, it indicates that an increased ensemble density may necessitate significantly larger excitation powers to optimize their collective sensitivity. While this statement may be obvious, these results suggest that the needed power may be impractical from an application point of view, even if N-V absorption is the dominant absorption source.

ACKNOWLEDGMENTS

We would like to thank Kristian Hagsted Rasmussen for help with diamond surface preparation and Ilya Radko for supporting N-V concentration measurements. We are also thankful to Fedor Jelezko, Adam Wojciechowski, and Ilja Gerhardt for helpful discussions. This work is partly funded by Innovation Fund Denmark under the EXMAD project and the Qubiz center, as well as the Danish research Council under the DIMS project.

S. A. and H. A. R. E.-E. contributed equally to this work.

[1] L. Rondin, J. P. Tetienne, T. Hingant, J. F. Roch, P. Maletinsky, and V. Jacques, Magnetometry with nitrogen-vacancy defects in diamond, Rep. Prog. Phys. **77**, 056503 (2014).

[2] G. Kucsko, P. C. Maurer, N. Y. Yao, M. Kubo, H. J. Noh, P. K. Lo, H. Park, and M. D. Lukin, Nanometre-scale thermometry in a living cell, Nature (London) **500**, 54 (2013).

[3] P. Neumann, I. Jakobi, F. Dolde, C. Burk, R. Reuter, G. Waldherr, J. Honert, T. Wolf, A. Brunner, J. H. Shim, D. Suter, H. Sumiya, J. Isoya, and J. Wrachtrup, High-precision nanoscale temperature sensing using single defects in diamond, Nano Lett. **13**, 2738 (2013).

[4] F. Dolde, H. Fedder, M. W. Doherty, T. Nöbauer, F. Rempp, G. Balasubramanian, T. Wolf, F. Reinhard, L. C. L. Hollenberg, F. Jelezko, and J. Wrachtrup, Electric-field sensing using single diamond spins, Nat. Phys. **7**, 459 (2011).

[5] D. R. Glenn, K. Lee, H. Park, R. Weissleder, A. Yacoby, M. D. Lukin, H. Lee, R. L. Walsworth, and C. B. Connolly, Single-cell magnetic imaging using a quantum diamond microscope, Nat. Methods **12**, 736 (2015).

[6] G. Balasubramanian, I. Y. Chan, R. Kolesov, M. Al-Hmoud, J. Tisler, C. Shin, C. Kim, A. Wojcik, P. R. Hemmer, A. Krueger, T. Hanke, A. Leitenstorfer, R. Bratschitsch, F. Jelezko, and J. Wrachtrup, Nanoscale imaging magnetometry with diamond spins under ambient conditions, Nature (London) **455**, 648 (2008).

[7] L. T. Hall, G. C. G. Beart, E. A. Thomas, D. A. Simpson, L. P. McGuinness, J. H. Cole, J. H. Manton, R. E. Scholten, F. Jelezko, J. Wrachtrup, S. Petrou, and L. C. L. Hollenberg, High spatial and temporal resolution wide-field imaging of neuron activity using quantum NV-diamond, Sci. Rep. **2**, 401 (2012).

[8] J. M. Taylor, P. Cappellaro, L. Childress, L. Jiang, D. Budker, P. R. Hemmer, A. Yacoby, R. Walsworth, and M. D. Lukin, High-sensitivity diamond magnetometer with nanoscale resolution, Nat. Phys. **4**, 810 (2008).

[9] Romana Schirhagl, Kevin Chang, Michael Loretz, and Christian L. Degen, Nitrogen-vacancy centers in diamond: Nanoscale sensors for physics and biology, Annu. Rev. Phys. Chem. **65**, 83 (2014).

[10] N. Y. Yao, L. Jiang, A. V. Gorshkov, P. C. Maurer, G. Giedke, J. I. Cirac, and M. D. Lukin, Scalable architecture for a room temperature solid-state quantum information processor, Nat. Commun. **3**, 800 (2012).

[11] D. Arnold, S. Siegel, E. Grisanti, J. Wrachtrup, and I. Gerhardt, A rubidium M_x-magnetometer for measurements on solid state spins, Rev. Sci. Instrum. **88**, 023103 (2017).

[12] J. F. Barry, M. J. Turner, J. M. Schloss, D. R. Glenn, Y. Song, M. D. Lukin, H. Park, and R. L. Walsworth, Optical magnetic detection of single-neuron action potentials using quantum defects in diamond, Proc. Natl. Acad. Sci. U.S.A. **113**, 14133 (2016).

[13] H. Clevenson, M. E. Trusheim, T. Schroder, C. Teale, D. Braje, and D. Englund, Broadband magnetometry and temperature sensing with a light trapping diamond waveguide, Nat. Phys. **11**, 393 (2015).

[14] D. Le Sage, L. M. Pham, N. Bar-Gill, C. Belthangady, M. D. Lukin, A. Yacoby, and R. L. Walsworth, Efficient photon detection from color centers in a diamond optical waveguide, Phys. Rev. B **85**, 121202 (2012).

[15] T. Wolf, P. Neumann, K. Nakamura, H. Sumiya, T. Ohshima, J. Isoya, and J. Wrachtrup, Subpicotesla Diamond Magnetometry, Phys. Rev. X **5**, 041001 (2015).

[16] V. M. Acosta, E. Bauch, M. P. Ledbetter, C. Santori, K.-M. C. Fu, P. E. Barclay, R. G. Beausoleil, H. Linget, J. F. Roch, F. Treussart, S. Chemerisov, W. Gawlik, and D. Budker, Diamonds with a high density of nitrogen-vacancy centers for magnetometry applications, Phys. Rev. B **80**, 115202 (2009).

[17] G. Balasubramanian, P. Neumann, D. Twitchen, M. Markham, R. Kolesov, N. Mizuochi, J. Isoya, J. Achard, J. Beck, J. Tissler, V. Jacques, P. R. Hemmer, F. Jelezko, and J. Wrachtrup, Ultralong spin coherence time in isotopically engineered diamond, Nat. Mater. **8**, 383 (2009).

[18] P. Siyushev, F. Kaiser, V. Jacques, I. Gerhardt, S. Bischof, H. Fedder, J. Dodson, M. Markham, D. Twitchen, F. Jelezko, and J. Wrachtrup, Monolithic diamond optics for single photon detection, Appl. Phys. Lett. **97**, 241902 (2010).

[19] J. P. Hadden, J. P. Harrison, A. C. Stanley-Clarke, L. Marseglia, Y. L. D. Ho, B. R. Patton, J. L. O'Brien, and J. G. Rarity, Strongly enhanced photon collection from diamond defect centers under microfabricated integrated solid immersion lenses, Appl. Phys. Lett. **97**, 241901 (2010).

[20] B. J. M. Hausmann, B. J. Shields, Q. Quan, Y. Chu, N. P. De Leon, R. Evans, M. J. Burek, A. S. Zibrov, M. Markham, D. J. Twitchen, H. Park, M. D. Lukin, and M. Loncr, Coupling of NV centers to photonic crystal nanobeams in diamond, Nano Lett. **13**, 5791 (2013).

[21] D. Riedel, D. Rohner, M. Ganzhorn, T. Kaldewey, P. Appel, E. Neu, R. J. Warburton, and P. Maletinsky, Low-Loss Broadband Antenna for Efficient Photon Collection from a Coherent Spin in Diamond, Phys. Rev. Applied **2**, 064011 (2014).

[22] Y. Dumeige, M. Chipaux, V. Jacques, F. Treussart, J. F. Roch, T. Debuisschert, V. M. Acosta, A. Jarmola, K. Jensen, P. Kehayias, and D. Budker, Magnetometry with nitrogen-vacancy ensembles in diamond based on infrared absorption in a doubly resonant optical cavity, Phys. Rev. B **87**, 155202 (2013).

[23] K. Jensen, N. Leefer, A. Jarmola, Y. Dumeige, V. M. Acosta, P. Kehayias, B. Patton, and D. Budker, Cavity-Enhanced Room-Temperature Magnetometry Using Absorption by Nitrogen-Vacancy Centers in Diamond, Phys. Rev. Lett. **112**, 160802 (2014).

[24] K. Jensen, V. M. Acosta, A. Jarmola, and D. Budker, Light narrowing of magnetic resonances in ensembles of nitrogen-vacancy centers in diamond, Phys. Rev. B **87**, 014115 (2013).

[25] N. Aslam, G. Waldherr, P. Neumann, F. Jelezko, and J. Wrachtrup, Photo-induced ionization dynamics of the nitrogen vacancy defect in diamond investigated by single-shot charge state detection, New J. Phys. **15**, 013064 (2013).

[26] R. U. A. Khan, B. L. Cann, P. M. Martineau, J. Samartseva, J. J. P. Freeth, S. J. Sibley, C. B. Hartland, M. E. Newton, H. K. Dhillon, and D. J. Twitchen, Colour-causing defects and their related optoelectronic transitions in single crystal CVD diamond, J. Phys. Condens. Matter **25**, 275801 (2013).

[27] T.-L. Wee, Y.-K. Tzeng, C.-C. Han, H.-C. Chang, W. Fann, J.-H. Hsu, K.-M. Chen, and Y.-C. Yu, Two-photon excited fluorescence of nitrogen-vacancy centers in proton-irradiated type Ib diamond, J. Phys. Chem. A **111**, 9379 (2007).

[28] See Supplemental Material at http://link.aps.org/supplemental/10.1103/PhysRevApplied.8.034001 for a wide-span measurement of the mixed MW signal, a description of the Bloch equations, its steady-state solution, and a derivation of the Fourier series for a frequency-modulated wave using a sine function.

[29] P. L. Stanwix, L. M. Pham, J. R. Maze, D. Le Sage, T. K. Yeung, P. Cappellaro, P. R. Hemmer, A. Yacoby, M. D. Lukin, and R. L. Walsworth, Coherence of nitrogen-vacancy electronic spin ensembles in diamond, Phys. Rev. B **82**, 201201(R) (2010).

[30] R. Fischer, A. Jarmola, P. Kehayias, and D. Budker, Optical polarization of nuclear ensembles in diamond, Phys. Rev. B **87**, 125207 (2013).

[31] A. Wickenbrock, H. Zheng, L. Bougas, N. Leefer, S. Afach, A. Jarmola, V. M. Acosta, and D. Budker, Microwave-free magnetometry with nitrogen-vacancy centers in diamond, Appl. Phys. Lett. **109**, 053505 (2016).

[32] H. A. R. El-Ella, S. Ahmadi, A. Wojciechowski, A. Huck, and U. L. Andersen, Optimised frequency modulation for continuous-wave optical magnetic resonance sensing using nitrogen-vacancy ensembles, Opt. Express **25**, 14809 (2017).

[33] L. Robledo, H. Bernien, T. van der Sar, and R. Hanson, Spin dynamics in the optical cycle of single nitrogen-vacancy centres in diamond, New J. Phys. **13**, 025013 (2011).

[34] J. R. Carson, Notes on the theory of modulation, Proc. IRE **10**, 57 (1922).

[35] A. Dréau, M. Lesik, L. Rondin, P. Spinicelli, O. Arcizet, J.-F. Roch, and V. Jacques, Avoiding power broadening in optically detected magnetic resonance of single NV defects for enhanced dc magnetic field sensitivity, Phys. Rev. B **84**, 195204 (2011).

[36] V. M. Acosta, E. Bauch, M. P. Ledbetter, A. Waxman, L.-S. Bouchard, and D. Budker, Temperature Dependence of the Nitrogen-Vacancy Magnetic Resonance in Diamond, Phys. Rev. Lett. **104**, 070801 (2010).

[37] D. W. Allan, Should the classical variance be used as a basic measure in standards metrology?, IEEE Trans. Instrum. Meas. **IM-36**, 646 (1987).

Supplementary for "Pump Enhanced Continuous-Wave Magnetometry using Nitrogen-Vacancy Ensembles"

Sepehr Ahmadi, Haitham A.R. El-Ella,* Jørn O. B. Hansen, Alexander Huck, and Ulrik L. Andersen
Department of Physics, Technical University of Denmark, 2800 Kongens Lyngby, Denmark

Appendix A: Fluorescence Signal Prior to Lock-in Detection, and Full Microwave Excitation Spectrum

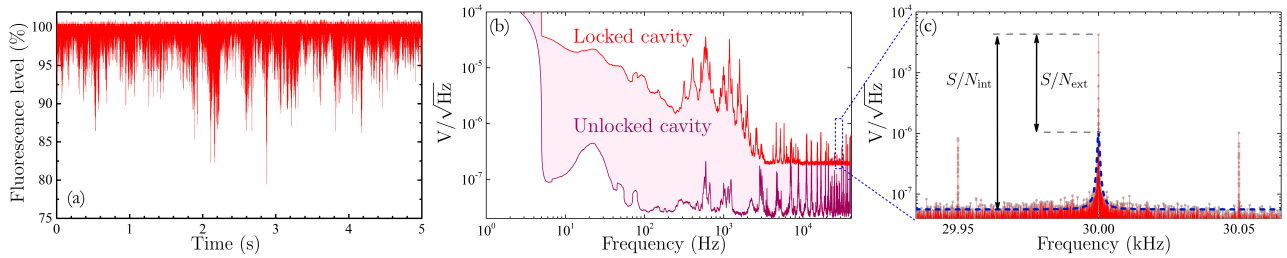

FIG. 1. (a) Time-dependent NV fluorescence measured before the lock-in amplifier, with $\omega_c = \omega_0$ and modulated at 30 kHz. The fluorescence is scaled relative to the maximum measured fluorescence when the cavity is locked. (b) Smoothed Fourier transform of (a) highlighting significant RMS noise up to 3 kHz after which the noise floor reaches a plateau. (c) Zoom in of the 30 kHz frequency component (not smoothed) displaying an intrinsic signal to noise ratio of $S/N_{\rm int} \sim 750$, and an extrinsic signal to noise ratio $S/N_{\rm ext} \sim 40$. $S/N_{\rm ext}$ is extracted by fitting the wings of the central carrier frequency with a Lorentzian. Two side-bands at 50 Hz originate from the beating of the central carrier with the 50 Hz magnetic hum.

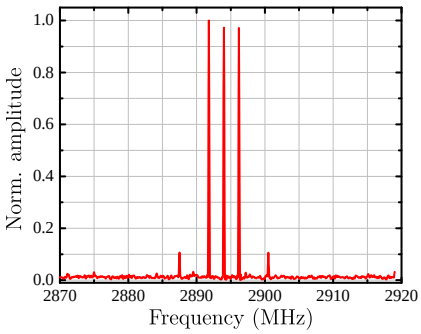

FIG. 2. Measured wide span spectrum of the carrier wave ω_c mixed with a signal at the hyperfine splitting frequency $A_\parallel = 2.16$ MHz.

The detected signal prior to lock-in amplification is shown in supplementary figure 1(a), highlighting the effect of the cavity servo on the diamond fluorescence while maintaining its lock. As seen in 6(b), the process of locking the cavity, in addition to the environmental perturbations of the cavity mirrors and the increased shot-noise raises the noise floor and introduces significant noise density up to 3 kHz, before settling. For these reasons, lock-in detection using modulation frequencies past 3 kHz helps to circumvent the inherent noise density of the locked-cavity system. Furthermore, the modulated ODMR signal (here generated by setting $\omega_c = \omega_0$ + the half width at half maximum) posses a low signal to noise ratio, which benefits greatly from phase-sensitive amplification. This is shown in the magnified window around 30 kHz in figure 6(c), where the 30 kHz peak shows an intrinsic signal-to-noise ratio (limited by the intrinsic properties of the diamond) of $S/N_{\rm int} \sim 750$, and an extrinsic signal to noise ratio (limited

* haitham.el@fysik.dtu.dk

by the noise from external field fluctuations) of $S/N_{\rm ext} \sim 40$. The intrinsic signal-to-noise ratio limits the smallest delectable field δB to ~ 20 nT. The beating of the central carrier with the 50 Hz magnetic hum is also apparent from the 50 Hz separated side-bands.

The full excitation spectrum of the mixed carrier frequency is shown in supplementary figure 2 prior to amplification, showing an absence of harmonics beyond the first order, as well as the relative power of the first order harmonics to the central mixed frequencies.

Appendix B: Derivation of Expressions for Continuous-Wave and Lock-in ODMR Spectrum

A system of coupled rate equations for a five-level scheme (detailed in supplementary figure 3) is constructed to model the ODMR spectrum dependence on the essential decay rates and the optical pump and MW drive. This is used to be able to more accurately model the expected lock-in signal, in order to project the optimum limit of this measurement technique and thereby better understand the limitations of the current system. The coupled equations are derived using a Hamiltonian that only incorporates the resonant drive between the two ground-spin states:

$$\hat{\mathcal{H}}/\hbar = \sum \omega_i |i\rangle\langle i| - \Omega \cos(\omega t)\big(|1\rangle\langle 2| + |2\rangle\langle 1|\big). \tag{B1}$$

Using a rotating reference frame with the MW drive frequency $\omega_c/2\pi$ and the rotating-wave approximation, the system of equations become:

$$\dot{\rho}_{11} = -\Gamma_p\rho_{11} + k_{31}\rho_{33} + k_{41}\rho_{44} + k_{51}\rho_{55} - \frac{k_{21}}{2}(\rho_{11}-\rho_{22}) - \frac{i}{2}\Omega(\rho_{12}-\rho_{21}), \tag{B2}$$

$$\dot{\rho}_{22} = -\Gamma_p\rho_{22} + k_{32}\rho_{33} + k_{42}\rho_{44} + k_{52}\rho_{55} - \frac{k_{21}}{2}(\rho_{22}-\rho_{11}) + \frac{i}{2}\Omega(\rho_{12}-\rho_{21}), \tag{B3}$$

$$\dot{\rho}_{33} = \Gamma_p\rho_{11} - (k_{35}+k_{32}+k_{31})\rho_{33}, \tag{B4}$$

$$\dot{\rho}_{44} = \Gamma_p\rho_{22} - (k_{45}+k_{42}+k_{41})\rho_{44}, \tag{B5}$$

$$\dot{\rho}_{55} = k_{45}\rho_{44} + k_{35}\rho_{33} - (k_{52}+k_{51})\rho_{55}, \tag{B6}$$

$$\dot{\rho}_{12} = -(\gamma_2' - i\Delta)\rho_{12} + \frac{i}{2}\Omega(\rho_{22}-\rho_{11}), \tag{B7}$$

$$\dot{\rho}_{21} = -(\gamma_2' + i\Delta)\rho_{21} - \frac{i}{2}\Omega(\rho_{22}-\rho_{11}), \tag{B8}$$

where $\Delta = (\omega_c - \omega_0)$ is the detuning between the MW frequency $\omega_c/2\pi$ and the ground-spin state transition frequency $\omega_0/2\pi$, while the spin and optical dephasing rates are defined through $\gamma_2 = k_{21}/2 + \gamma_2^*$ and $\gamma_2' = \gamma_2 + \Gamma_p/2$, respectively, and $\mathrm{Tr}\{\hat{\rho}\} = 1$. The steady-state solutions for the ground state populations become:

$$\rho_{11}^{ss} = \left[1 + \Xi + \frac{\Gamma_p}{K_3} + \frac{\Gamma_p\Xi}{K_4} + \frac{k_{35}\Gamma_p}{K_3K_5} + \frac{k_{45}\Gamma_p\Xi}{K_5K_4}\right]^{-1}, \quad \rho_{22}^{ss} = \left[1 + \frac{1}{\Xi} + \frac{\Gamma_p}{K_4} + \frac{\Gamma_p}{K_3\Xi} + \frac{k_{45}\Gamma_p}{K_4K_5} + \frac{k_{35}\Gamma_p}{K_5K_3\Xi}\right]^{-1}, \tag{B9}$$

$$\Xi = \frac{\left[\left(\frac{k_{21}}{2}\right) + \left(\frac{\Gamma_p(k_{32}K_5 + k_{52}k_{35})}{K_3K_5}\right) + \left(\frac{\Omega^2\gamma_2'}{2(\gamma_2'^2+\Delta^2)}\right)\right]}{\left[\Gamma_p + \left(\frac{k_{21}}{2}\right) - \left(\frac{\Gamma_p(k_{42}K_5 + k_{52}k_{45})}{K_4K_5}\right) + \left(\frac{\Omega^2\gamma_2'}{2(\gamma_2'^2+\Delta^2)}\right)\right]}, \tag{B10}$$

where:

$$K_3 = k_{31} + k_{32} + k_{35}, \quad K_4 = k_{41} + k_{42} + k_{45}, \quad K_5 = k_{51} + k_{52}. \tag{B11}$$

The ODMR spectrum is then defined in terms of the excited levels steady-state populations, which are proportional to the ground sate steady-state populations:

$$\mathcal{I}_{cw} = \alpha\rho_{33}^{ss} + \beta\rho_{44}^{ss} = \frac{\alpha\Gamma_p}{K_3}\rho_{11}^{ss} + \frac{\beta\Gamma_p}{K_4}\rho_{22}^{ss}, \tag{B12}$$

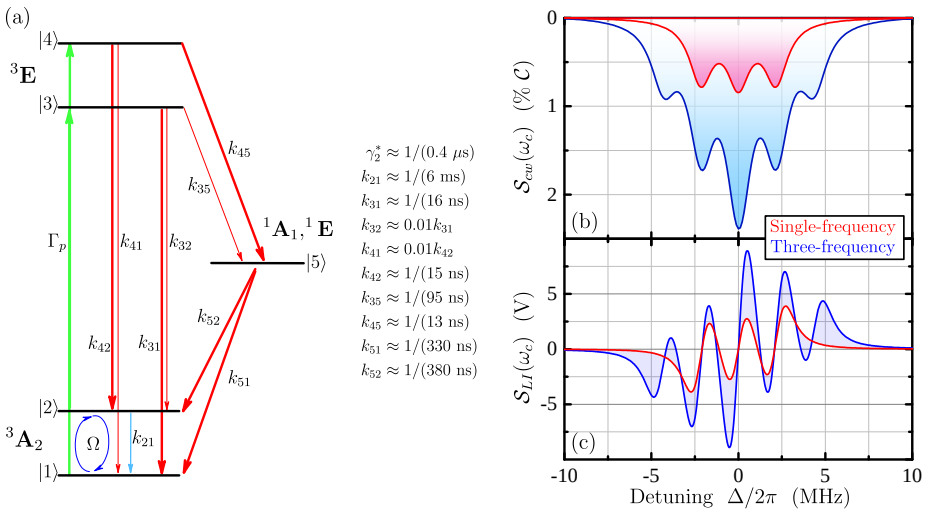

FIG. 3. (a)Schematic of the 5-level structure used to model ensemble NV transitions, where only the $|m_s = +1\rangle$ spin level is considered for state $|2\rangle$ and $|4\rangle$, while the shelving states are merged into a single level $|5\rangle$. The listed decay rate values were extracted from [1]. (b) Plot of equation B15 for both single- and three-frequency excitation, with the axis shown in terms of the contrast $\mathcal{C}$, with $\Gamma_p = 0.3/2\pi$ MHz and $\Omega/2\pi = 0.1$ MHz. (c) Single- and three-frequency excitation lock-in signals plotted for the simulated spectra in (b) using equations B22 and B23.

where the pre-factors are functions of the fraction of the radiative relaxation rates:

$$\alpha = \frac{k_{31} + k_{32}}{K_3} \ , \ \beta = \frac{k_{41} + k_{42}}{K_4}. \tag{B13}$$

As a function of detuning, the expression (B12) (plotted in figure 3(b)) is equivalent to a Lorentzian function:

$$\mathcal{S}_{cw}(\omega_c) = \mathcal{I}_{cw}^{\Omega=0}\left(1 - \frac{\mathcal{C}\gamma^2}{\Delta^2 + \gamma^2}\right) \equiv \frac{\alpha\Gamma_p}{K_3}\rho_{11}^{ss} + \frac{\beta\Gamma_p}{K_4}\rho_{22}^{ss}, \tag{B14}$$

where

$$\mathcal{C} = 1 - \frac{\mathcal{I}_{cw}^{\Delta=0}}{\mathcal{I}_{cw}^{\Omega=0}}, \quad 2\gamma \approx \gamma_2^* + \frac{1}{2\pi}\sqrt{\gamma_2^2 + \frac{\gamma_2\Omega^2}{k_{21} + \Gamma_p}}, \tag{B15}$$

for which $\mathcal{C}$ is the Ω/Γ_p-dependent contrast, $\mathcal{I}_{cw}^{\Omega=0}$ is the generated spectrum when $\Omega = 0$, and γ is the half width at half maximum. When attempting to model the resulting lock-in signal, the modulation function of $\omega_c/2\pi$ and its parameters needs to be considered. A sine-wave modulated field can be described through:

$$\omega(t) = \cos(\omega_c t + \beta\sin(2\pi\nu t)), \tag{B16}$$

where the modulation index $\beta = m/\nu$ is the ratio of the modulation depth m to the modulation frequency ν. Such a modulated signal possesses an infinite bandwidth, and to more intuitively account for its influence on the lock-in spectrum, this can be simplified by expanding the expression into its Fourier series coefficients, and then reducing it using the integral identity of the Bessel function:

$$\omega(t) = \mathrm{Re}\{e^{i\omega_c t}e^{i\beta\sin(2\pi\nu t)}\}, \tag{B17}$$

$$\omega(t) = \mathrm{Re}\left\{e^{i\omega_c t}\sum_{n=-\infty}^{\infty} C_n e^{in2\pi\nu t}\right\}, \quad C_n = \frac{1}{2\pi}\int_{-\pi}^{\pi} e^{i(\beta\sin(x) - nx)}dx = J_n(\beta), \quad \text{where } x = 2\pi\nu t, \tag{B18}$$

$$\omega(t) = \mathrm{Re}\left\{e^{i\omega_c t}\sum_{n=-\infty}^{\infty} J_n(\beta)e^{in2\pi\nu t}\right\} = \sum_{n=-\infty}^{\infty} J_n(\beta)\cos(\omega_c t + n2\pi\nu t). \tag{B19}$$

The spectrum can thus be described by n frequency components, spaced by ν and scaled by the Bessel function of the first kind $J_n(\beta)$. The number of frequency components whose amplitude constitutes at least 1% of the central un-modulated carrier frequency amplitude is well approximated as $n \simeq \lceil \beta \rceil$, for large β [2]. The modulated lock-in signal can then be defined in terms of the sum of $\lceil \beta/2 \rceil$ out-of-phase spectra equally spaced by ν, and driven by an Ω that is scaled by $|J_n^*(\beta)| = |J_n(\beta)/\chi|$ where χ is the largest Bessel function value generated from the set of $\lceil \beta \rceil$ peaks:

$$\mathcal{S}_{LI}(\omega_c) = \frac{\mathcal{A}V_0}{2} \sum_{n=0}^{\lceil \beta/2 \rceil} \Big(\mathcal{I}_{cw}(\Delta + n2\pi\nu, |J_n^*(\beta)\Omega|) - \mathcal{I}_{cw}(\Delta - n2\pi\nu, |J_n^*(\beta)\Omega|) \Big), \tag{B20}$$

where V_0 is the detected voltage prior to lock-in detection and $\mathcal{A} \propto 10g^{-1}$ is proportional to the lock-in gain factor g^{-1}. To describe the full spectrum, the expression is summed for three distributions shifted by the axial hyperfine constant $A_\parallel = 2.16$ MHz:

$$\mathcal{S}_{LI}(\omega_c) = \frac{\mathcal{A}V_0}{2} \sum_{m_I} \sum_{n=0}^{\lceil \beta/2 \rceil} \Big(\mathcal{I}_{cw}(\Delta + n2\pi\nu + m_I 2\pi A_\parallel, |J_n^*(\beta)\Omega|) - \mathcal{I}_{cw}(\Delta - n2\pi\nu + m_I 2\pi A_\parallel, |J_n^*(\beta)\Omega|) \Big), \tag{B21}$$

where $m_I = \{-1, 0, 1\}$ is the nuclear spin quantum number. In the case of simultaneous driving of all three hyperfine lines, expression (B21) becomes a further sum of the mixed $\omega_c/2\pi$ frequencies m_x $(= m_I)$ with $A_\parallel$:

$$\mathcal{S}_{LI}(\omega_c) = \frac{\mathcal{A}V_0}{2} \sum_{m_x} \sum_{m_I} \sum_{n=0}^{\lceil \beta/2 \rceil} \Big(\mathcal{I}_{cw}(\Delta + n2\pi\nu + (m_I + m_x)2\pi A_\parallel, |J_n^*(\beta)\Omega|) - \mathcal{I}_{cw}(\Delta - n2\pi\nu + (m_I + m_x)2\pi A_\parallel, |J_n^*(\beta)\Omega|) \Big). \tag{B22}$$

Equations (B21) and (B22) are plotted in figure 3(c).

[1] L. Robledo, H. Bernien, T. van der Sar, and R. Hanson, "Spin dynamics in the optical cycle of single nitrogen-vacancy centres in diamond," New J. Phys. **13**, 025013 (2011).
[2] J. R. Carson, "Notes on the theory of modulation," Proc. IRE **10**, 57 (1922).

Chapter 6

Magnetometry Based on Pump Absorption

6.1 Introduction

In this chapter, we present an alternative technique for sensing magnetic fields with NV centers that enables us to circumvent the difficulties of low fluorescence collection efficiency. The ground state population of NV centers depends on the spin-states of the electrons. As a consequence, the electron spin-states can be detected by recording the pump light level transmitted through the diamond.

We use the concept of absorption detected magnetic resonance (ADMR), which is obtained by monitoring the transmitted pump light and sweeping the MW drive around NV spin resonances. As the contrast of ADMR is very low ($\sim 10^{-6}$), we enhance the ADMR signal by building an optical cavity around the diamond. Considering five electronic levels for the NV centers, a set of optical Bloch equations is used to model the frequency-modulated ADMR spectrum.

By measuring the pump light transmitted through the cavity, we demonstrate a magnetic noise spectral density of ~ 100 nT/$\sqrt{\text{Hz}}$ for an input power of 0.4 W. We obtain a bandwidth of 125 Hz followed by a 12 dB/octave roll-off that is generated by the low-pass filter of the LIA. In addition, we estimate a photon-shot-noise-limited sensitivity of ~ 1 pT/$\sqrt{\text{Hz}}$ by measuring the reflection of the cavity at the impedance-matched point and using a diamond with an optimized NV concentration.

6.2 Publication

This section was published in Physical Review B with the title of "Nitrogen-vacancy ensemble magnetometry based on pump absorption" as follows:

Nitrogen-vacancy ensemble magnetometry based on pump absorption

Sepehr Ahmadi, Haitham A. R. El-Ella, Adam M. Wojciechowski, Tobias Gehring, Jørn O. B. Hansen, Alexander Huck, and Ulrik L. Andersen
Department of Physics, Technical University of Denmark, 2800 Kongens Lyngby, Denmark

(Received 30 May 2017; revised manuscript received 18 December 2017; published 11 January 2018)

We demonstrate magnetic-field sensing using an ensemble of nitrogen-vacancy centers by recording the variation in the pump-light absorption due to the spin-polarization dependence of the total ground-state population. Using a 532 nm pump laser, we measure the absorption of native nitrogen-vacancy centers in a chemical-vapor-deposited diamond placed in a resonant optical cavity. For a laser pump power of 0.4 W and a cavity finesse of 45, we obtain a noise floor of $\sim$100 nT/$\sqrt{\text{Hz}}$ spanning a bandwidth up to 125 Hz. We project a photon shot-noise-limited sensitivity of $\sim$1 pT/$\sqrt{\text{Hz}}$ by optimizing the nitrogen-vacancy concentration and the detection method.

DOI: 10.1103/PhysRevB.97.024105

I. INTRODUCTION

The nitrogen-vacancy (NV) center in diamond is currently one of the most studied and anticipated platforms for high spatial-resolution sensing of magnetic fields [1–3], electric fields [4], and temperature [5,6] at ambient conditions. Several novel applications using diamond sensors are currently being developed in the fields of neuroscience [7,8], cellular biology [9,10], nanoscale magnetic resonance microscopy [11], paleomagnetism [12], and microelectronics [13,14].

Many magnetometer schemes using NV centers are based on recording the change in the detected fluorescence level upon a shift of the electron spin precession frequency due to a change of an external magnetic field [8,10,15,16]. The fluorescence contribution of an ensemble of NV centers to the signal increases the optically detected magnetic resonance (ODMR) amplitude and hence boosts the sensitivity by $\sqrt{N}$, where N is the number of NV centers [17]. However, the high refractive index of diamond ($\sim$2.4) together with the near uniform emission of NV center ensembles trap most of the generated fluorescence due to total internal reflection. This limits the collection efficiency and thus the smallest detectable magnetic-field change. To increase the fluorescence collection from a diamond, several techniques have been demonstrated such as fabricating a solid immersion lens [18], side-collection detection [19], employing a silver mirror [20], using a dielectric optical antenna [21], emission into fabricated nanopillar waveguides [22], and employing a parabolic lens [23]. Alternatively, magnetic fields can also be sensed efficiently by observing the cavity-enhanced change in the shelving-state infrared absorption [24,25], or the change in fluorescence when transitioning through the ground-state level anticrossing of the NV center [26].

In this article, we report on a measurement technique for NV ensemble magnetometry, which is based on monitoring the spin-dependent absorption of the pump field. Using the absorption detected magnetic resonance (ADMR) measurement technique in conjunction with a cavity resonant with the pump field, we fully circumvent challenges associated with inefficient collection of fluorescence by detecting the absorption through the transmitted cavity mode. We demonstrate a NV ensemble magnetometer for low-frequency magnetic-field sensing with a measured noise floor of $\sim$100 nT/$\sqrt{\text{Hz}}$ spanning a bandwidth up to 125 Hz. Intriguingly, using the reflection of an impedance-matched cavity and a diamond crystal with an optimized NV concentration, we project an estimated sensitivity of $\sim$1 pT/$\sqrt{\text{Hz}}$.

II. ABSORPTION DETECTED MAGNETIC RESONANCE

The electronic level structure of the NV defect is summarized in Fig. 1(a). It consists of a $^3A_2$ spin-triplet ground state, a ^3E spin-triplet excited state, and a $^1A_1 \leftrightarrow {}^1E$ shelving state. Pumping with a 532 nm laser results in an excitation above the zero-phonon line, which decays on a picosecond time scale [27] to the ^3E excited states by nonradiative transitions. Moreover, there exists a nonradiative decay path through the shelving state that is more probable for $m_s = \pm 1$ of the excited state $|4\rangle$. Continuous optical pumping depopulates the $m_s = \pm 1$ spin sublevel and accumulates the population in $m_s = 0$. The zero-field splitting of the ground state levels $|1\rangle$ and $|2\rangle$ is $\sim$2.87 GHz at room temperature, making the transition between these levels accessible using microwave (MW) fields. The presence of a local magnetic field lifts the degeneracy of $m_s = \pm 1$ with a splitting proportional to $2\gamma_e B_{\text{NV}}$, where $\gamma_e = 2.8$ GHz/T is the gyromagnetic ratio of the electron spin and B_{NV} corresponds to the magnetic-field projection along the NV symmetry axis. A change in the external magnetic field hence results in a detectable shift in the electron-spin resonance frequency of the ODMR or the ADMR spectrum. The continuous-wave sensitivity of the spin resonances to small changes of an external magnetic field is proportional to $\max[\frac{d}{dw}S]^{-1}$, where $\frac{d}{dw}$ is the derivative with respect to the MW frequency $\omega/2\pi$ of the ADMR signal S. Using a cavity around the diamond host crystal, a change in S can be detected by a measurement of the remaining pump light either transmitted through or reflected off the cavity. Intriguingly, by appropriately tailoring the impedance of the cavity, it is possible to obtain a unity contrast in the reflected light

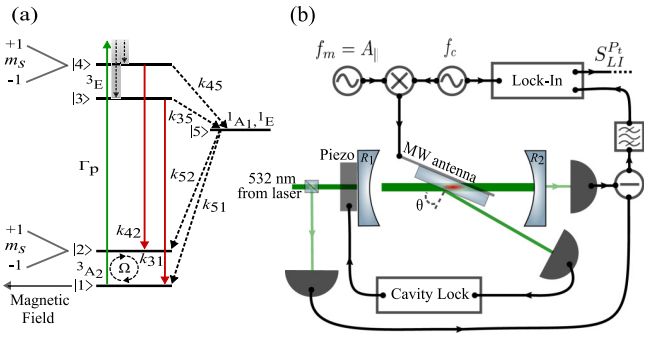

FIG. 1. (a) Summary of the NV center energy levels and transitions between them. Green laser light excites the NV center with a rate Γ_p to a quasicontinuous vibronic state that decays quickly to the optical excited states. The decay between two states is shown by k_{ab}, and Ω corresponds to the Rabi frequency of the MW drive. The presence of a magnetic field lifts the degeneracy of $m_s = \pm 1$ proportional to $2\gamma_e B_{\mathrm{NV}}$. Nonradiative transitions are shown by dashed arrows. (b) Schematic of our experimental setup to perform ADMR measurements through the cavity transmission (see the main text and the Supplemental Material [28] for further experimental details).

power, which in turn may lead to a sensitivity in the $\mathrm{pT}/\sqrt{\mathrm{Hz}}$ range.

III. EXPERIMENT

We use the native $^{14}\mathrm{NV}^-$ concentration of an off-the-shelf single-crystal diamond grown by chemical vapor deposition. A schematic of the experimental setup is shown in Fig. 1(b). The optical cavity consists of two concave mirrors with a 10 cm radius of curvature set in a confocal configuration, resulting in a minimum beam waist of 92 μm with a Rayleigh length of ∼50 mm. The mirrors have measured reflectivities of $R_1 = 94.8 \pm 0.1\,\%$ and $R_2 = 99.8 \pm 0.1\,\%$ at a pump wavelength of 532 nm. With the diamond rotated at its Brewster angle ($\theta \simeq 67^\circ$), the round-trip beam path in the diamond is $l = 2 \times 1.3$ mm and the estimated excitation volume is $\sim 3.5 \times 10^{-2}\,\mathrm{mm}^3$, accounting for the standing wave and the transverse beam profile. The finesse of a cavity is defined by $F = \pi\sqrt{\rho}/(1-\rho)$, where $\rho = \sqrt{R_1 R_2 e^{-\alpha}}$ corresponds to the cumulative round-trip loss product and α is the propagation loss coefficient. In the absence of the diamond, the finesse depends solely on the product of the mirror reflectivities $R_1 R_2$ and is calculated as $F = 113.4 \pm 4.4$, which is confirmed by the measured finesse of $F = 114 \pm 0.1$. Incorporating the diamond into the cavity reduces the finesse to $F = 45.1 \pm 0.1$, which indicates that all the effective loss in the loaded cavity can be attributable solely to losses occurring through the diamond. The corresponding cumulative round-trip loss of the loaded cavity shows that the cavity is slightly undercoupled. The propagation loss can be decomposed to $\alpha = \alpha_{\mathrm{abs}} l + \alpha_r$, in which α_{abs} is the absorption loss coefficient and α_r is attributed to all other loss channels, such as surface-based absorption, scattering losses, and birefringence losses. The total fraction of reflected light from the diamond to intracavity power was measured as ∼0.006, of which approximately 80% was s-polarized light. This translates to an absorption loss coefficient of $\alpha_{\mathrm{abs}} \sim 0.0301\ \mathrm{mm}^{-1}$, taking $\alpha_r \sim 0.006$. With an independent measurement using a confocal microscope, we determined the NV^- concentration, $[\mathrm{NV}^-]$, to be $\sim 2.9 \times 10^{10}\ \mathrm{mm}^{-3}$ (∼0.16 ppb) corresponding to $\sim 10^9$ NV^- centers within the excitation volume. Considering the absorption cross section of a single $^{14}\mathrm{NV}^-$ at 532 nm ($\sigma_{\mathrm{NV}} = 3.1 \times 10^{-15}\ \mathrm{mm}^2$ [29]), a NV-related absorption loss coefficient of $\alpha_{\mathrm{abs}}^{\mathrm{NV}} \sim 9 \times 10^{-5}\ \mathrm{mm}^{-1}$ is obtained. Hence, in our diamond sample most of the propagation loss is attributed to non-NV loss channels. Using the NV absorption loss coefficient, we estimate the ratio between the excitation rate and the intracavity power $\epsilon = \Gamma_p / P_{\mathrm{cav}} \sim 75$ kHz/W, where the intracavity and incident powers are linked through $P_{\mathrm{cav}} = P_{\mathrm{in}}(1 - R_1)/|1 - \sqrt{R_1 R_2 e^{-\alpha}}|^2$.

A. Spectrum

We performed ADMR measurements by recording the remaining pump light transmitted through the diamond-loaded cavity while sweeping the MW drive frequency across the spin resonance. To reduce the technical noise level in our measurement, we tapped off some laser light before the cavity, recorded it with a second photodetector, and subtracted the two photocurrents, as indicated in Fig. 1(b). To remove low-frequency technical noise, we applied lock-in detection with a frequency-modulated MW drive, directly yielding $S_{\mathrm{LI}}^{P_t}$ at the output, where P_t indicates the transmitted power through the cavity, and LI refers to lock-in (further experimental details can be found in the Supplemental Material [28]). A typical frequency-modulated ADMR spectrum is presented in Fig. 2(a). In these measurements, a static magnetic field was aligned along the [111] axis, resulting in the outermost electron spin resonances (SR1,SR4), while the inner peaks (SR2,SR3) correspond to the electron spin resonances of the other three crystallographic orientations. The three-peak feature of the ADMR spectrum in Fig. 2(a) is a consequence of the hyperfine

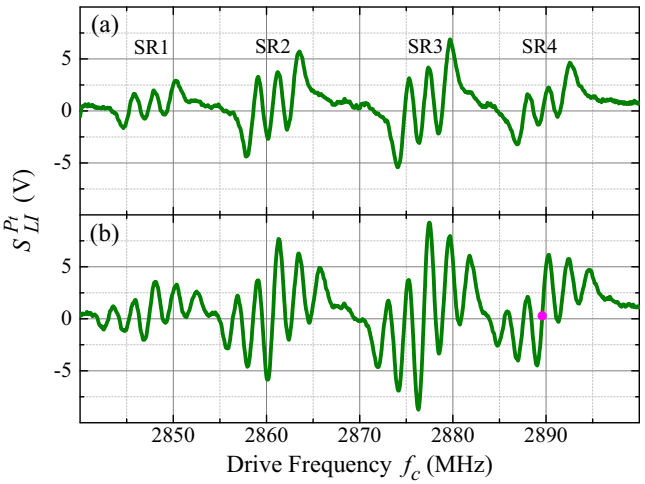

FIG. 2. Measured frequency-modulated ADMR spectrum using (a) single-frequency excitation and (b) three-frequency excitation. SR1 and SR4 correspond to the electron-spin resonances of single crystallographic orientation of NV centers, while SR2 and SR3 correspond to the electron-spin resonances of the other three crystallographic orientations. The purple dot in (b) indicates the point that is most sensitive to small changes in the magnetic field.

interaction between the NV electron spin and the intrinsic ^{14}N nuclear spin with a coupling constant of $A_{||} = 2.16$ MHz [30]. To enhance max$[\frac{d}{dw}(S_{\rm LI}^{P_t})]$, we excited all three ^{14}N hyperfine transitions simultaneously by mixing the modulation frequency f_c with a $f_m = A_{||}$ signal. The three-frequency excitation results in five peaks for each electron spin resonance, as shown by the measured spectrum in Fig. 2(b).

B. Model

An ADMR spectrum $S_{\rm LI}$ may be obtained by recording the pump beam either reflected from the cavity, $S_{\rm LI}^{P_r}$, or transmitted through the cavity, $S_{\rm LI}^{P_t}$, as a function of the applied MW frequency, and it may be modeled using a set of optical Bloch equations considering the five electronic levels and the transitions summarized in Fig. 1(a) [31]. The steady-state level populations $\rho^{\rm ss}$ are then obtained as a function of Rabi frequency Ω, optical excitation rate Γ_p, and MW detuning Δ from the spin $m_s = 0 \leftrightarrow m_s = \pm 1$ transition. The cavity reflection or transmission itself is a function of loss inside the cavity, which is dominated by the absorption in diamond, while the NV absorption in diamond depends on the NV ensemble ground-state spin population. Applying a resonant MW field ($\Delta = 0$) increases the population in the shelving state $|5\rangle$, which possesses a longer lifetime (>150 ns [32,33]) than the ^3E excited states, and hence a lower average population remains in the ground states $|1\rangle$ and $|2\rangle$ to absorb the pump photons. Ultimately, the resonant MW field decreases the optical loss inside the cavity, which can be monitored through the light transmitted or reflected from the cavity. The steady-state population of the optical ground state can be written as

$$\rho_g^{\rm ss}(\Omega,\Gamma_p,\Delta) = \rho_{11}^{\rm ss} + \rho_{22}^{\rm ss}, \tag{1}$$

where $\rho_{11}^{\rm ss}$ and $\rho_{22}^{\rm ss}$ are the steady-state populations of $|1\rangle$ and $|2\rangle$, respectively. As the absorption of a NV ensemble depends directly on $\rho_g^{\rm ss}$, a change in the propagation loss as a function of $[{\rm NV}^-]$ can be described as

$$\alpha(\Omega,\Gamma_p,\Delta,[{\rm NV}^-]) = \alpha_{\rm abs}^0 + [{\rm NV}^-]\sigma_{\rm NV} l \rho_g^{\rm ss} + \alpha_r, \tag{2}$$

where $\alpha_{\rm abs}^0$ is the loss coefficient attributed to non-NV absorption. As pump absorption in our sample is dominated by non-NV-related processes, the absorption-based spin contrast $C_{\rm ADMR}$ related to the fraction $\alpha_{\rm abs}^{\rm NV}/\alpha$ is on the order of 10^{-6} when monitoring the absorption through the cavity transmission. The steady-state cavity outputs as a function of MW detuning are then reformulated in terms of transmitted and reflected powers:

$$\frac{P_t}{P_{\rm in}} = \frac{T_1 T_2 e^{-\alpha(\Omega,\Gamma_p,\Delta,[{\rm NV}^-])}}{|1-\sqrt{R_1 R_2 e^{-\alpha(\Omega,\Gamma_p,\Delta,[{\rm NV}^-])}}|^2}, \tag{3}$$

$$\frac{P_r}{P_{\rm in}} = \frac{(R_1 - \sqrt{R_1 R_2 e^{-\alpha(\Omega,\Gamma_p,\Delta,[{\rm NV}^-])}})^2}{R_1|1-\sqrt{R_1 R_2 e^{-\alpha(\Omega,\Gamma_p,\Delta,[{\rm NV}^-])}}|^2}, \tag{4}$$

where $P_{\rm in}$ is the laser input power to the cavity, T_1 and T_2 are the transmissions of the first and second mirror, respectively, and we assume $R_i + T_i = 1$. For the sake of simplicity, the intracavity excitation rate ($\Gamma_p = \epsilon P_{\rm cav}$) is calculated in terms of the input power and the propagation loss when no MW field is applied ($\Omega = 0$, $\Delta\rho_g^{\rm ss} = 1$). The lock-in signal $S_{\rm LI}^{P_i}$ can be described as a function of detuning between the carrier frequency f_c, the resonance frequency f_0 ($\Delta = f_c - f_0$), and the modulation depth δ through

$$S_{\rm LI}^{P_i}(\Delta) = \frac{GV_0}{2}\sum_{m_x}\sum_{m_l}\{P_i[\Delta+\delta+(m_l+m_x)A_{||}] - P_i[\Delta-\delta+(m_l+m_x)A_{||}]\}, \tag{5}$$

where G is the lock-in gain factor, V_0 is the off-resonant detected voltage, and P_i is either the reflected or transmitted cavity power. The expression is summed over the ^{14}N nuclear spin quantum number $m_l = \{-1,0,1\}$, and the three frequencies m_x separated by $A_{||}$ in order to account for the simultaneous drive of all three hyperfine transitions.

Using Eq. (5), $S_{\rm LI}^{P_i}$ is plotted as a solid line in Fig. 3(a), taking $P_{\rm in} = 0.4$ W, $\Omega = 0.3$ MHz, a pure dephasing rate of $\gamma_2^* = 1/3$ MHz, a longitudinal relaxation rate of $\gamma_1 = 0.182$ kHz, and level decay rates k_{ab} extracted from [32]. We also plot the measured ADMR spectrum as a dashed line in Fig. 3(a). The ADMR spectrum was recorded with the same $P_{\rm in}$ and Ω as the simulated spectrum. The match between the simulated and measured traces is very good, with just a small mismatch due to the uncertainty in the estimation of the parameters ϵ, γ_2^*, and $\alpha_{\rm abs}^0$ in the simulation.

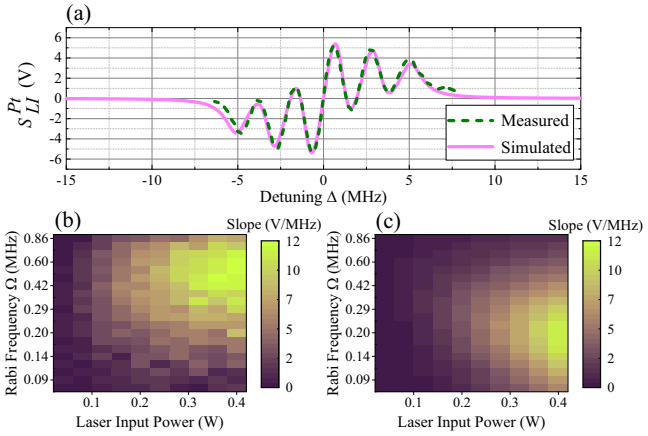

FIG. 3. (a) Simulated and measured frequency-modulated ADMR spectra using three-frequency excitation. The used parameters are $P_{\rm in} = 0.4$ W, $\Omega = 0.3$ MHz, $R_1 = 94.8\%$, $R_2 = 99.8\%$, $\alpha_{\rm abs}^0 = 0.0781$, $\alpha_r = 0.006$, $[{\rm NV}^-] = 0.16$ ppb, $l = 2 \times 1.3$ mm, $\epsilon = 75$ kHz/W, $\gamma_2^* = 1/3$ MHz, $\gamma_1 = 0.182$ kHz, and $GV_0 = 65 \times 10^6$ V. (b) Measured and (c) simulated slopes of three-frequency excitation, frequency-modulated ADMR spectra at $\Delta = 0$ as a function of $P_{\rm in}$ and Ω. The maximum measured slope in (b) is obtained for $P_{\rm in} = 0.4$ W and $\Omega \sim 0.3$ MHz.

C. Sensitivity

To optimize the magnetic-field sensitivity, we measure the dependence of $\frac{d}{dw}(S_{\rm LI}^{P_i})$ of three-frequency excitation spectra on the pump power and Rabi frequency, $P_{\rm in}$ and Ω, at $\Delta = 0$. The results of these measurements are presented in Fig. 3(b). The maximum slope is achieved at $P_{\rm in} = 0.4$ W and $\Omega \sim 0.3$ MHz, where the optical excitation rate by virtue of the

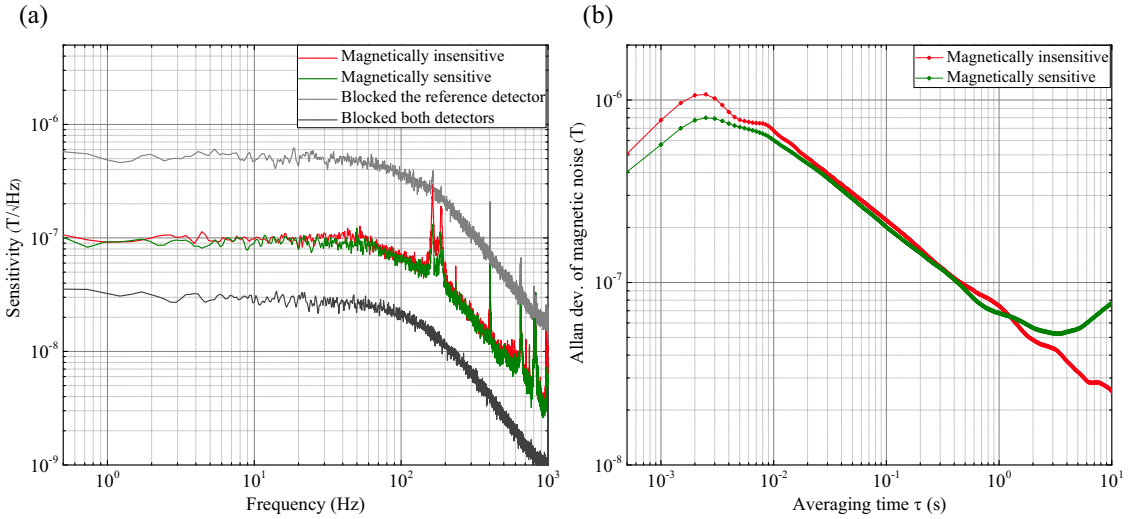

FIG. 4. (a) Measurements of the magnetic noise spectral density: when the MW drive is set on the maximum slope of the frequency-modulated ADMR, corresponding to the purple dot in Fig. 2(b) (magnetically sensitive - green trace), when the MW drive is far from any spin resonance (magnetically insensitive - red trace), when we do not cancel out the correlated laser noise (blocked the reference detector - gray trace), and the noise floor of the lock-in and blocked detectors for the same gain setting (black trace). (b) Measurements of the Allan deviation of magnetic noise of the traces in (a). The drop with the slope of $-1/2$ identifies the white noise in the system. For the magnetically sensitive trace, there is a minimum at ∼3.3 s that increases at higher averaging time due to thermal or mechanical drift in the system. The Allan deviation was calculated using the overlapping method.

cavity enhancement overcomes the MW power-induced broadening, allowing for a narrowing regime to be reached [34]. The simulated slopes are presented in Fig. 3(c) and obtained using the same parameters as in Fig. 3(a). We observe a very good agreement with respect to the overall trend, the slope magnitude, and the location of the slope maximum.

For deducing the sensitivity of the magnetometer, we independently measured four time traces of the lock-in signal for $P_{\text{in}} = 0.4$ W. The first trace was measured in the optimal magnetically sensitive configuration, with the MW drive on resonance with a spin transition ($\Delta = 0$) corresponding to the purple dot in Fig. 2(b). The second trace was measured in the magnetically insensitive configuration, with the MW drive frequency far-detuned from any spin resonance ($\Delta \to \infty$). The third trace was measured by blocking the reference detector that monitored the laser output. The last trace was measured with all detectors blocked, which shows the sum of electronic noise from the lock-in detector and photodetectors. The Fourier transforms of these time traces with a frequency resolution of 0.24 Hz are presented in Fig. 4(a), where the y axis is displayed in units of sensitivity. It shows a 125 Hz bandwidth and a 12 dB/octave roll-off that is generated by the low-pass filter of the lock-in detector. The choice of this bandwidth is a consequence of the low ADMR contrast ($C_{\text{ADMR}} \sim 10^{-6}$) measured through the cavity transmission. When the MW drive is off-resonance, a noise floor of ∼100 nT/$\sqrt{\text{Hz}}$ is achieved. The increased noise floor when we blocked the reference detector and only monitored the transmission through the cavity shows the impact of substantial technical noise at the 35 kHz modulation frequency. Next, we calculated the Allan deviation of both magnetically insensitive and magnetically sensitive traces, which allows us to investigate the intrinsic noise in the system. The results are presented in Fig. 4(b). The drop of the Allan deviation with a slope of $-1/2$ in both traces is a signature of white noise. For the magnetically sensitive measurements, the white noise reaches a minimum at ∼3.3 s. The increase of the Allan deviation at higher averaging time is a sign of thermal or mechanical drift in the system.

IV. OUTLOOK

To better understand the context and magnitude of the measured sensitivity, we estimate the shot-noise-limited sensitivity for a single-peak ADMR as a function of [NV$^-$], P_{in}, and Ω. Using the same physical dimensions as in our setup (cavity length and diamond thickness), we assume a diamond host where $\alpha^0_{\text{abs}} = \alpha^{\text{NV}}_{\text{abs}}$ for any [NV$^-$]. In addition, we consider that the reflectivity of the incoupling mirror is such that $R_1 = R_2 e^{-\alpha}$ when $\Omega = 0$ for a given optical input power, ensuring that the cavity is impedance-matched. The intracavity power is thereby always maximized and there is no cavity reflection when no MW field is applied. The shot-noise-limited sensitivity was estimated from the ratio of the shot-noise level to max$[\frac{d}{dw} S]$. The results of this calculation are presented in Fig. 5 for both transmitted (a,b) and reflected (c,d) powers. We have fixed $\Omega = 0.5$ MHz for (a,c) and $P_{\text{in}} = 0.5$ W for (b,d). By monitoring the transmitted power P_t and optimizing [NV$^-$], P_{in}, and Ω, a shot-noise-limited sensitivity in the sub-100-pT/$\sqrt{\text{Hz}}$ range can be expected. In comparison, by monitoring the reflected power P_r, a sensitivity in the pT/$\sqrt{\text{Hz}}$ range is projected. As the cavity is impedance-matched, applying no MW field results in $P_r(\Omega = 0) \sim 0$. However, applying Ω on resonance with a spin transition reduces the loss in the cavity and pushes the cavity into the overcoupled regime. For the case presented in Fig. 5(d) with a fixed input power $P_{\text{in}} = 0.5$ W, the optimal sensitivity of ∼1 pT/$\sqrt{\text{Hz}}$ is obtained for $\Omega =$

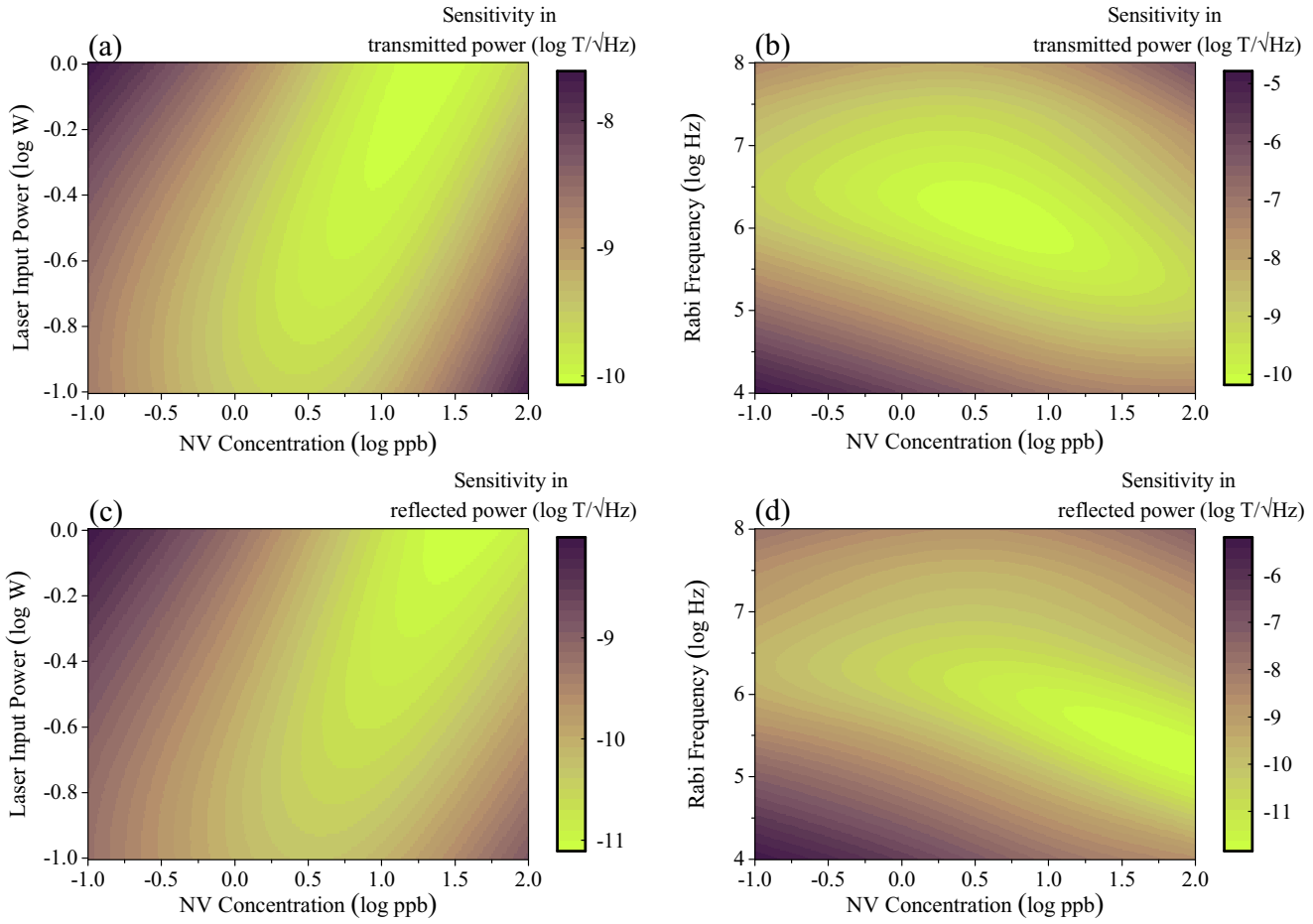

FIG. 5. Simulated plots of the shot-noise-limited sensitivity as a function of $[NV^-]$, P_{in}, and Ω using the following parameters: $R_1 = R_2 e^{-\alpha}$, $R_2 = 99.9\%$, $\alpha^0_{abs} = \alpha^{NV}_{abs}$, $\alpha_r = 0.006$, $l = 2 \times 1.3$ mm, $\epsilon = 75$ kHz/W, $\gamma_2^* = 1/3$ MHz, and $\gamma_1 = 0.182$ kHz. Parts (a) and (b) are calculated from transmission through the cavity for $\Omega = 0.5$ MHz and $P_{in} = 0.5$ W, respectively. Parts (c) and (d) are calculated from reflection of the cavity for $\Omega = 0.5$ MHz and $P_{in} = 0.5$ W, respectively.

0.21 MHz and $[NV^-] \sim 70.8$ ppb. At these settings, the cavity finesse is 13.7, the intracavity power reaches $P_{cav} = 5.35$ W, and the maximum reflected power $P_r(\Delta = 0) = 0.15\ \mu$W. The total reflected power of such an overcoupled cavity contributes to the ADMR signal.

V. CONCLUSION

In this article, we report on magnetic-field sensing using an ensemble of NV centers based on the variation of transmitted pump power due to electron-spin dependent absorption. Frequency-modulated ADMR spectra were measured, which was used to record the local magnetic noise spectral density with a noise floor of $\sim 100\,\mathrm{nT}/\sqrt{\mathrm{Hz}}$ spanning a bandwidth up to 125 Hz. Our simulations show that a photon shot-noise-limited sensitivity of $\sim 1\ \mathrm{pT}/\sqrt{\mathrm{Hz}}$ can be achieved when measuring a cavity's reflected power near the impedance-matched point and using a diamond with an optimized NV density. ADMR is an alternative to its ODMR counterpart, and it shows some advantages in terms of its projected detection contrast. With the appropriate cavity design and sample optimization, it is anticipated that the work and technique presented here will provide a solid foundation for NV-based magnetometers.

ACKNOWLEDGMENTS

We would like to thank Kristian Hagsted Rasmussen for help with diamond sample preparation and Ruben Grigoryan for technical support. We are also grateful to Jonas Schou Neergaard-Nielsen for fruitful discussions. This work was supported by the Innovation Fund Denmark through the EX-MAD project and the Qubiz center, as well as the Independent Research Fund Denmark through the Sapere Aude project (DIMS).

[1] G. Balasubramanian, I. Y. Chan, R. Kolesov, M. Al-Hmoud, J. Tisler, C. Shin, C. Kim, A. Wojcik, P. R. Hemmer, A. Krueger, T. Hanke, A. Leitenstorfer, R. Bratschitsch, F. Jelezko, and J. Wrachtrup, Nature (London) **455**, 648 (2008).

[2] L. Rondin, J. P. Tetienne, T. Hingant, J. F. Roch, P. Maletinsky, and V. Jacques, Rep. Prog. Phys. **77**, 56503 (2014).

[3] R. Schirhagl, K. Chang, M. Loretz, and C. L. Degen, Annu. Rev. Phys. Chem. **65**, 83 (2014).

[4] F. Dolde, H. Fedder, M. W. Doherty, T. Nöbauer, F. Rempp, G. Balasubramanian, T. Wolf, F. Reinhard, L. C. L. Hollenberg, F. Jelezko, and J. Wrachtrup, Nat. Phys. **7**, 459 (2011).
[5] G. Kucsko, P. C. Maurer, N. Y. Yao, M. Kubo, H. J. Noh, P. K. Lo, H. Park, and M. D. Lukin, Nature (London) **500**, 54 (2013).
[6] P. Neumann, I. Jakobi, F. Dolde, C. Burk, R. Reuter, G. Waldherr, J. Honert, T. Wolf, A. Brunner, J. H. Shim, D. Suter, H. Sumiya, J. Isoya, and J. Wrachtrup, Nano Lett. **13**, 2738 (2013).
[7] L. T. Hall, G. C. G. Beart, E. A. Thomas, D. A. Simpson, L. P. McGuinness, J. H. Cole, J. H. Manton, R. E. Scholten, F. Jelezko, J. Wrachtrup, S. Petrou, and L. C. L. Hollenberg, Sci. Rep. **2**, 1 (2012).
[8] J. F. Barry, M. J. Turner, J. M. Schloss, D. R. Glenn, Y. Song, M. D. Lukin, H. Park, and R. L. Walsworth, Proc. Natl. Acad. Sci. (U.S.A.) **113**, 14133 (2016).
[9] S. Steinert, F. Ziem, L. T. Hall, A. Zappe, M. Schweikert, N. Götz, A. Aird, G. Balasubramanian, L. Hollenberg, and J. Wrachtrup, Nat. Commun. **4**, 1607 (2013).
[10] D. R. Glenn, K. Lee, H. Park, R. Weissleder, A. Yacoby, M. D. Lukin, H. Lee, R. L. Walsworth, and C. B. Connolly, Nat. Methods **12**, 736 (2015).
[11] I. Lovchinsky, A. O. Sushkov, E. Urbach, N. P. de Leon, S. Choi, K. D. Greve, R. Evans, R. Gertner, E. Bersin, C. Müller, L. McGuinness, F. Jelezko, R. L. Walsworth, H. Park, and M. D. Lukin, Science **351**, 836 (2016).
[12] R. R. Fu, B. P. Weiss, E. A. Lima, R. J. Harrison, X.-N. Bai, S. J. Desch, D. S. Ebel, C. Suavet, H. Wang, D. Glenn, D. L. Sage, T. Kasama, R. L. Walsworth, and A. T. Kuan, Science **346**, 1089 (2014).
[13] S. Kolkowitz, A. Safira, A. A. High, R. C. Devlin, S. Choi, Q. P. Unterreithmeier, D. Patterson, A. S. Zibrov, V. E. Manucharyan, H. Park, and M. D. Lukin, Science **347**, 1129 (2015).
[14] I. Jakobi, P. Neumann, Y. Wang, D. Dasari, F. E. Hallak, M. A. Bashir, M. Markham, A. Edmonds, D. Twitchen, and J. Wrachtrup, Nat. Nanotechnol. **12**, 67 (2016).
[15] H. Clevenson, M. E. Trusheim, C. Teale, T. Schröder, D. Braje, and D. Englund, Nat. Phys. **11**, 393 (2015).
[16] S. Ahmadi, H. A. R. El-Ella, J. O. B. Hansen, A. Huck, and U. L. Andersen, Phys. Rev. Appl. **8**, 034001 (2017).
[17] J. M. Taylor, P. Cappellaro, L. Childress, L. Jiang, D. Budker, P. R. Hemmer, A. Yacoby, R. Walsworth, and M. D. Lukin, Nat. Phys. **4**, 810 (2008).
[18] J. P. Hadden, J. P. Harrison, A. C. Stanley-Clarke, L. Marseglia, Y. L. D. Ho, B. R. Patton, J. L. O'Brien, and J. G. Rarity, Appl. Phys. Lett. **97**, 241901 (2010).
[19] D. Le Sage, L. M. Pham, N. Bar-Gill, C. Belthangady, M. D. Lukin, A. Yacoby, and R. L. Walsworth, Phys. Rev. B **85**, 121202 (2012).
[20] N. M. Israelsen, S. Kumar, M. Tawfieq, J. S. Neergaard-Nielsen, A. Huck, and U. L. Andersen, J. Opt. **16**, 114017 (2014).
[21] D. Riedel, D. Rohner, M. Ganzhorn, T. Kaldewey, P. Appel, E. Neu, R. J. Warburton, and P. Maletinsky, Phys. Rev. Appl. **2**, 064011 (2014).
[22] S. A. Momenzadeh, R. J. Stöhr, F. F. De Oliveira, A. Brunner, A. Denisenko, S. Yang, F. Reinhard, and J. Wrachtrup, Nano Lett. **15**, 165 (2015).
[23] T. Wolf, P. Neumann, K. Nakamura, H. Sumiya, T. Ohshima, J. Isoya, and J. Wrachtrup, Phys. Rev. X **5**, 041001 (2015).
[24] K. Jensen, N. Leefer, A. Jarmola, Y. Dumeige, V. M. Acosta, P. Kehayias, B. Patton, and D. Budker, Phys. Rev. Lett. **112**, 160802 (2014).
[25] G. Chatzidrosos, A. Wickenbrock, L. Bougas, N. Leefer, T. Wu, K. Jensen, Y. Dumeige, and D. Budker, Phys. Rev. Appl. **8**, 044019 (2017).
[26] A. Wickenbrock, H. Zheng, L. Bougas, N. Leefer, S. Afach, A. Jarmola, V. M. Acosta, and D. Budker, Appl. Phys. Lett. **109**, 053505 (2016).
[27] V. M. Huxter, T. A. A. Oliver, D. Budker, and G. R. Fleming, Nat. Phys. **9**, 744 (2013).
[28] See Supplemental Material at http://link.aps.org/supplemental/10.1103/PhysRevB.97.024105 for experimental details on diamond and cavity setup, MW delivery, detection, data analysis, and the magnetometer response to an applied magnetic field.
[29] T. L. Wee, Y. K. Tzeng, C. C. Han, H. C. Chang, W. Fann, J. H. Hsu, K. M. Chen, and E. C. Yu, J. Phys. Chem. A **111**, 9379 (2007).
[30] B. Smeltzer, J. McIntyre, and L. Childress, Phys. Rev. A **80**, 050302(R) (2009).
[31] H. A. R. El-Ella, S. Ahmadi, A. M. Wojciechowski, A. Huck, and U. L. Andersen, Opt. Express **25**, 14809 (2017).
[32] L. Robledo, H. Bernien, T. V. D. Sar, and R. Hanson, New J. Phys. **13**, 025013 (2011).
[33] V. M. Acosta, A. Jarmola, E. Bauch, and D. Budker, Phys. Rev. B **82**, 201202 (2010).
[34] K. Jensen, V. M. Acosta, A. Jarmola, and D. Budker, Phys. Rev. B **87**, 014115 (2013).

Supplemental Material for "Nitrogen-Vacancy Ensemble Magnetometry Based on Pump Absorption"

Sepehr Ahmadi, Haitham A.R. El-Ella, Adam M. Wojciechowski,
Tobias Gehring, Jørn B. Hansen, Alexander Huck, and Ulrik L. Andersen
Department of Physics, Technical University of Denmark, 2800 Kongens Lyngby, Denmark

EXPERIMENTAL DETAILS

Diamond and Cavity Setup

The diamond sample, grown by chemical vapor deposition (Element 6), with a dimension of 6 mm × 6 mm × 1.2 mm and a stated nitrogen concentration of <1 ppm was mounted on a MW antenna board and placed in the center of an optical cavity at its Brewster angle of $\theta \simeq 67° \pm 0.4°$ relative to the cavity axis. Both mirrors were anti-reflection coated for 532 nm wavelength at their flat ends and the incoupling mirror was attached to a piezo actuator for cavity stabilization. The cavity was pumped with a phase-modulated and p-polarized 532 nm laser possessing a single longitudinal mode (Verdi SLM, Coherent). The birefringence behavior of the diamond [1] made it possible to observe resonances of the cavity by detecting the s-polarized reflected light from the diamond surface. We detected this reflected light with a silicon photodetector (Thorlabs PDA10A) and used an in-house built feedback servo to lock the cavity by the Pound-Drever-Hall technique.

MW Delivery

The MW field was delivered using a homemade MW antenna consisting of a split-ring resonator lithographically prepared on a printed circuit board [2, 3]. The antenna had a measured resonance at 2.884 GHz and a bandwidth of $\sim$ 91 MHz. The homogeneity of the MW field was tested by measuring the Rabi frequency Ω in a confocal microscopy setup and varied $< 3\%$ over a 2 mm^2 area of a diamond sample.

Detection

We used a homemade photodetector which subtracted the currents of two Hamamatsu S2386-18K photodiodes and converted it to voltage via a 11 kΩ load. The first photodiode measured the transmission light through the cavity and the second photodiode monitored the laser output before the cavity. The power on the second photodiode was adjusted to get zero DC voltage output after subtraction. The detector was attached to a second-order band-pass filter with a 35 kHz central frequency. In order to extract the signal from the low-frequency noisy environment, we used a lock-in detector (Stanford Research Systems SR850) with a 1 ms time constant, by modulating the MW drive at 35 kHz modulation rate and 0.75 MHz modulation depth.

Data Analysis

Time traces were recorded using 2 kHz sampling rate for 100 s. The power spectral density was estimated using the Welch's method with 25 Blackman-Harris window, and 50% of the window length as the number of overlapped samples. The spectrum was then converted to the amplitude spectral density and in units of magnetic field sensitivity.

APPLYING A MAGNETIC FIELD

We generated a 60 Hz sine-wave magnetic field by placing a coil close to the diamond and monitored the magnetometer response by recording the lock-in signal. The Fourier transform of the recorded time trace is presented in Fig. 1(a) in units of sensitivity. A small portion of the time trace is shown in Fig. 1(b). By applying a digital band-pass filter from 55 Hz to 65 Hz, the 60 Hz signal may be reconstructed, as presented in Fig. 1(c).

[1] K. Jensen, N. Leefer, A. Jarmola, Y. Dumeige, V. M. Acosta, P. Kehayias, B. Patton, and D. Budker, Physical Review Letters **112**, 160802 (2014).
[2] M. Shamonin, E. Shamonina, V. Kalinin, and L. Solymar, Microwave and Optical Technology Letters **44**, 133 (2005).
[3] K. Bayat, J. Choy, M. Farrokh Baroughi, S. Meesala, and M. Loncar, Nano Letters **14**, 1208 (2014).

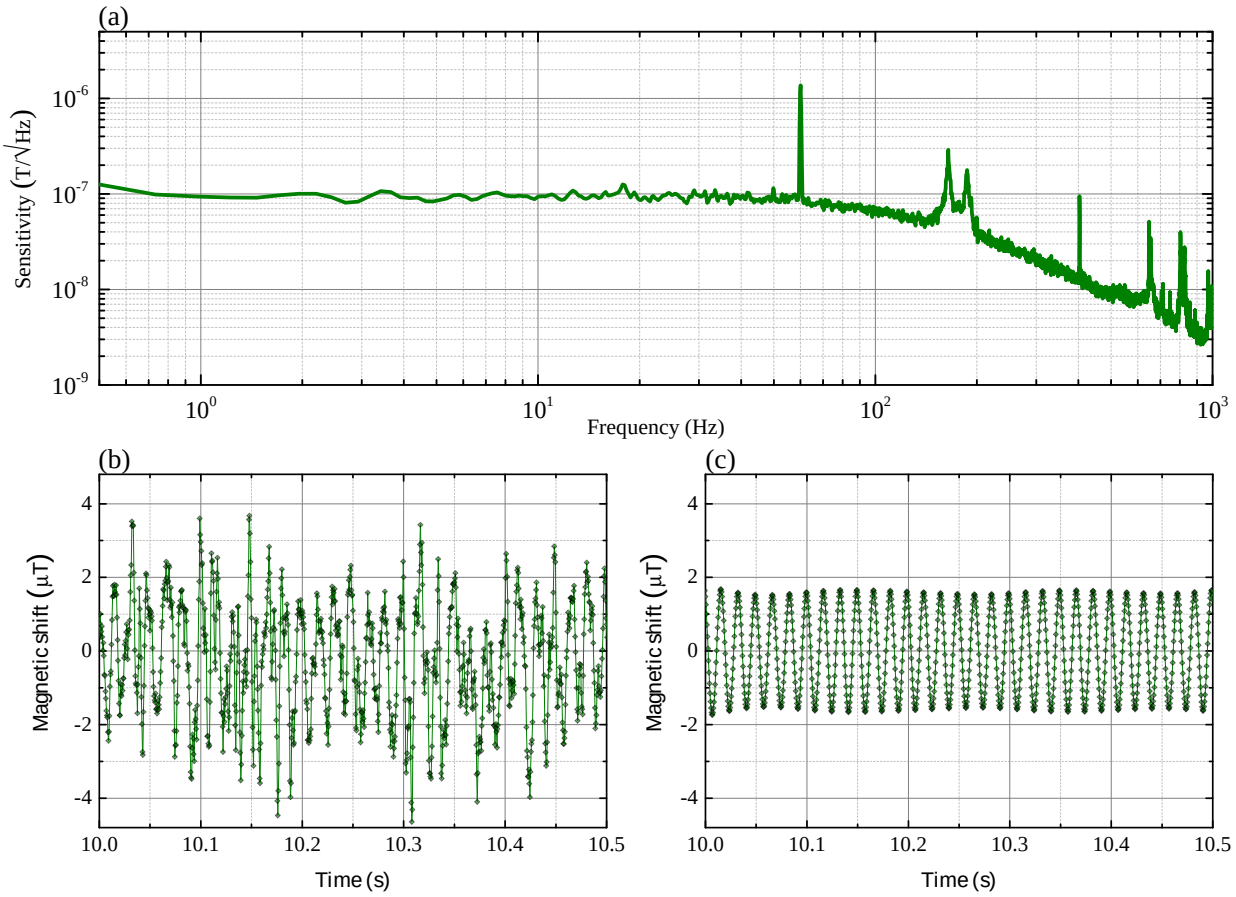

FIG. 1. (a) Measurement of the magnetic noise spectral density (b) The magnetometer response to a 60 Hz applied sine-wave magnetic field as a function of time. (c) The same response as (b) band-pass filtered from 55 Hz to 65 Hz.

6.3 Reflection-based magnetometry

Using the reflection of an impedance-matched cavity is an approach to enhance the sensitivity, as discussed in the last section. We attempted to impedance-match our optical cavity to perform reflection-based magnetometry.

Initially, a mirror with a reflectivity of $R_1 = 90\%$ at a pump wavelength of 532 nm, replaced the incoupling mirror. A CVD diamond was laser-sliced into three pieces at Almax easyLab, with the thickness of 150 μm, 250 μm, and 350 μm. In all cases, the cavity is overcoupled due to the low loss of the diamond slabs. To reach the impedance-matched point, we added more loss inside the cavity by rotating the diamond slightly from the Brewster angle, and an optical isolator was used to measure the cavity reflection. Although the impedance-matched point should be reachable, we only observed a minimum of $\sim 20\%$ reflection from the cavity.

For this condition, a high reflection from cavity with a laser input of 400 mW saturates the photodetector. We attenuated the reflection power to ~ 1 mW and measured an ADMR spectrum, shown in Fig. 6.1 (a). To deduce the sensitivity, we recorded a time trace while the MW drive was off-resonance. The ASD of the time trace is displayed in Fig. 6.1 (b) in units of sensitivity, showing a sensitivity of ~ 600 nT/$\sqrt{\text{Hz}}$, limited by the impedance-mismatched cavity.

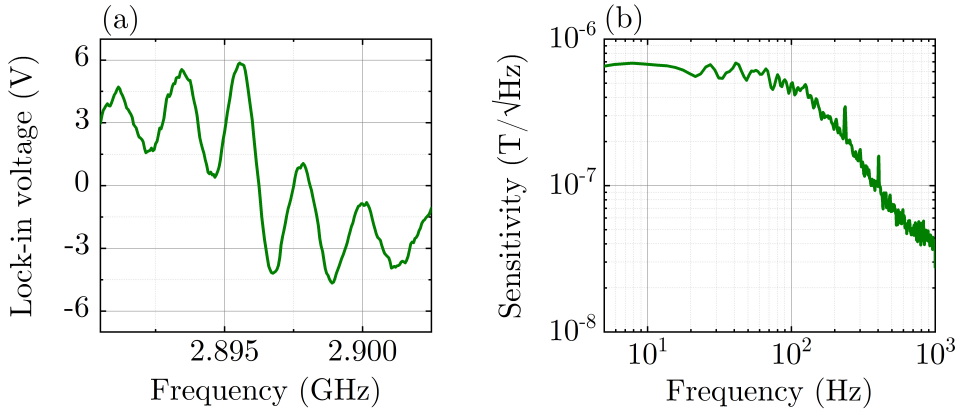

Figure 6.1: (a) Plot of the measured reflection-based three-frequency-modulated ADMR spectrum. (b) Measurement of the noise spectral density when the MW drive is far from any spin resonance (magnetically insensitive).

Later, we used an optical fiber (Thorlabs P5-488PM-FC-2) to create a beam with a Gaussian intensity profile just before entering the optical isolator. Using the fiber reduced the cavity reflection to $\sim 10\%$ as shown in

Fig. 6.2. However, the fiber could not withstand high laser power and no ADMR signal was measured for a cavity laser input of 10 mW.

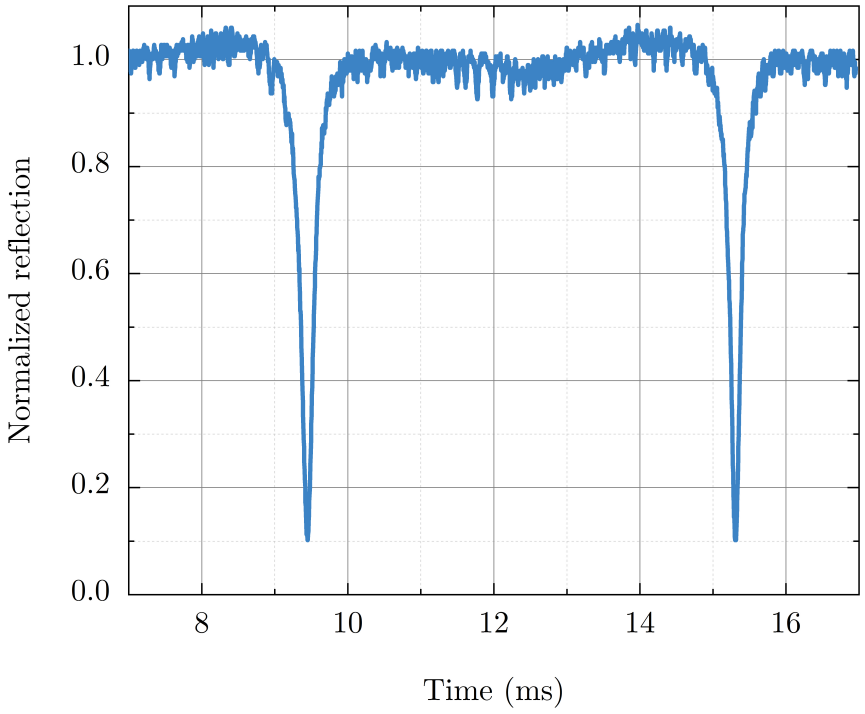

Figure 6.2: Reflection spectrum of the loaded optical cavity as a function of time.

Chapter 7

Cavity-Enhanced Magnetometry

7.1 Introduction

This chapter includes a summary of our results on cavity-enhanced magnetometry, which is described in two parts. The first part presents continuous-wave magnetometry with NV centers based on fluorescence detection. The second part introduces NV ensemble magnetometry based on the absorption of the pump field.

7.2 Publication

The following paper was presented at the Conference on Lasers and Electro-Optics (CLEO) and published in OSA Publishing's Digital Library with the title of "Cavity-Enhanced Nitrogen-Vacancy Ensemble Magnetometry":

Cavity-Enhanced Nitrogen-Vacancy Ensemble Magnetometry

Sepehr Ahmadi, Haitham A. R. El-Ella, Adam M. Wojciechowski, Tobias Gehring, Jørn O. B. Hansen, Alexander Huck, and Ulrik L. Andersen

Department of Physics, Technical University of Denmark, 2800 Kongens Lyngby, Denmark

sepehr.ahmadi@fysik.dtu.dk

Abstract: We demonstrate magnetic-field sensing using the intrinsic nitrogen-vacancy concentration of a single-crystal diamond placed in an optical cavity resonant with the pump field. We investigate two approaches based on fluorescence detection and pump absorption, respectively.

OCIS codes: 270.0270, 160.2220, 020.0020.

1. Introduction

Ensembles of nitrogen-vacancy (NV) centers in diamond are a highly promising platform for high-sensitivity detection of magnetic fields, electric fields, and temperature at ambient conditions, with potential applications in various fields including neuroscience, nanoscale magnetic resonance microscopy, and microelectronics [1]. Here, we report on the combination of a diamond sample with an optical cavity resonant with the pump field. This combination allows us to reach an enhanced sensitivity with fluorescence light detection. Additionally, we report on magnetic field sensing by recording the remaining pump light level.

2. Magnetometry based on fluorescence detection

An external magnetic field shifts the electron spin precession frequency of NV centers, which can be detected by monitoring the fluorescence level while driving a microwave (MW) field. This optically detected magnetic resonance (ODMR) technique is commonly used for continuous-wave magnetometry with NV centers.

In our experiments, we used the native NV^- concentration of $<$0.2 ppb of an untreated single-crystal diamond grown by chemical vapor deposition. Two concave mirrors form a confocal cavity around the diamond which was placed at its Brewster angle inside the cavity. The optical cavity is resonant at the pump wavelength of 532 nm and has a measured finesse of 45. We applied a MW resonator to deliver frequency-modulated MW field to the diamond sample and used lock-in detection to avoid low-frequency technical noise in our measurements [2]. The ODMR spectrum presented in Fig. 1(a) was recorded by monitoring the emitted fluorescence from the diamond while sweeping the MW drive frequency accross the spin resonances. For this measurement, a static magnetic field was aligned along the [111] crystal axis, resulting in the outermost electron spin resonances (SR1,SR4), while the inner peaks (SR2,SR3) correspond to the electron spin resonances of the other three crystallographic orientations. We excited all three hyperfine transitions simultaneously by mixing the MW drive center frequency with a 2.16 MHz signal corresponding to the ^{14}N axial hyperfine splitting frequency.

The use of the optical cavity allows us to reach the linewidth-narrowing regime, thereby maximizing the measured ODMR slope and the sensitivity [2]. For deducing the sensitivity of the magnetometer, we independently measured three time traces of the lock-in signal for 0.4 W optical input power. The first trace was measured in the optimal magnetically sensitive configuration, driving the MW field on resonance with a spin transition corresponding to the blue dot in Fig. 1(a). The second trace was measured in the magnetically insensitive configuration, with the MW drive frequency far-detuned from any spin resonance. The last trace was measured with all detectors blocked, representing the electronic noise of our system. The Fourier transforms of these time traces are presented in Fig. 1(b), where the y axis is displayed in units of sensitivity. The spectra show a 125 Hz bandwidth and a 12 dB/octave roll-off that is generated by the low-pass filter of the lock-in detector. The magnetically insensitive trace shows a $\sim$400 pT/$\sqrt{\text{Hz}}$ noise floor. The magnetically sensitive trace includes a low-frequency magnetic noise mostly due to temperature fluctuations, and also detects a pronounced 50 Hz environmental magnetic noise.

3. Magnetometry based on pump absorption

As the ground state population of NV centers depends on the electron spin-state, we present an alternative technique for magnetic-field sensing based on the absorption of pump light [3]. We monitored the transmission of the cavity using the same diamond crystal and optical cavity. The result of sweeping frequency-modulated MW is an absorption detected magnetic resonance (ADMR), which is presented in Fig. 1(c). It should be noted that, compared to ODMR, the ADMR spectrum bears a 180^0 phase shift. In Fig. 1(d) we present the magnetic noise spectral density for an input power of 0.4 W, demonstrating a noise floor of $\sim$100 nT/$\sqrt{\text{Hz}}$ in the magnetically insensitive trace.

The ADMR spectrum can be modeled using a set of optical Bloch equations considering five electronic levels of the NV center. Employing an optical cavity, an ADMR spectrum may be obtained by recording the pump beam either reflected from or transmitted through the cavity as a function of the applied MW frequency [3]. The simulation results agree very well with the measured ADMR traces, as evidenced by the dashed line in Fig.1(c). Based on our simulations and considering a diamond with an optimized NV density, we estimate a photon shot-noise-limited sensitivity of $\sim$1 pT/$\sqrt{\text{Hz}}$ when measuring a cavity's reflected power near the impedance-matched point.

4. Conclusion

In conclusion, we report on a cavity-enhanced diamond magnetometer using the low NV concentration of a chemical-vapor-deposited diamond crystal. We reached a linewidth-narrowing regime by virtue of using a cavity resonant with the pump light, allowing for a sensitivity in the sub-nT/$\sqrt{\text{Hz}}$ regime to be reached based on fluorescence light detection.

In addition, we introduced an alternative spin resonance detection technique based on pump light absorption. We measured the cavity-assisted ADMR and obtained a noise floor of $\sim$100 nT/$\sqrt{\text{Hz}}$. We project a photon shot-noise-limited sensitivity of $\sim$1 pT/$\sqrt{\text{Hz}}$ by optimizing the NV concentration and the detection method. Using this technique we circumvent challenges associated with inefficient fluorescence collection.

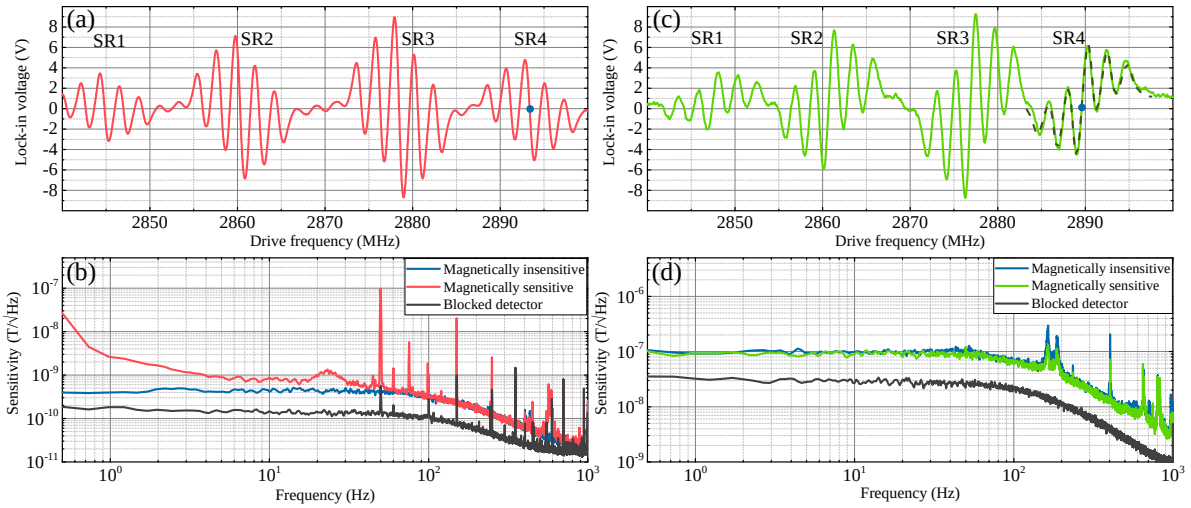

Fig. 1: Measured frequency-modulated (a) ODMR and (c) ADMR spectra. SR1 and SR4 correspond to the electron-spin resonances of a single crystallographic orientation, while SR2 and SR3 correspond to the resonances of the other three orientations. The blue dots indicate the points with the steepest slope and highest sensitivity. The dashed line in (c) is a simulated ADMR spectrum. The magnetic noise spectral density measurements are presented in (b) and (d), corresponding to ODMR and ADMR, respectively. The electronic noise for the same gain setting is also presented.

References

1. L. Rondin, J. P. Tetienne, T. Hingant, J. F. Roch, P. Maletinsky, V. Jacques, Rep. Prog. Phys. **77**, 056503 (2014).
2. S. Ahmadi, H. A. El-Ella, J. O. Hansen, A. Huck, and U. L. Andersen, Phys. Rev. Appl. **8**, 034001 (2017).
3. S. Ahmadi, H. A. El-Ella, A. M. Wojciechowski, T. Gehring, J. O. Hansen, A. Huck, and U. L. Andersen, arXiv:1712.05161 (2017), accepted in Phys. Rev. B.

Chapter 8

Outlook

In this thesis, continuous-wave magnetic field sensing with NV centers in diamond was discussed. First, background regarding the properties of NV centers and its use in sensing was described. Next, our experimental framework for cavity-enhanced magnetic field sensing with an ensemble of NV centers was introduced. Finally, the experimental results were presented. By measuring the changes in the fluorescence level, we demonstrated a magnetic noise density of ~ 400 pT/$\sqrt{\text{Hz}}$ spanning a bandwidth up to 125 Hz. In addition, a magnetic noise floor of ~ 100 nT/$\sqrt{\text{Hz}}$ was measured based on recording the absorption of the pump light.

The sensing of magnetic fields has important applications, especially in the fields of biology and biomedicine as it can be used noninvasively for diagnoses. However, several limitations have prevented current high-sensitive magnetometers to be accessible to every laboratory and hospital around the world, and thus, the development of affordable and sensitive magnetometers is required. The authors of Ref. [111] have discussed the commercial viability of diamond magnetometers, and they have estimated that an improved version of an NV magnetometer with the same functionality as SQUID magnetometers would be in demand for magnetocardiography devices.

Although we demonstrated sub-nano-Tesla/$\sqrt{\text{Hz}}$ magnetic field sensing, there are possibilities for improvement in terms of material, light coupling, collection efficiency, MW delivery, and reflection-based ADMR.

In our experiments, most of the propagation loss through the diamond was attributed to the non-NV loss channels. These loss channels reduced the finesse of the optical cavity and thus the excitation efficiency. Using a diamond where absorption of the NV centers is the dominant loss channel, increases the cavity-assisted excitation. Moreover, we determined the NV center concentration of ~ 0.16 ppb. A diamond with a higher density of NV centers improves the sensitivity by by a factor $\sqrt{\text{N}}$, where N is the number

of NV centers [11]. The concentration of NV centers can be enhanced by electron or ion irradiation and high-temperature annealing [112].

Expanding the excitation volume is another approach to address more NV spins, at the expense of a lower spatial resolution. In our measurements, we illuminated $\sim 10^9$ NV centers within the excitation volume of 3.5×10^{-2} mm^3. This volume can be increased by trapping the laser light inside the diamond and increase the optical path length [88].

In addition, a better photon collection scheme improves the sensitivity. We collected the fluorescence light only from one side of a diamond, which can be enhanced, for instance, by having high-reflection coating for red wavelengths on the opposite side of the diamond.

Based on our simulation, the reflection-based ADMR using an impedance-matched cavity enhances the sensitivity. Considering our attempt to reach the impedance-matched point, discussed in Section 6.3, an almost perfect Gaussian beam and better control of the loss inside the cavity is necessary to ensure no reflection occurs from the cavity input port.

Furthermore, a diamond magnetometer can be developed as a handheld device. An example of a handheld sensor is designed in Ref. [113], and its schematic is drawn in Fig. 8.1. The device contains a diamond, an MW antenna, a permanent magnet to resolve all orientation of the NV centers, and a photodiode to collect the fluorescence photons. The optical drive, MW drive, and all electronics such as LIA are included in a different holder and are connected to the handheld sensor with optical fiber and cables.

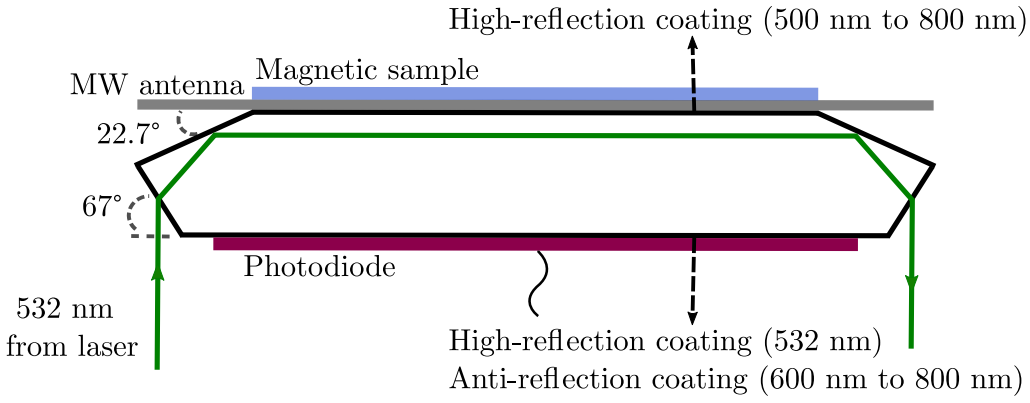

Figure 8.1: Schematic of the handheld magnetometer developed in Ref. [113]. Green arrow indicates the optical path of the excitation beam through the diamond. The magnetic sample is place on top of the MW antenna which has a thickness of 0.5 mm and shown in gray. The fluorescence is collected by attaching a photodiode on the larger side of the diamond with some index-matching material in between.

Figure 8.2 (a) shows a frequency-modulated ODMR spectrum measured with this handheld magnetometer using three-frequency excitation. A magnetic noise density of ~ 60 nT/$\sqrt{\text{Hz}}$ is demonstrated in Fig. 8.2 (b) spanning a bandwidth up to 125 Hz. The measurement is limited by the technical noise of the laser. An order of magnitude improvement is expected by canceling out the correlated laser noise.

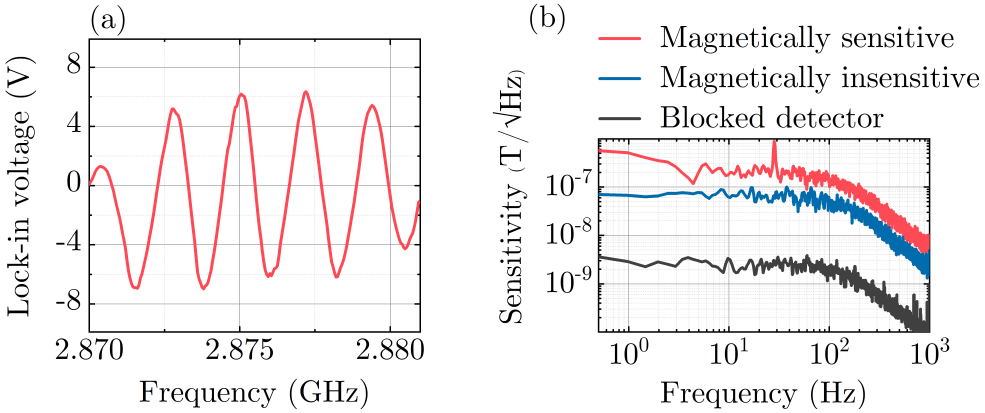

Figure 8.2: Characterization of the handheld magnetometer. (a) Plot of measured three-frequency-modulated ODMR spectrum. (b) Measurements of magnetic noise spectral density: The red trace corresponds to the magnetically sensitive configuration, when the MW drive being set to $\max(|\frac{d}{d\omega}S|)$ of the spin resonance, the blue trace is magnetically insensitive and measured when the MW drive was off-resonance, and the black trace shows the electronic noise of the system, when the detector was blocked. (b). Data taken from Ref. [113].

Diamond magnetometers operate at room temperature and have the potential to reduce the complexity and cost of the current state-of-the-art high-sensitive magnetometers. In addition, replacing the laser with an LED source reduces the cost of a device. An improved magnetic field sensor of approximately two orders of magnitude, compared to the presented results in this thesis would be practical for applications such as magnetocardiography.

Bibliography

[1]N. Lambert, Y. N. Chen, Y. C. Cheng, C. M. Li, G. Y. Chen, and F. Nori, "Quantum biology", Nature Physics **9**, 10–18 (2013) (cited on p. 1).

[2]J. Vrba, "Magnetoencephalography: The art of finding a needle in a haystack", Physica C: Superconductivity and its Applications **368**, 1–9 (2002) (cited on p. 2).

[3]J. Clarke and A. I. Braginski, *The SQUID handbook. Vol. 1, Fundamentals and technology of SQUIDS and SQUID systems* (Wiley-VCH, 2005) (cited on p. 3).

[4]K. Jensen, P. Kehayias, and D. Budker, *High sensitivity magnetometers, Magnetometry with nitrogen-vacancy centers in diamond* (Springer, 2017) (cited on p. 3, 9).

[5]M. Schmelz, R. Stolz, V. Zakosarenko, T. Schönau, S. Anders, L. Fritzsch, M. Mück, and H. G. Meyer, "Field-stable SQUID magnetometer with sub-fT Hz-1/2 resolution based on sub-micrometer cross-type Josephson tunnel junctions", Superconductor Science and Technology **24**, 065009 (2011) (cited on p. 3).

[6]I. K. Kominis, T. W. Kornack, J. C. Allred, and M. V. Romalis, "A subfemtotesla multichannel atomic magnetometer", Nature **422**, 596–599 (2003) (cited on p. 3).

[7]D. Sheng, S. Li, N. Dural, and M. V. Romalis, "Subfemtotesla scalar atomic magnetometry using multipass cells", Physical Review Letters **110**, 160802 (2013) (cited on p. 3).

[8]K. Jensen, R. Budvytyte, R. A. Thomas, T. Wang, A. Fuchs, M. V. Balabas, G. Vasilakis, L. Mosgaard, T. Heimburg, S.-P. Olesen, and E. S. Polzik, "Non-invasive detection of animal nerve impulses with an atomic magnetometer operating near quantum limited sensitivity", Scientific Reports **6**, 29638 (2016) (cited on p. 4).

[9]E. Boto, N. Holmes, J. Leggett, G. Roberts, V. Shah, S. S. Meyer, L. D. Muñoz, K. J. Mullinger, T. M. Tierney, S. Bestmann, G. R. Barnes, R. Bowtell, and M. J. Brookes, "Moving magnetoencephalography towards real-world applications with a wearable system", Nature **555**, 657–661 (2018) (cited on p. 4).

[10]G. Balasubramanian, I. Y. Chan, R. Kolesov, M. Al-Hmoud, J. Tisler, C. Shin, C. Kim, A. Wojcik, P. R. Hemmer, A. Krueger, T. Hanke, A. Leitenstorfer, R. Bratschitsch, F. Jelezko, and J. Wrachtrup, "Nanoscale imaging magnetometry with diamond spins under ambient conditions", Nature **455**, 648–651 (2008) (cited on p. 5).

[11]J. M. Taylor, P. Cappellaro, L. Childress, L. Jiang, D. Budker, P. R. Hemmer, A. Yacoby, R. Walsworth, and M. D. Lukin, "High-sensitivity diamond magnetometer with nanoscale resolution", Nature Physics **4**, 810–816 (2008) (cited on p. 5, 86).

[12]F. Dolde, H. Fedder, M. W. Doherty, T. Nöbauer, F. Rempp, G. Balasubramanian, T. Wolf, F. Reinhard, L. C. L. Hollenberg, F. Jelezko, and J. Wrachtrup, "Electric-field sensing using single diamond spins", Nature Physics **7**, 459–463 (2011) (cited on p. 5).

[13]E. H. Chen, H. A. Clevenson, K. A. Johnson, L. M. Pham, D. R. Englund, P. R. Hemmer, and D. A. Braje, "High-sensitivity spin-based electrometry with an ensemble of nitrogen-vacancy centers in diamond", Physical Review A **95**, 053417 (2017) (cited on p. 5).

[14]M. W. Doherty, V. V. Struzhkin, D. A. Simpson, L. P. McGuinness, Y. Meng, A. Stacey, T. J. Karle, R. J. Hemley, N. B. Manson, L. C. Hollenberg, and S. Prawer, "Electronic properties and metrology applications of the diamond NV - center under pressure", Physical Review Letters **112**, 047601 (2014) (cited on p. 5).

[15]G Kucsko, P. C. Maurer, N. Y. Yao, M Kubo, H. J. Noh, P. K. Lo, H Park, and M. D. Lukin, "Nanometre-scale thermometry in a living cell", Nature **500**, 54–58 (2013) (cited on p. 5).

[16]P. Neumann, I. Jakobi, F. Dolde, C. Burk, R. Reuter, G. Waldherr, J. Honert, T. Wolf, A. Brunner, J. H. Shim, D. Suter, H. Sumiya, J. Isoya, and J. Wrachtrup, "High-precision nanoscale temperature sensing using single defects in diamond.pdf", Nano Letters **13**, 2738–2742 (2013) (cited on p. 5).

[17]L. T. Hall, G. C. G. Beart, E. A. Thomas, D. A. Simpson, L. P. McGuinness, J. H. Cole, J. H. Manton, R. E. Scholten, F Jelezko, J. Wrachtrup, S Petrou, and L. C. L. Hollenberg, "High spatial and temporal resolution wide-field imaging of neuron activity using quantum NV-diamond.", Scientific Reports **2**, 1–9 (2012) (cited on p. 5).

[18]J. F. Barry, M. J. Turner, J. M. Schloss, D. R. Glenn, Y. Song, M. D. Lukin, H. Park, and R. L. Walsworth, "Optical magnetic detection of single-neuron action potentials using quantum defects in diamond", Proceedings of the National Academy of Sciences **113**, 14133–14138 (2016) (cited on p. 5).

[19]L. P. McGuinness, Y. Yan, A. Stacey, D. A. Simpson, L. T. Hall, D. Maclaurin, S. Prawer, P. Mulvaney, J. Wrachtrup, F. Caruso, R. E. Scholten, and L. C. Hollenberg, "Quantum measurement and orientation tracking of fluorescent nanodiamonds inside living cells", Nature Nanotechnology **6**, 358–363 (2011) (cited on p. 5).

[20]S. Steinert, F. Ziem, L. T. Hall, A. Zappe, M. Schweikert, N. Götz, A. Aird, G. Balasubramanian, L. Hollenberg, and J. Wrachtrup, "Magnetic spin imaging under ambient conditions with sub-cellular resolution", Nature Communications **4**, 1607 (2013) (cited on p. 5).

[21]D. R. Glenn, K. Lee, H. Park, R. Weissleder, A. Yacoby, M. D. Lukin, H. Lee, R. L. Walsworth, and C. B. Connolly, "Single-cell magnetic imaging using a quantum diamond microscope", Nature Methods **12**, 736–738 (2015) (cited on p. 5).

[22]S. J. Devience, L. M. Pham, I. Lovchinsky, A. O. Sushkov, N. Bar-Gill, C. Belthangady, F. Casola, M. Corbett, H. Zhang, M. Lukin, H. Park, A. Yacoby, and R. L. Walsworth, "Nanoscale NMR spectroscopy and imaging of multiple nuclear species", Nature Nanotechnology **10**, 129–134 (2015) (cited on p. 5).

[23]I. Lovchinsky, A. O. Sushkov, E. Urbach, N. P. de Leon, S. Choi, K. D. Greve, R. Evans, R. Gertner, E. Bersin, C. Müller, L. McGuinness, F. Jelezko, R. L. Walsworth, H. Park, and M. D. Lukin, "Nuclear magnetic resonance detection and spectroscopy of single proteins using quantum logic", Science **351**, 836–841 (2016) (cited on p. 5).

[24]J.-C. Jaskula, E. Bauch, S. Arroyo-Camejo, M. D. Lukin, S. W. Hell, A. S. Trifonov, and R. L. Walsworth, "Superresolution optical magnetic imaging and spectroscopy using individual electronic spins in diamond", Optics Express **25**, 11048–11064 (2017) (cited on p. 5).

[25]D. R. Glenn, D. B. Bucher, J. Lee, M. D. Lukin, H. Park, and R. L. Walsworth, "High-resolution magnetic resonance spectroscopy using a solid-state spin sensor", Nature **555**, 351–354 (2018) (cited on p. 5).

[26]R. R. Fu, B. P. Weiss, E. A. Lima, R. J. Harrison, X.-N. Bai, S. J. Desch, D. S. Ebel, C. Suavet, H. Wang, D. Glenn, D. L. Sage, T. Kasama, R. L. Walsworth, and A. T. Kuan, "Solar nebula magnetic fields recorded in the Semarkona meteorite", Science **346**, 1089–1092 (2014) (cited on p. 5).

[27]S Kolkowitz, A Safira, A. A. High, R. C. Devlin, S Choi, Q. P. Unterreithmeier, D Patterson, A. S. Zibrov, V. E. Manucharyan, H Park, and M. D. Lukin, "Probing Johnson noise and ballistic transport in normal metals with a single-spin qubit.", Science **347**, 1129–32 (2015) (cited on p. 5).

[28]A. Brenneis, L. Gaudreau, M. Seifert, H. Karl, M. S. Brandt, H. Huebl, J. A. Garrido, F. H. Koppens, and A. W. Holleitner, "Ultrafast electronic readout of diamond nitrogen-vacancy centres coupled to graphene", Nature Nanotechnology **10**, 135–139 (2015) (cited on p. 5).

[29]I. Jakobi, P. Neumann, Y. Wang, D. Dasari, F. E. Hallak, M. A. Bashir, M. Markham, A. Edmonds, D. Twitchen, and J. Wrachtrup, "Measuring broadband magnetic fields on the nanoscale using a hybrid quantum register", Nature Nanotechnology **12**, 67–72 (2017) (cited on p. 5).

[30]J. D. Breeze, E. Salvadori, J. Sathian, N. M. N. Alford, and C. W. Kay, "Continuous-wave room-temperature diamond maser", Nature **555**, 493–496 (2018) (cited on p. 5).

[31]N. Abe, Y. Mitsumori, M. Sadgrove, and K. Edamatsu, "Dynamically unpolarized single-photon source in diamond with intrinsic randomness", Scientific Reports **7**, 1–7 (2017) (cited on p. 5, 6).

[32]B. Hensen, H. Bernien, A. E. Dréau, A. Reiserer, N. Kalb, M. S. Blok, J. Ruitenberg, R. F. L. Vermeulen, R. N. Schouten, C. Abellán, W. Amaya, V. Pruneri, M. W. Mitchell, M. Markham, D. J. Twitchen, D. Elkouss, S. Wehner, T. H. Taminiau, and R. Hanson, "Loophole-free Bell inequality violation using electron spins separated by 1.3 kilometres", Nature, 1–5 (2015) (cited on p. 5).

[33]S. Choi, J. Choi, R. Landig, G. Kucsko, H. Zhou, J. Isoya, F. Jelezko, S. Onoda, H. Sumiya, V. Khemani, C. Von Keyserlingk, N. Y. Yao, E. Demler, and M. D. Lukin, "Observation of discrete time-crystalline order in a disordered dipolar many-body system", Nature **543**, 221–225 (2017) (cited on p. 5).

[34]N. M. Nusran, K. R. Joshi, K Cho, M. A. Tanatar, W. Meier, S. L. Bud'ko, P. C. Canfield, Y Liu, T. A. Lograsso, and R Prozorov, "Spatially-resolved study of the Meissner effect in superconductors using NV-centers-in-diamond optical magnetometry", New Journal of Physics **20**, 043010 (2018) (cited on p. 5).

[35]J. E. Field, "The mechanical and strength properties of diamond", Reports on Progress in Physics **75** (2012) (cited on p. 5).

[36]C. E. Nebel, D. Shin, B. Rezek, N. Tokuda, H. Uetsuka, and H. Watanabe, "Diamond and biology", Journal of the Royal Society Interface **4**, 439–461 (2007) (cited on p. 6).

[37]M. W. Doherty, N. B. Manson, P. Delaney, F. Jelezko, J. Wrachtrup, and L. C. Hollenberg, "The nitrogen-vacancy colour centre in diamond", Physics Reports **528**, 1–45 (2013) (cited on p. 6, 8, 9, 14).

[38]C. Wang, C. Kurtsiefer, H. Weinfurter, and B. Burchard, "Single photon emission from SiV centres in diamond produced by ion implantation", Journal of Physics B: Atomic, Molecular and Optical Physics **39**, 37–41 (2006) (cited on p. 6).

[39]E. Neu, D. Steinmetz, J. Riedrich-Möller, S. Gsell, M. Fischer, M. Schreck, and C. Becher, "Single photon emission from silicon-vacancy colour centres in chemical vapour deposition nano-diamonds on iridium", New Journal of Physics **13**, 025012 (2011) (cited on p. 6).

[40]L. J. Rogers, K. D. Jahnke, T. Teraji, L. Marseglia, C. Müller, B. Naydenov, H. Schauffert, C. Kranz, J. Isoya, L. P. McGuinness, and F. Jelezko, "Multiple intrinsically identical single-photon emitters in the solid state", Nature Communications **5**, 4739 (2014) (cited on p. 6).

[41]A. Sipahigil, R. E. Evans, D. D. Sukachev, M. J. Burek, J. Borregaard, M. K. Bhaskar, C. T. Nguyen, J. L. Pacheco, H. A. Atikian, C. Meuwly, R. M. Camacho, F. Jelezko, E. Bielejec, H. Park, M. Lončar, and M. D. Lukin, "An integrated diamond nanophotonics platform for quantum-optical networks", Science **354**, 847–850 (2016) (cited on p. 6).

[42]D. D. Sukachev, A. Sipahigil, C. T. Nguyen, M. K. Bhaskar, R. E. Evans, F. Jelezko, and M. D. Lukin, "Silicon-vacancy spin qubit in diamond: A quantum memory exceeding 10 ms with single-shot state readout", Physical Review Letters **119**, 223602 (2017) (cited on p. 6).

[43]Y. N. Palyanov, I. N. Kupriyanov, Y. M. Borzdov, and N. V. Surovtsev, "Germanium: A new catalyst for diamond synthesis and a new optically active impurity in diamond", Scientific Reports **5**, 14789 (2015) (cited on p. 6).

[44]E. A. Ekimov, S. G. Lyapin, K. N. Boldyrev, M. V. Kondrin, R. Khmelnitskiy, V. A. Gavva, T. V. Kotereva, and M. N. Popova, "Germanium-vacancy color center in isotopically enriched diamonds synthesized at high pressures", Journal of Experimental and Theoretical Physics Letters **102**, 701–706 (2015) (cited on p. 6).

[45]T. Iwasaki, F. Ishibashi, Y. Miyamoto, Y. Doi, S. Kobayashi, T. Miyazaki, K. Tahara, K. D. Jahnke, L. J. Rogers, B. Naydenov, F. Jelezko, S. Yamasaki, S. Nagamachi, T. Inubushi, N. Mizuochi, and M. Hatano, "Germanium-vacancy single color centers in diamond", Scientific Reports **5**, 12882 (2015) (cited on p. 6).

[46]P. Siyushev, M. H. Metsch, A. Ijaz, J. M. Binder, M. K. Bhaskar, D. D. Sukachev, A. Sipahigil, R. E. Evans, C. T. Nguyen, M. D. Lukin, P. R. Hemmer, Y. N. Palyanov, I. N. Kupriyanov, Y. M. Borzdov, L. J. Rogers, and F. Jelezko, "Optical and microwave control of germanium-vacancy center spins in diamond", Physical Review B **96**, 081201 (2017) (cited on p. 6).

[47]M. K. Bhaskar, D. D. Sukachev, A. Sipahigil, R. E. Evans, M. J. Burek, C. T. Nguyen, L. J. Rogers, P. Siyushev, M. H. Metsch, H. Park, F. Jelezko, M. Lončar, and M. D. Lukin, "Quantum nonlinear optics with a germanium-vacancy color center in a nanoscale diamond waveguide", Physical Review Letters **118**, 223603 (2017) (cited on p. 6).

[48]T. Iwasaki, Y. Miyamoto, T. Taniguchi, P. Siyushev, M. H. Metsch, F. Jelezko, and M. Hatano, "Tin-vacancy quantum emitters in diamond", Physical Review Letters **119**, 253601 (2017) (cited on p. 6).

[49]L Rondin, J. P. Tetienne, T Hingant, J. F. Roch, P Maletinsky, and V Jacques, "Magnetometry with nitrogen-vacancy defects in diamond", Reports on Progress in Physics **77**, 56503 (2014) (cited on p. 6, 9).

[50]P. Neumann, J. Beck, M. Steiner, F. Rempp, H. Fedder, P. R. Hemmer, J. Wrachtrup, and F. Jelezko, "Single-shot readout of a single nuclear spin", Science **329**, 542–4 (2010) (cited on p. 6).

[51]L. Robledo, L. Childress, H. Bernien, B. Hensen, P. F. A. Alkemade, and R. Hanson, "High-fidelity projective read-out of a solid-state spin quantum register", Nature **477**, 574–578 (2011) (cited on p. 6).

[52]W. Pfaff, T. H. Taminiau, L. Robledo, H. Bernien, M. Markham, D. J. Twitchen, and R. Hanson, "Demonstration of entanglement-by-measurement of solid-state qubits", Nature Physics **9**, 29–33 (2013) (cited on p. 6).

[53]F. P. Bundy, H. T. Hall, H. M. Strong, and R. H. Wentorf, "Man-made diamonds", Nature **176**, 51–55 (1955) (cited on p. 6).

[54]R. C. Burns, A. I. Chumakov, S. H. Connell, D. Dube, H. P. Godfried, J. O. Hansen, J. Härtwig, J. Hoszowska, F. Masiello, L. Mkhonza, M. Rebak, A. Rommevaux, R. Setshedi, and P. Van Vaerenbergh, "HPHT growth and x-ray characterization of high-quality type IIa diamond", Journal of Physics: Condensed Matter **21**, 364224 (2009) (cited on p. 6).

[55]M. Schwander and K. Partes, "A review of diamond synthesis by CVD processes", Diamond and Related Materials **20**, 1287–1301 (2011) (cited on p. 6).

[56]C. M. Breeding and J. E. Shigley, "The "type" classification system of diamonds and its importance in gemology", Gems & Gemology **45**, 96–111 (2009) (cited on p. 6, 7).

[57]Element Six, "The Element Six CVD diamond handbook", (cited on p. 7).

[58]G. Waldherr, J. Beck, M. Steiner, P. Neumann, A. Gali, T. H. Frauenheim, F. Jelezko, and J. Wrachtrup, "Dark states of single nitrogen-vacancy centers in diamond unraveled by single shot NMR", Physical Review Letters **106**, 157601 (2011) (cited on p. 7).

[59]N. Aslam, G. Waldherr, P. Neumann, F. Jelezko, and J. Wrachtrup, "Photo-induced ionization dynamics of the nitrogen vacancy defect in diamond investigated by single-shot charge state detection", New Journal of Physics **15** (2013) (cited on p. 7).

[60]M. Pfender, N. Aslam, P. Simon, D. Antonov, G. Thiering, S. Burk, F. Fávaro De Oliveira, A. Denisenko, H. Fedder, J. Meijer, J. A. Garrido, A. Gali, T. Teraji, J. Isoya, M. W. Doherty, A. Alkauskas, A. Gallo, A. Grüneis, P. Neumann, and J. Wrachtrup, "Protecting a diamond quantum memory by charge state control", Nano Letters **17**, 5931–5937 (2017) (cited on p. 7).

[61]S. Dhomkar, J. Henshaw, H. Jayakumar, and C. A. Meriles, "Long-term data storage in diamond", Science Advances **2**, 1–6 (2016) (cited on p. 7).

[62]M. E. Wieser and W. A. Brand, "Isotope ratio studies using mass spectrometry", Encyclopedia of Spectroscopy and Spectrometry, 1072–1086 (1999) (cited on p. 8, 12, 13).

[63]R. Schirhagl, K. Chang, M. Loretz, and C. L. Degen, "Nitrogen-vacancy centers in diamond: Nanoscale sensors for physics and biology", Annual Review of Physical Chemistry **65**, 83–105 (2014) (cited on p. 8).

[64]J. H. N. Loubser and J. A. van Wyk, "Electron spin resonance in the study of diamond", Reports on Progress in Physics **41**, 1201–1248 (1978) (cited on p. 8).

[65]V. M. Acosta, E. Bauch, M. P. Ledbetter, A. Waxman, L. S. Bouchard, and D. Budker, "Temperature dependence of the nitrogen-vacancy magnetic resonance in diamond", Physical Review Letters **104**, 070801 (2010) (cited on p. 8).

[66]J Fontanella, R. L. Johnston, J. H. Colwell, and C Andeen, "Temperature and pressure variation of the refractive index of diamond.", Applied Optics **16**, 2949–2951 (1977) (cited on p. 9).

[67]J. P. Hadden, J. P. Harrison, A. C. Stanley-Clarke, L. Marseglia, Y. L. D. Ho, B. R. Patton, J. L. O'Brien, and J. G. Rarity, "Strongly enhanced photon collection from diamond defect centers under microfabricated integrated solid immersion lenses", Applied Physics Letters **97**, 241901 (2010) (cited on p. 9).

[68]P. Siyushev, F. Kaiser, V. Jacques, I. Gerhardt, S. Bischof, H. Fedder, J. Dodson, M. Markham, D. Twitchen, F. Jelezko, and J. Wrachtrup, "Monolithic diamond optics for single photon detection", Applied Physics Letters **97**, 241902 (2010) (cited on p. 9).

[69]D. Riedel, D. Rohner, M. Ganzhorn, T. Kaldewey, P. Appel, E. Neu, R. J. Warburton, and P. Maletinsky, "Low-loss broadband antenna for efficient photon collection from a coherent spin in diamond", Physical Review Applied **2**, 064011 (2014) (cited on p. 9).

[70]N. M. Israelsen, S. Kumar, M. Tawfieq, J. S. Neergaard-Nielsen, A. Huck, and U. L. Andersen, "Increasing the photon collection rate from a single NV center with a silver mirror", Journal of Optics **16**, 114017 (2014) (cited on p. 10).

[71]S. A. Momenzadeh, R. J. Stöhr, F. F. De Oliveira, A. Brunner, A. Denisenko, S. Yang, F. Reinhard, and J. Wrachtrup, "Nanoengineered diamond waveguide as a robust bright platform for nanomagnetometry using shallow nitrogen vacancy centers", Nano Letters **15**, 165–169 (2015) (cited on p. 10).

[72]T. Wolf, P. Neumann, K. Nakamura, H. Sumiya, T. Ohshima, J. Isoya, and J. Wrachtrup, "Subpicotesla diamond magnetometry", Physical Review X **5**, 041001 (2015) (cited on p. 10).

[73]R. Albrecht, A. Bommer, C. Deutsch, J. Reichel, and C. Becher, "Coupling of a single nitrogen-vacancy center in diamond to a fiber-based microcavity", Physical Review Letters **110**, 243602 (2013) (cited on p. 10).

[74]H. Kaupp, T. Hümmer, M. Mader, B. Schlederer, J. Benedikter, P. Haeusser, H. C. Chang, H. Fedder, T. W. Hänsch, and D. Hunger, "Purcell-enhanced single-photon emission from nitrogen-vacancy centers coupled to a tunable microcavity", Physical Review Applied **6**, 054010 (2016) (cited on p. 10).

[75]D. Le Sage, L. M. Pham, N. Bar-Gill, C. Belthangady, M. D. Lukin, A. Yacoby, and R. L. Walsworth, "Efficient photon detection from color centers in a diamond optical waveguide", Physical Review B **85**, 121202 (2012) (cited on p. 10).

[76]S. Zhang, Z. Ma, L. Qin, Y. Fu, Y. Shi, J. Liu, and Y. Li, "Fluorescence detection using optical waveguide collection device with high efficiency on assembly of nitrogen vacancy centers in diamond", Applied Physics Express **11**, 013007 (2018) (cited on p. 10).

[77]Z. Ma, S. Zhang, Y. Fu, H. Yuan, Y. Shi, J. Gao, L. Qin, J. Tang, J. Liu, and Y. Li, "Magnetometry for precision measurement using frequency-modulation microwave combined efficient photon-collection technique on an ensemble of nitrogen-vacancy centers in diamond", Optics Express **26**, 382–390 (2018) (cited on p. 10).

[78]V. M. Huxter, T. a. a. Oliver, D Budker, and G. R. Fleming, "Vibrational and electronic dynamics of nitrogen–vacancy centres in diamond revealed by two-dimensional ultrafast spectroscopy", Nature Physics **9**, 744–749 (2013) (cited on p. 10).

[79]P. J. Mohr, D. B. Newell, and B. N. Taylor, "CODATA recommended values of the fundamental physical constants: 2014", Reviews of Modern Physics **88**, 035009 (2016) (cited on p. 11).

[80]N. D. Lai, D. Zheng, F. Jelezko, F. Treussart, and J. F. Roch, "Influence of a static magnetic field on the photoluminescence of an ensemble of nitrogen-vacancy color centers in a diamond single-crystal", Applied Physics Letters **95**, 133101 (2009) (cited on p. 12).

[81]R. Hanson, V. V. Dobrovitski, A. E. Feiguin, O. Gywat, and D. D. Awschalom, "Coherent dynamics of a single spin interacting with an adjustable spin bath", **320**, 352–355 (2008) (cited on p. 12).

[82]G. Balasubramanian, P. Neumann, D. Twitchen, M. Markham, R. Kolesov, N. Mizuochi, J. Isoya, J. Achard, J. Beck, J. Tissler, V. Jacques, P. R. Hemmer, F. Jelezko, and J. Wrachtrup, "Ultralong spin coherence time in isotopically engineered diamond", Nature Materials **8**, 383–387 (2009) (cited on p. 14).

[83]T. Astner, J. Gugler, A. Angerer, S. Wald, S. Putz, N. J. Mauser, M. Trupke, H. Sumiya, S. Onoda, J. Isoya, J. Schmiedmayer, P. Mohn, and J. Majer, "Solid-state electron spin lifetime limited by phononic vacuum modes", Nature Materials (2018) (cited on p. 14).

[84]M. W. Doherty, F. Dolde, H. Fedder, F. Jelezko, J. Wrachtrup, N. B. Manson, and L. C. Hollenberg, "Theory of the ground-state spin of the NV- center in diamond", Physical Review B **85**, 205203 (2012) (cited on p. 14).

[85]S. Ahmadi, H. A. El-Ella, J. O. Hansen, A. Huck, and U. L. Andersen, "Pump-enhanced continuous-wave magnetometry using nitrogen-vacancy ensembles", Physical Review Applied **8**, 034001 (2017) (cited on p. 15, 23, 32).

[86]L. Robledo, H. Bernien, T. V. D. Sar, and R. Hanson, "Spin dynamics in the optical cycle of single nitrogen-vacancy centres in diamond", New Journal of Physics **13**, 025013 (2011) (cited on p. 17).

[87]C. S. Shin, C. E. Avalos, M. C. Butler, D. R. Trease, S. J. Seltzer, J. Peter Mustonen, D. J. Kennedy, V. M. Acosta, D. Budker, A. Pines, and V. S. Bajaj, "Room-temperature operation of a radiofrequency diamond magnetometer near the shot-noise limit", Journal of Applied Physics **112**, 1–11 (2012) (cited on p. 17).

[88]H. Clevenson, M. E. Trusheim, C. Teale, T. Schröder, D. Braje, and D. Englund, "Broadband magnetometry and temperature sensing with a light-trapping diamond waveguide", Nature Physics **11**, 393–397 (2015) (cited on p. 17, 86).

[89]A. Wickenbrock, H. Zheng, L. Bougas, N. Leefer, S. Afach, A. Jarmola, V. M. Acosta, and D. Budker, "Microwave-free magnetometry with nitrogen-vacancy centers in diamond", Applied Physics Letters **109**, 053505 (2016) (cited on p. 18).

[90]D. A. Broadway, J. D. A. Wood, L. T. Hall, A. Stacey, M. Markham, D. A. Simpson, J. P. Tetienne, and L. C. L. Hollenberg, "Anticrossing spin dynamics of diamond nitrogen-vacancy centers and all-optical low-frequency magnetometry", Physical Review Applied **6**, 064001 (2016) (cited on p. 18).

[91]Y. Dumeige, M. Chipaux, V. Jacques, F. Treussart, J. F. Roch, T. Debuisschert, V. M. Acosta, A. Jarmola, K. Jensen, P. Kehayias, and D. Budker, "Magnetometry with nitrogen-vacancy ensembles in diamond based on infrared absorption in a doubly resonant optical cavity", Physical Review B **87**, 155202 (2013) (cited on p. 18).

[92]K Jensen, N Leefer, A Jarmola, Y Dumeige, V. M. Acosta, P Kehayias, B Patton, and D Budker, "Cavity-enhanced room-temperature magnetometry using absorption by nitrogen-vacancy centers in diamond", Physical Review Letters **112**, 160802 (2014) (cited on p. 18).

[93]G. Chatzidrosos, A. Wickenbrock, L. Bougas, N. Leefer, T. Wu, K. Jensen, Y. Dumeige, and D. Budker, "Miniature cavity-enhanced diamond magnetometer", Physical Review Applied **8**, 044019 (2017) (cited on p. 18).

[94]S. Ahmadi, H. A. El-Ella, A. M. Wojciechowski, T. Gehring, J. O. Hansen, A. Huck, and U. L. Andersen, "Nitrogen-vacancy ensemble magnetometry based on pump absorption", Physical Review B **97**, 024105 (2018) (cited on p. 18).

[95]G. de Lange, Z. H. Wang, D. Ristè, V. V. Dobrovitski, and R. Hanson, "Universal dynamical decoupling of a single solid-state spin from a spin bath", Science **330**, 60–63 (2010) (cited on p. 18).

[96]A. Stark, N. Aharon, T. Unden, D. Louzon, A. Huck, A. Retzker, U. L. Andersen, and F. Jelezko, "Narrow-bandwidth sensing of high-frequency fields with continuous dynamical decoupling", Nature Communications **8**, 1105 (2017) (cited on p. 18).

[97]A. M. Edmonds, U. F. S. D'Haenens-Johansson, R. J. Cruddace, M. E. Newton, K. M. C. Fu, C. Santori, R. G. Beausoleil, D. J. Twitchen, and M. L. Markham, "Production of oriented nitrogen-vacancy color centers in synthetic diamond", Physical Review B **86**, 035201 (2012) (cited on p. 19).

[98]M. Shamonin, E. Shamonina, V. Kalinin, and L. Solymar, "Resonant frequencies of a split-ring resonator: Analytical solutions and numerical simulations", Microwave and Optical Technology Letters **44**, 133–136 (2005) (cited on p. 20).

[99]L. Yan, M. Tang, V. Krozer, V. Zhurbenko, T. Jensen, C. Jiang, and T. K. Johansen, "Transmission line model for coupled rectangular double split-ring resonators", Microwave and Optical Technology Letters **53**, 1311–1315 (2011) (cited on p. 20).

[100]K. Bayat, J. Choy, M. Farrokh Baroughi, S. Meesala, and M. Loncar, "Efficient, uniform, and large area microwave magnetic coupling to NV centers in diamond using double split-ring resonators", Nano Letters **14**, 1208–1213 (2014) (cited on p. 20).

[101]D. M. Pozar, *Microwave engineering*, Third (John Wiley & Sons, 2005) (cited on p. 21).

[102]H.-A. Bachor and T. C. Ralph, *A guide to experiments in quantum optics*, Second (Wiley-VCH, 2004) (cited on p. 22).

[103]A. E. Siegman, *Lasers* (University Science Books, 1986) (cited on p. 23).

[104]R. W. P. Drever, J. L. Hall, F. V. Kowalski, J. Hough, G. M. Ford, A. J. Munley, and H. Ward, "Laser phase and frequency stabilization using an optical resonator", Applied Physics B **31**, 97–105 (1983) (cited on p. 24).

[105]E. D. Black, "An introduction to Pound-Drever-Hall laser frequency stabilization", American Journal of Physics **69**, 79–87 (2001) (cited on p. 24).

[106]G Dattoli, L. Giannessi, L. Mezi, and A. Torre, "Theory of generalized Bessel functions", Il Nuovo Cimento B **105**, 327–348 (1990) (cited on p. 25).

[107]D. P. Blair and P. H. Sydenham, "Phase sensitive detection as a means to recover signals buried in noise", Journal of Physics E: Scientific Instruments **8**, 621–627 (1975) (cited on p. 26).

[108]Standford Research Systems, "Model SR850 DSP lock-in amplifier", (2009) (cited on p. 26).

[109]H. A. R. El-Ella, S. Ahmadi, A. M. Wojciechowski, A. Huck, and U. L. Andersen, "Optimised frequency modulation for continuous-wave optical magnetic resonance sensing using nitrogen-vacancy ensembles", Optics Express **25**, 14809–14821 (2017) (cited on p. 29).

[110]P. Stoica and R. Moses, *Spectral analysis of signals* (Pearson Prentice Hall, 2005) (cited on p. 34).

[111]M. W. Dale and G. W. Morley, "Medical applications of diamond magnetometry: commercial viability", 1–10 (2017) (cited on p. 85).

[112]V. M. Acosta, E. Bauch, M. P. Ledbetter, C. Santori, K. M. C. Fu, P. E. Barclay, R. G. Beausoleil, H. Linget, J. F. Roch, F. Treussart, S. Chemerisov, W. Gawlik, and D. Budker, "Diamonds with a high density of nitrogen-vacancy centers for magnetometry applications", Physical Review B **80**, 1–15 (2009) (cited on p. 86).

[113]G. J. Johansen, "Handheld diamond magnetic field sensor", MSc thesis, Technical University of Denmark (2018) (cited on p. 86, 87).